

Three-Dimensional Micro-Mechanical Characterization of Concrete Vibration

FINAL REPORT

IRISE-24-P22-01-01

DECEMBER 2023

PITT | **IRISE**

CENTER FOR IMPACTFUL RESILIENT
INFRASTRUCTURE SCIENCE & ENGINEERING

1. Report No. IRISE-24-P22-01-01	2. Government Accession No.	3. Recipient's Catalog No.	
4. Title and Subtitle Three-Dimensional Micro-Mechanical Characterization of Concrete Vibration		5. Report Date April 2024	
		6. Performing Organization Code	
7. Author(s) Alessandro Fascetti, PhD. Julie M. Vandenbossche, PhD., PE Xiangdong Yan Megan Darnell		8. Performing Organization Report No. IRISE-24-P22-01-01	
9. Performing Organization Name and Address IRISE Department of Civil and Environmental Engineering University of Pittsburgh Benedum Hall 3700 O'Hara Street Pittsburgh, PA 15261		10. Work Unit No. (TRAIS)	
		11. Contract or Grant No. PITTIRISE2018	
12. Sponsoring Agency Name and Address The Pennsylvania Department of Transportation Bureau of Planning and Research Commonwealth Keystone Building 400 North Street, 6 th Floor Harrisburg, PA 17120-0064		13. Type of Report and Period Covered January 2022 – April 2024	
		14. Sponsoring Agency Code	
15. Supplementary Notes PI contact info: 742 Benedum Hall, 3700 O'Hara Street, Pittsburgh, PA 15261 – Fascetti@pitt.edu			
16. Abstract Vibration is a crucial step in slipform paving during construction; however, the specific usage scenarios have led to an unclear understanding of the relationship between vibratory energy input and the quality of concrete consolidation. Thus, developing a comprehensive evaluation system to assess and characterize the vibratory behavior in slipform paving would facilitate the creation of practical guidelines for optimizing the paving process under various conditions. This study explores how vibration energy affects the distribution of air, coarse aggregate, and mortar of concrete as well as providing a frame for homogeneity assessment. Initially, the study models the mechanical response of coarse aggregate to vibration energy during slipform paving, utilizing paver consolidation simulation (PaCS). The coarse aggregate is recognized and segmented with advanced computer vision techniques. Subsequently, "virtual aggregates" resembling real aggregates in morphology were generated using spherical harmonic expansion and random fields and reconstruct mesoscale model using discrete element simulation to model the optimal spatial distribution of aggregates. Then, the outcomes from concrete paving simulation experiments and numerical simulations are compared to establish a model explicitly correlating vibration energy input with concrete consolidation quality.			
17. Key Words Slipform paving; Vibration and compactions; Experimental design; Computer vision; Homogeneity and dispersion evaluation; Spherical harmonic expansion; Random field theory; Multiscale modeling		18. Distribution Statement No restrictions. This document is available from the National Technical Information Service, Springfield, VA 22161	
19. Security Classif. (of this report) Unclassified	20. Security Classif. (of this page) Unclassified	21. No. of Pages 52	22. Price

IRISE

The Impactful Resilient Infrastructure Science & Engineering consortium was established in the Department of Civil and Environmental Engineering in the Swanson School of Engineering at the University of Pittsburgh to address the challenges associated with aging transportation infrastructure. IRISE is addressing these challenges with a comprehensive approach that includes knowledge gathering, decision making, design of materials and assets and interventions. It features a collaborative effort among the public agencies that own and operate the infrastructure, the private companies that design and build it and the academic community to develop creative solutions that can be implemented to meet the needs of its members. To learn more, visit: <https://www.engineering.pitt.edu/irise/>.



Acknowledgements

The authors gratefully acknowledge the financial support of all contributing members of IRISE. In addition, we are indebted to the advice and assistance provided by Mark Gallardo of the Pennsylvania Department of Transportation, Yathi Yathepan of the Federal Highway Administration, Ken Urbanec of Allegheny County, Dave Sciuillo of Golden Triangle Construction, and Matt Blough, Charles Buchanan, and Chris Forry of the Pennsylvania Turnpike Commission.

Disclaimer

The views and conclusions contained in this document are those of the authors and should not be interpreted as representing official policies, either expressed or implied, of the Pennsylvania Department of Transportation, the Pennsylvania Turnpike Commission, Allegheny County, Golden Triangle Construction, Michael Baker International, the Constructors Association of Western Pennsylvania or CDR Maguire.

Three-Dimensional Micro-Mechanical Characterization of Concrete Vibration

April 30, 2024

Authors

Alessandro Fascetti, Ph.D., University of Pittsburgh

Julie M. Vandenbossche, Ph.D., P.E., University of Pittsburgh

Xiangdong Yan, University of Pittsburgh

Megan Darnell, University of Pittsburgh

Technical Reviewers

Matthew Blough – Pennsylvania Turnpike Commission

Charles Buchanan – Pennsylvania Turnpike Commission

Mark Gallardo – Pennsylvania Department of Transportation

Dave Sciullio – Golden Triangle Construction

Kenneth Urbanec – Allegheny County Department of Public Works

Yathi Yatheepan – Federal Highway Administration

Gang Zou – Michael Baker International

IRISE

The Impactful Resilient Infrastructure Science & Engineering (IRISE) consortium was established in the Department of Civil and Environmental Engineering in the Swanson School of Engineering at the University of Pittsburgh to address the challenges associated with aging transportation infrastructure. IRISE is addressing these challenges with a comprehensive approach that includes knowledge gathering, decision making, material durability and structural repair. It features a collaborative effort among the public

agencies that own and operate the infrastructure, the private companies that design and build it and the academic community to develop creative solutions that can be implemented to meet the needs of its members. To learn more, visit: <https://www.engineering.pitt.edu/irise/>.

Acknowledgements

We are indebted to the advice and assistance provided by the following representatives of IRISE member organizations that comprised the technical panel that guided work on the project: Allegheny County, PennDOT, PA Turnpike, Golden Triangle Construction, Michael Baker International, Contractors of Western Pennsylvania (CAWP), and CDR Maguire. The authors would also like to acknowledge the members of Frank Bryan Concrete and Neville Aggregates for supplying the materials used to make the concrete in this project. Finally, the authors would like to acknowledge the members from Minnich Manufacturing for providing the vibrator test setup used in this study.

Disclaimer

The views and conclusions contained in this document are those of the authors and should not be interpreted as representing official policies, either expressed or implied, of the Pennsylvania Department of Transportation, the Pennsylvania Turnpike Commission, the Allegheny County Department of Public Works, Golden Triangle Construction, the Constructors Association of Western Pennsylvania, CDR Maguire or Michael Baker International.

Table of contents

Three-Dimensional Micro-Mechanical Characterization of Concrete Vibration	4
Technical Reviewers	4
IRISE	4
Acknowledgements	5
Disclaimer	5
Table of contents	6
1. Introduction	8
2. Literature Review	11
2.1 Vibrators	12
2.1.1 Angle, Depth, and Spacing	12
2.1.2 Frequency	13
2.1.3 Amplitude	18
2.1.4 Paver Speed	19
2.2 Factors Influencing Required Vibration Energy	21
2.2.1 Ambient climatic conditions during paving	21
2.2.2 Concrete mixture design	21
2.3 Flowability of Concrete	25
2.4 Applicability of Current Tests	27
2.4.1 Box test	27
2.4.2 V-Kelly Test	29
2.5 Data Collection, Image Processing, and Investigation	32
2.6 Gaps in Knowledge	33
2.6.1 Test methods	33
2.6.2 Numerical modeling and assessment criteria	33
3. Experimental Methodology	35
3.1 Experimental Setup of PaCS	35
3.2 Experimental Procedure	39
4. Data Analysis	42
4.1 Vibration signal analysis	42
4.2 Image acquisition, CNN-based image recognition and image analysis	45
4.2.1 Image acquisition	45
4.2.2 CNN-based image recognition	45
4.2.3 Image analysis	47
4.3 Mathematical representation of aggregate morphology based on spherical harmonic expansion	54
4.3.1 Aggregate morphology acquisition	54
4.3.2 Virtual aggregate generation based on random radius field	55
4.3.3 Multi-scale aggregate morphology control	60
4.3.4 Validation of aggregate with morphological index	63
4.4 Discrete element method (DEM) simulation	66
4.4.1 Discrete aggregate generation and placement	67

4.4.2	Optimal spatial distribution of aggregate	69
4.5	Consolidation Analysis	72
4.5.1	Results of DEM simulation	72
4.5.2	Aggregate properties analysis.....	73
4.5.3	Aggregate homogeneity analysis	74
4.5.4	Aggregate dispersion analysis	75
4.5.5	Aggregate 3D spatial distribution analysis	77
5.	Discussion.....	79
5.1	PaCS Implementation	79
5.2	Effect of vibration on spatial distribution of aggregates	82
6.	Conclusion	84
7.	Bibliography.....	

1. Introduction

Consolidation is a construction process to make a mass of fresh concrete less porous and uniform in shape. To achieve consolidation during the slipform paving of a jointed plain concrete pavement (JPCP), fluid concrete is vibrated using external vibrators that are mounted to the front of the paver (**Figure 1**). The energy dispersed from these vibrators allows the fluid concrete to mobilize and consolidate. The goal of the vibration process is to evenly distribute aggregates and cement paste around the pavement reinforcement, as well as to remove entrapped air. Without a proper consolidation procedure, concrete can be either under- or over-consolidated (ACI Committee 305, 1991). Vibrating the concrete to a uniform consolidation increases the strength and durability of the concrete. Vibration energy is a function of the mass of the vibrating object (the vibrator shaft) and its angular and translational velocity (the frequency of the shaft and the speed of the paver) (Halliday, Resnick, & Walker, 2021). Using the correct amount of vibration energy is crucial in preventing over- and under-consolidated concrete.



Figure 1. Slipform paving with typical concrete vibrator.

Over-consolidation of fluid concrete can lead to segregation between the aggregates and cement paste. Segregation causes larger aggregates to settle to the bottom of the pavement while smaller aggregates and cement paste move to the surface, which reduces the overall pavement strength. Segregation can cause premature pavement cracking due to the decreased strength in their respective areas (ACI Committee 305, 1991). Additionally, over-consolidating concrete can also result in a reduction in entrained air, which decreases the freeze-thaw durability of the concrete and can lead to premature pavement distresses such as durability cracking (ACI Committee, 1996) (AASHTO, 1993).

Alternatively, under-consolidation of fluid concrete occurs when there is a lack of vibration energy. Under-consolidation can cause entrapped air voids in the hardened

concrete, as shown in **Figure 2**. These voids lead to an overall decrease in the concrete strength, making the pavement susceptible to premature fatigue cracking (AASHTO, 1993). Both over- and under-consolidation can eventually lead to early pavement distresses, poor ride quality, and increased maintenance costs. It is critical that contractors construct concrete pavements that are well-consolidated.

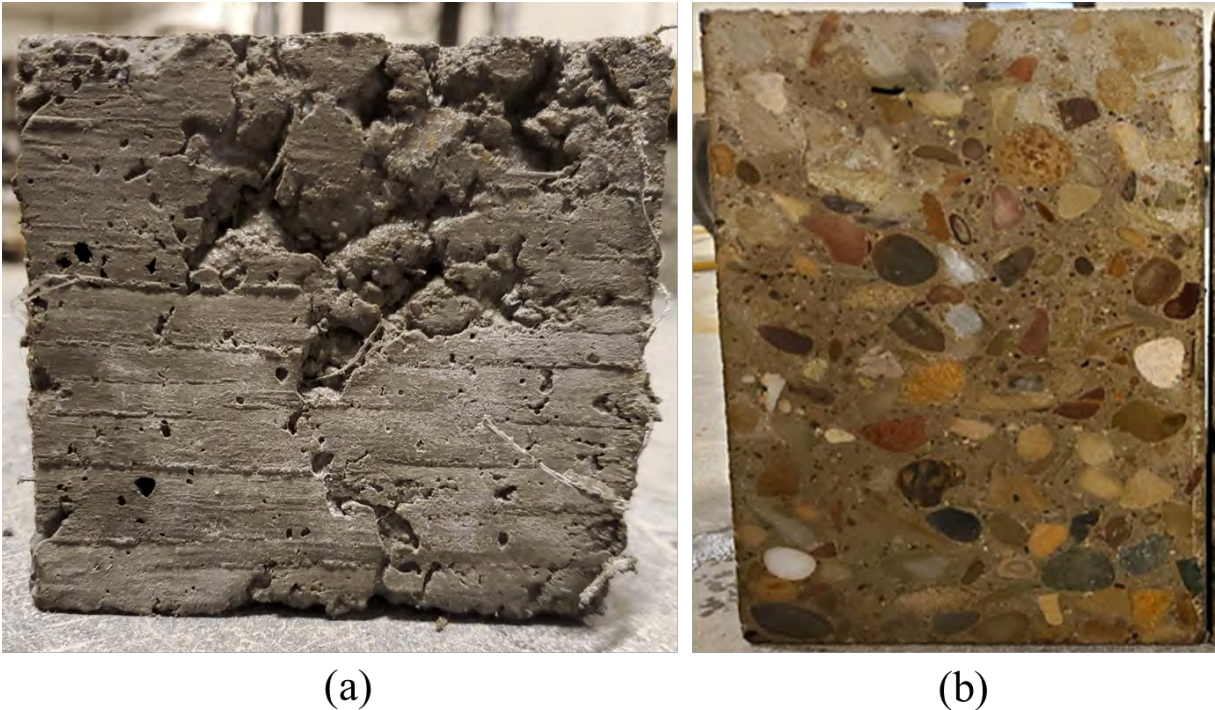


Figure 1. Examples of (a) under-consolidated concrete and (b) over-consolidated concrete.

Workability of the concrete mixture plays a role in how well it will consolidate (ACI Committee 305, 1991). Much of the recent research regarding consolidation has focused on the development of testing methods for quantifying the consolidation characteristics of the concrete mixture. Historically, workability has been characterized using the slump test. More recently, the Box Test (Ley, 2018) has been used to qualitatively characterize workability, while the V-Kelly Test (National Concrete Pavement Technology Laboratory) provides a quantitative means. While these tests provide an indication of the suitability of the concrete mixture, they do not define the level of vibration energy required to achieve proper consolidation. The energy needed to achieve proper consolidation varies as a function of not only the concrete mixture but also the climatic conditions during paving, the pavement design features (pavement thickness, presence of reinforcement, etc.), and the paving process.

Previous studies have evaluated the effect of vibration energy on consolidation; however, the focus has largely been on identifying the paving speed and vibrator frequency that is optimal for specific aspects of consolidation. A study performed by the Iowa Department of Transportation (Iowa DOT) analyzed the impact of vibrator frequency

and paver speed on the entrained air content of hardened concrete throughout the depth of the slab. It was found that vibration caused excess loss in entrained air when the paver speed was either slower than 2.5 ft/min or vibrator frequency exceeded 200 Hz (Steffes & Tymkowicz, *Vibrator Trails in Slipformed Pavements*, 1997). Similarly, Jaworski found frequencies exceeding 200 Hz resulted in a loss of entrained air content (Jaworski, *Vibrations Role Surface Defects-Concrete Surface Distresses Caused By Vibrator Speed*, 2017). When considering the effects of paving speed, Iowa DOT determined that a paver frequency of 200 Hz at 6.25 ft/min resulted in a pavement surface free of voids and reduced finishing requirements needed behind the paving machine (Cable, McDaniel, & Steffes, *Evaluation of Paver Vibrator Frequency Monitoring and Concrete Consolidation*, 1999). Based on the results of these studies, state departments of transportation (DOTs), such as PennDOT (PennDOT, 2020), MnDOT (MnDOT, 2003), and Iowa DOT (IowaDOT, 2015), have specified ranges of vibrator frequencies and concrete workability to use on slipform paving projects. While these studies evaluated the effect of vibration energy on entrained air, they were not able to quantify total consolidation. Additionally, these studies were limited to specific mixture designs and did not consider the vibration energy required as a function of the workability of the concrete mixture.

There is a need to study how different combinations of vibrator frequency, paver speed, and concrete workability impact the quality of consolidation on slipform paving projects. In this study, a novel, small-scale experimental setup was developed to quantify the consolidation of fluid concrete as a function of key paving parameters. This setup, referred to as the Paver Consolidation Simulation (PaCS), will be used to replicate the conditions of slipform paving and measure the level of consolidation achieved for a range of key paving parameters. Results from this study will allow the researchers to determine the optimal amount of vibration energy needed based on the workability of the concrete mixture. This is useful for assisting paving contractors in selecting appropriate vibration frequencies that will result in the construction of long-life, durable concrete pavements based on the concrete workability and paver speed.

2. Literature Review

The purpose of the vibrators when paving concrete is to evenly disperse the aggregates and cement paste around the pavement reinforcement and to remove entrapped air voids. By vibrating the concrete, the concrete is properly consolidated, which allows for a more durable pavement performance that is more resistant to pavement distresses. When improper consolidation occurs, it can lead to segregation of aggregates, water movement, air entrapment, removal of entrained air, and poor ride quality after the curing process. However, the vibration process is more complicated than it may appear. Vibration parameters, including frequency and depth of the vibrator, speed of the paver, and other field conditions may lead to improper consolidation of the concrete. However, the parameters in which improper consolidation of concrete occurs are not well understood. Due to the lack of understanding of these parameters, it is important to study the effect of varying vibration conditions on the resulting quality of the concrete pavement. These vibration conditions include the type of vibrator used, factors that influence vibrator energy, and the flowability of the concrete mix during vibration. Prior to conducting research on how these conditions may impact concrete consolidation and pavement performance, it is crucial to explore past research in these areas to identify how the vibration of concrete affects the compaction and performance of concrete pavements.

This report consists of a literature review of previous research on the effects of varying vibration parameters on concrete pavement consolidation. The first area reviewed consists of characteristics of the paver used, including the angle, depth, spacing, frequency and amplitude of the vibrators, and the speed of the paver. The next area reviewed covers factors that influence the required vibration energy into the concrete mixture, including climatic conditions during paving and the concrete mixture design. Next, prior work characterizing the flowability of concrete and how it impacts consolidation is summarized. This is followed by a review on current tests used to characterize concrete flowability and segregation tendencies, such as the Box and V-Kelly tests. The applications and limitations of these tests with respect to characterizing concrete used for paving is also examined. Finally, a discussion is provided on the noticeable gaps in knowledge and what must be explored further to close those gaps.

2.1 Vibrators

Factors affecting the energy generated by the vibrator have been explored to determine what has a noticeable impact on the consolidation of the concrete mixture. These factors include the angle, depth, spacing, frequency and amplitude of the concrete vibrators, as well as the speed of the paver. By changing any of these factors, it is possible that the concrete mixture may consolidate in a different way, leading to varying pavement performances. Due to this, it is important to review past research in these areas so a proper method to consolidate concrete pavements can be determined and a concrete mixture that can be easily consolidated is utilized.

2.1.1 Angle, Depth, and Spacing

Three areas regarding energy transfer from the vibrator to the pavement that have been studied include the angle and depth of each vibrator into the concrete mixture, as well as the spacing between all the vibrators on the paver. The orientation of a vibrator in the concrete during paving can be seen in **Figure 3**. A common vibration angle is between 5 and 10 degrees above the horizontal (Jaworski, Vibrations Role Surface Decets-Concrete Surface Distresses Caused By Vibrator Speed, 2017). Additionally, vibrator spacing is typically between 12 and 18 in (Steffes & Tymkowicz, Vibrator Trails in Slipformed Pavements, 1997), with most Departments of Transportations (DOT) specifying less than 16 in (Jaworski, Vibrations Role Surface Decets-Concrete Surface Distresses Caused By Vibrator Speed, 2017). Furthermore, the closer the vibrator is to the pavement surface, the lower the air content will be at the surface, which results in fewer voids (Jaworski, Vibrations Role Surface Decets-Concrete Surface Distresses Caused By Vibrator Speed, 2017). However, aggregate segregation should be avoided at all depths of the concrete pavement, not only at the surface. Variations in vibration angle, depth, and spacing are not well-studied. It is important to study how varying vibration angles, depths, and spacings can change the consolidation of the concrete because a corresponding impact on concrete pavement performance can be noted.

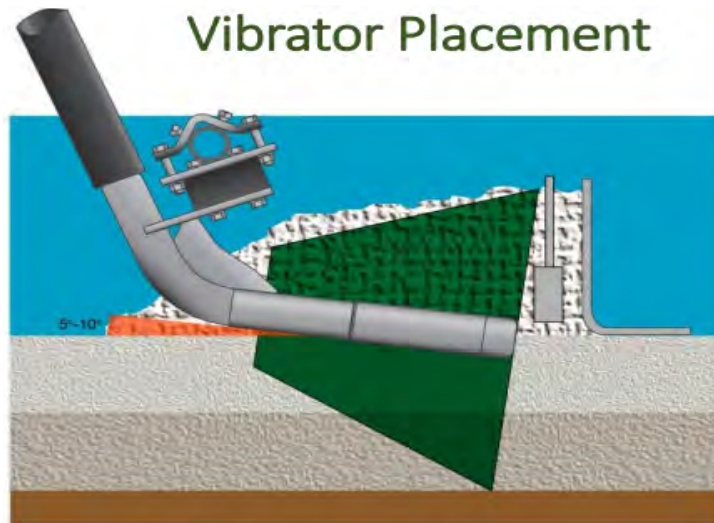


Figure 3: Vibrator Placement (Jaworski, Vibrations Role Surface Decets-Concrete Surface Distresses Caused By Vibrator Speed, 2017).

2.1.2 Frequency

Vibrator frequency is a parameter that has been better documented regarding impact on the consolidation process. Vibration at an excessively high frequency will cause segregation and remove the micro-air (< 40 mils) from the concrete, thereby creating durability issues. Insufficient vibration will result in entrapped air in the concrete. The important factors in characterizing the vibratory frequency are establishing the target value, determining what to use for measuring frequency, and establishing a protocol for taking the measurements. Each of these three components are discussed below.

A typical frequency range is from 83 to 133 Hz according to the Iowa DOT (Iowa DOT, 2008). This range has been chosen because it limits the amount of pavement surface distresses (Jaworksi, 2022), which has been verified in different studies. In a study sponsored by the Iowa DOT in 1999, entrained air contents were compared at different vibration frequencies, 83 Hz, 133 Hz, and 200 Hz. Excessive vibration of Portland cement concrete (PCC) can cause vibrator trails that have high paste and low air contents, but the specification of 83 to 133 Hz did prevent the formation of vibrator trails at normal paver speeds. The data provided in the study show the difference in average air content between concrete vibrated at 83 Hz and 133 Hz does not differ much. These values can be seen in Error! Reference source not found. (Steffes & Tymkowicz, Vibration Study for Consolidation of Portland Cement Concrete, 1999). A statistical analysis was not performed as a part of their study to determine the significance of the difference between the averages so as a part of this IRISE project the statistical significance was investigated. Specifically, an analysis was conducted on the difference between the average entrained air values for the 83 Hz and the 133 Hz data samples to test for statistical significance, controlling for location relative to the vibrator. It was found

that the difference in results was not statistically significant at a 95% confidence level. This implies that when paver speed and location relative to the vibrator are controlled, a vibrator frequency of 83 Hz or 133 Hz will yield similar results. However, the difference in the entrained air content within the vibrator trail and between the vibrator trail, both for the 83 Hz and 133 Hz samples, was found to be statistically significant at a 95% confidence level. This implies that, in the range of 83 to 133 Hz, the variability in vibration frequency did not have as much impact on the air content of the pavement as the location of the core did (Steffes & Tymkowicz, Vibration Study for Consolidation of Portland Cement Concrete, 1999).

Table 1: Average Entrained Air Contents by Frequency (Steffes & Tymkowicz, Vibration Study for Consolidation of Portland Cement Concrete, 1999).

Vibrator Frequency (Hz)	Paver Speed	Location Relative to Vibrator(s)	Number of Samples	Average	Standard Deviation
83	Normal	All	18	7.698	0.578
		In Trail	9	7.454	0.544
		Between	9	7.942	0.532
133	Normal	All	18	7.498	1.007
		In Trail	9	6.901	1.073
		Between	9	8.094	0.451

The study also compared entrained air contents in concrete pavements that were vibrated at 133 and 200 Hz. The test results indicated that the vibrator frequency may greatly affect the entrained air content at a frequency of 200 Hz by reducing the air content significantly. The greatest reduction in air content for the 200 Hz test was seen in the middle of the pavement core. These values can be seen in **Table 2** and shown graphically in **Figure 4**. By vibrating the concrete pavement at 200 Hz, the entrained air contents were drastically reduced at the top and the middle of the pavement core (Steffes & Tymkowicz, Vibration Study for Consolidation of Portland Cement Concrete, 1999). This would make the top and middle cores most susceptible to freeze-thaw cracking due to the lack of entrained air. This data leads to the conclusion that the concrete can become over-consolidated when vibrated at 200 Hz instead of 83 or 133 Hz.

Table 2: Average Entrained Air Contents by Core Location (Slow Paver Speed)

Treatment	Top of Core	Middle of Core	Bottom of Core
Between Vibrators	8.383	8.810	7.933
In Trail at 133 Hz	5.550	7.460	7.013
In Trail at 200 Hz	4.032	1.610	5.610

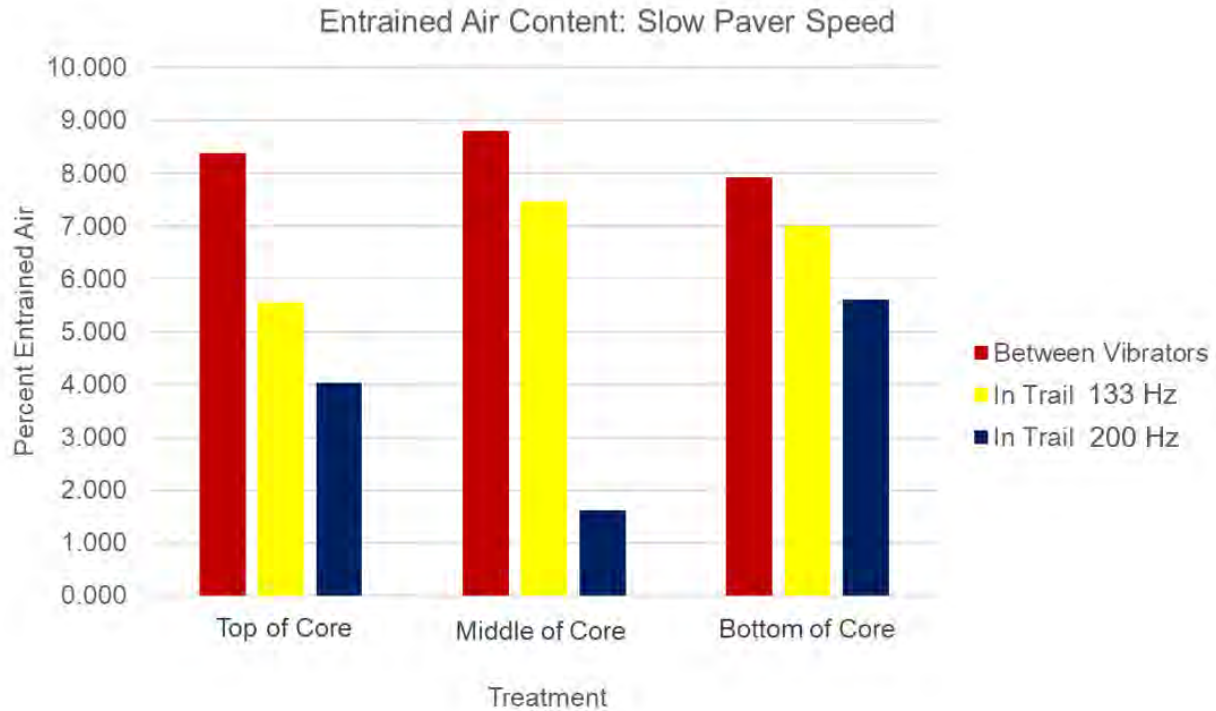


Figure 4: Average Entrained Air Contents by Core Location (Steffes & Tymkowicz, 1999).

Another study sponsored by Iowa DOT found that the combination of slow vibrator frequencies (83 Hz) and low forward paver speed (4 ft/min) created the potential for open surfaces behind the paving machine, if the consistency of the material being delivered varied in any way. The combination of high vibratory frequencies (133 Hz) and high forward paver speed (6.25 ft/min) resulted in a surface free of voids and reduced any finishing requirements behind the paving machine by providing a uniform product and surface across the slab (Cable, McDaniel, & Steffes, 1999). This study emphasized the importance of studying the frequency and paver speed, and the results can be implemented in further studies regarding the changing of vibration parameters needed for proper construction of concrete pavements.

Jaworski noted that high vibrator frequencies reduce the micro air (< 40 mils) content (Jaworski, Vibrations Role Surface Decets-Concrete Surface Distresses Caused By Vibrator Speed, 2017). It was found that, generally, vibrator frequencies over 133 Hz result in greater loss of entrained air, which is consistent with the Iowa DOT study previously mentioned. Additionally, there was a greater chance of poor aggregate arrangement at these higher frequencies. When aggregate segregation occurs, the larger particles usually settle to the bottom of the mix while the finer particles and paste rise to the top. This creates an unequal distribution of strength throughout the pavement, which can negatively impact durability and performance. Additionally, it was found that the micro air content is also reduced when the vibrator is pushed slowly through the concrete (Jaworski, Vibrations Role Surface Decets-Concrete Surface Distresses Caused By

Vibrator Speed, 2017).

In summary, 83 Hz is a good frequency to aim for to have optimal micro- and macro-air content, consistent cores, and aggregate arrangement for this mixture and the specific paving conditions. By vibrating the concrete mix at 83 Hz, consistent air and aggregate distribution was found to likely to occur, which leads to consistent durability and performance throughout the mix. However, a vibrator setting of 133 Hz was found to be good for the pavement surface finish (Jaworski, Vibrations Role Surface Decets-Concrete Surface Distresses Caused By Vibrator Speed, 2017). A good surface finish leads to better ride quality of the pavement, and thus safer conditions for motorists, increased fuel economy, reduced vehicular damage, and better pavement durability (SME, n.d.). Finally, 108 Hz is considered to produce average results regarding air and aggregate dispersion, as well as surface finish (Jaworski, 2017).

The Iowa DOT has established a protocol for determining the vibrator frequency for an individual vibrator on a slipform Portland Cement Concrete (PCC) paver, including the type of equipment to use when reading vibration frequencies. A ½ inch diameter steel rod with a small fork on the lower end was used. It is attached to the vibrator body or hydraulic line protector hose as shown in **Figure 3**. The length of the rod depends on the distance above the paver operator expanded metal walkway down to the vibrators, and the limit on the width of the fork is dependent on the size of the openings in the expanded metal walkway. Tachometers are used as well, which consist of a series of consecutively tuned reeds to determine the speed of the vibrator on the paving machine in revolutions per minute (rpm). The tachometers used included the Vibra-Tak and the Standco (Iowa DOT, 2008). The Vibra-Tak tachometer is a single wire reed type tachometer, which works by holding the tachometer against a vibrating object and observing the movement of the single reed. There is an adjustable slide rule below the reed which is meant to match the frequency of the vibrating object. The operator adjusts the slide rule until the wire reed has reached a maximum movement range, or throw, and then reads the scale which notes the frequency of the vibration in rpm (Workmaster, 2018). The Standco tachometer is a vibrating reed type tachometer, which has multiple calibrated reeds that measure frequency by picking up the rate of vibration of an object. These reeds indicate the speed of the vibration in rpm and display the speed on an analog scale (Sticht). The Vibra-Tak is sometimes preferred over the Standco as it has a wide range of frequencies that can be measured, is low-cost, durable and gives readings with acceptable accuracy (Iowa DOT, 2008).

Immediately after paving begins, it is advised by Iowa DOT to start taking readings of the vibrator, which are best obtained through contact with the hydraulic line protector hose. Readings are best obtained here due to ease of readability and minimal damage to the tachometer. This is shown as point A in **Figure 5** below. The other options for vibrator reading locations are points B and C, also shown in **Figure 5**. It is also advised by the Iowa DOT to check and record the frequency of at least two vibrators each day vibration monitoring is used. When vibration monitoring is not used, the frequency of every vibrator should be recorded twice daily. Vibration transmission to the tachometer is found by

placing the lower end of the forked rod on or near each vibrator while reading the vibrations per minute from the tachometer at the top end of the rod (Iowa DOT, 2008).

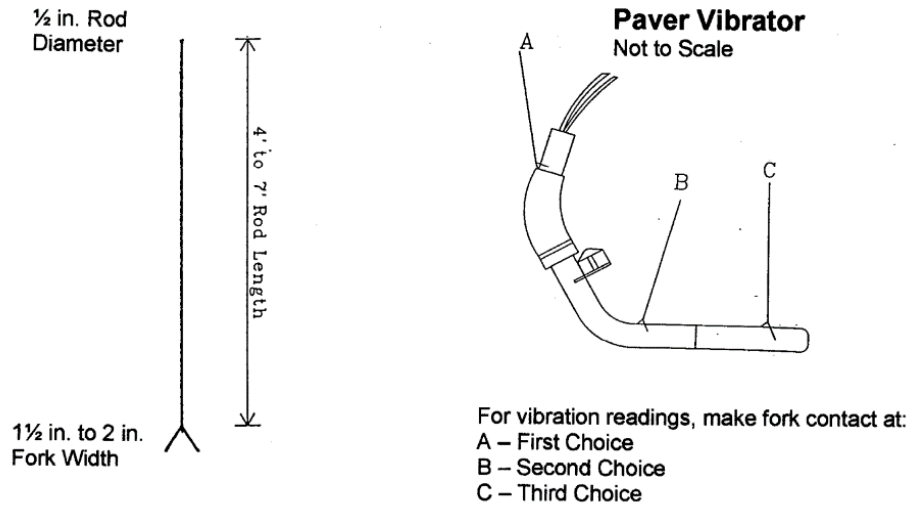


Figure 5: Tachometer Placements on Paver Vibrator (Iowa DOT, 2008)

2.1.3 Amplitude

The amplitude of vibration has also been previously studied regarding impact on concrete consolidation. A study performed by the Construction Material Laboratory group at Tohoku University analyzed how a change in amplitude with consistent frequency impacted aggregate segregation in self-consolidating concrete. While the results might not directly correlate to the behavior of the stiffer concrete mixture used for slipform paving, the findings of the study might be tangible and provide guidance into the parameters that should be accounted for in this IRISE study. The researchers kept the frequency at 160 Hz, while amplitudes of 0.0012 in (0.03 mm), 0.0020 in (0.05 mm), and 0.0039 in (0.10 mm) were compared. A higher slump flow value also correlated to higher values of the Segregation Coefficient (SC), but there is a more defined trend when only comparing amplitude and SC value. Forces are created by the vibrator in the concrete which ultimately mobilize the coarse aggregate particles and determine the final quality of the concrete (Safawi & Iwaki, 2005). This study showed a correlation between increased amplitude and increased aggregate segregation in self-consolidating concrete. Although the results of this study cannot be directly related to low-slump concrete pavements, they suggest that a lower amplitude is preferred during vibration of wet concrete to prevent such segregation. This claim must be further investigated to provide an answer for how changes in vibrator amplitude impacts concrete pavements.

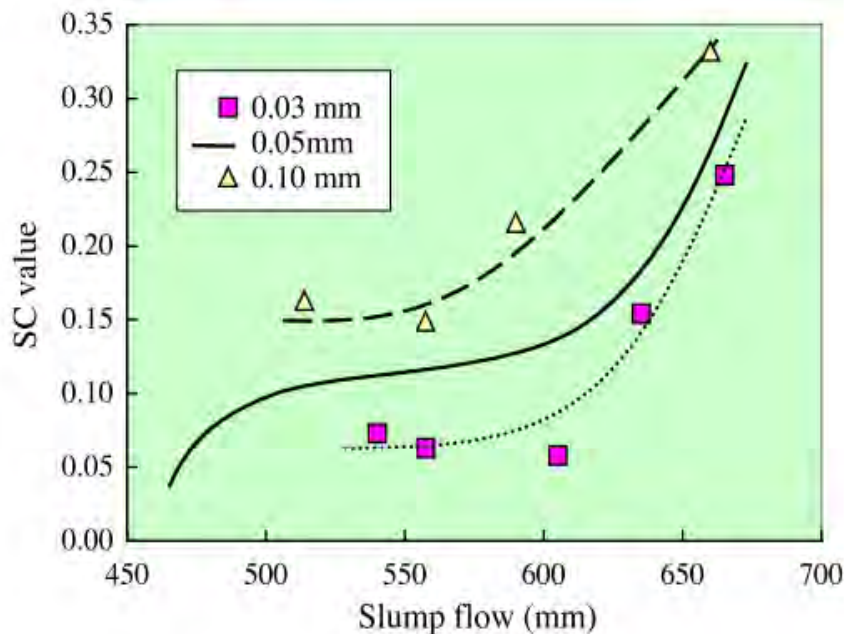


Figure 6: Segregation Results by Different Amplitude of Vibration

2.1.4 Paver Speed

Varying the operating speed of the paver will change the duration of time the concrete is vibrated, which can lead to either over- or under-consolidation. The average slipform paving speed is between 3 and 8 ft/min according to the Federal Highway Administration (Federal Highway Administration, 1995). Cable et al. (1999) reported a high forward paver speed of 6.25 ft/min would provide a surface free of voids and reduced finishing requirements behind the paving machine when used in combination with a vibratory frequency of 133 Hz. The effects of this combination on the entrained air system and potential segregation were not noted. The paver speed is typically dictated by the rate at which the concrete can be produced and transported to the location of placement and not with consideration for the effect paver speed has on consolidation of the concrete. Although, it is important to determine the effect of the speed of the paver on concrete consolidation for the paving conditions present, such as the mixture design, climate, time the concrete sits on the grade, concrete head in front of the paver, energy imposed by the vibrator, etc. The effects of changing paver speed on the consolidation of concrete pavements are not well studied, but there are various works that have tried to correlate the paver speed to aggregate segregation in concrete mixes. A study conducted by the Colorado Department of Highways compared two concrete mixtures, one with fine aggregates and one with coarse aggregates. For the coarse aggregate mixture, the paver used was equipped with a surface pan vibrator and two internal vibrators that could be spaced at any setting. The angles of the vibrators were changed, as was the height of the vibrator from the base of the slab, while the paver speeds were varied from 10 to 19 ft/min (Bower & Gerhardt, 1971). With the average slipform paving speed typically ranging between 3 to 8 ft/min, this study may provide results that are not directly applicable to most slipform paving processes. When comparing different paver speeds, it was found that range between these speeds resulted in very little variation in consolidation of the concrete, while vibration frequencies and amplitudes had a slightly greater effect, although not significant (Bower & Gerhardt, 1971). It should also be noted that a statistical analysis was not completed for this study to establish statistically significant findings.

The effect of paver speed was also investigated by Iowa DOT (Steffes & Tymkowicz, 1997). This study mentioned previously also looked at the effects of paver speed and vibrator frequency on air entrainment. The paver speed was evaluated at two levels: normal (5 ft/min) and slow (2.5 ft/min). As can be seen from **Table 3**, it was found that the paver speed had a slight impact on the entrained air in the concrete mix. At 133 Hz, the normal paver speed resulted in slightly higher levels of entrained air contents than the tests with the slow paver speed, regardless of the location relative to the vibrator (Steffes & Tymkowicz, 1999). With this data available, a statistical analysis was performed as part of this study. It was determined that the difference between the average entrained air content for the normal and slow paver speeds was found to not be statistically significant at a 95% confidence level for each sample location (relative to the location of the vibrator). Therefore, no significant conclusions can be drawn from this data

regarding paver speed on average entrained air contents. Although the study sponsored by Iowa DOT showed insignificant differences in entrained air contents at different paver speeds, there may be optimal paver speed and vibration frequency combinations that produce pavements with minimal voids and proper surface finish. Further research must be performed to identify the optimum combinations.

Table 3: Average Entrained Air Contents by Paver Speed (Steffes & Tymkowicz, 1997).

Vibrator Frequency (Hz)	Paver Speed	Location Relative to Vibrator(s)	Number of Samples	Average	Standard Deviation
133	Normal	All	18	7.498	1.007
		In Trail	9	6.901	1.073
		Between	9	8.094	0.451
133	Slow	All	18	7.098	1.017
		In Trail	9	6.713	0.637
		Between	9	7.483	1.207

In summary, vibrator angle, depth, and spacing, as well as paver speed have not been well-studied regarding their impacts on concrete pavement vibration and consolidation. Vibrator frequency and amplitude have been studied to greater lengths. The studies previously mentioned show that the optimal vibration speed for air and aggregate distribution is 83 Hz, while 133 Hz is best for surface finish, 108 Hz is considered the average between these settings, and 200 Hz leads to over-consolidation. It has also been found that increased vibrator amplitude can result in increased aggregate segregation for low slump concrete but the effects on concrete mixtures used for slipform paving have yet to be investigated. Due to this, it is important to continue researching these areas regarding their impact on concrete consolidation, and thus pavement performance.

2.2 Factors Influencing Required Vibration Energy

Not only do the characteristics of the vibrator settings affect the consolidation process of concrete mixes, but other factors can also play a role in influencing the required input of energy into the mix. Depending on the properties of the concrete mixture, different levels of required vibration energy may be needed to achieve optimal consolidation. These factors include ambient climatic conditions during paving, the head of concrete in front of the paver, type of base, how long the concrete sits on the grade or even how the concrete is placed in front of the paver (dumped vs belt placer). Such factors may impact how concrete pavement consolidates both during and after (post-consolidation around the basket due to gravity) the vibration process. Due to this, it is important to explore previous research in these areas to determine how varying climatic conditions and concrete mixture designs can impact pavement durability after vibration.

2.2.1 Ambient climatic conditions during paving

Certain climatic conditions, particularly high heat, humidity, and wind velocity can affect the workability and strength of fresh concrete. When a fresh concrete mixture is placed in the field during such conditions, it is known as hot weather concreting. Hot weather concreting is defined by the American Concrete Institute (ACI) as “operations concerning the preparation, production, delivery, placement, finishing, protection, and curing of concrete during hot weather” (ACI Committee 305, 1991). ACI defines hot weather as site conditions that accelerate moisture loss or reduction in cement hydration in a fresh concrete mixture. This includes ambient temperature at or above 80 degrees Fahrenheit, an evaporation rate over 0.205 lb/ft²/hr, or as revised by the engineer in charge of the concrete placement. The evaporation rate increases as the wind velocity increases (ACI Committee 305, 1991).

2.2.2 Concrete mixture design

2.2.2.1 Aggregate gradation and shape

Understanding the impact of coarse aggregate gradation, shape, and density is also very important to analyzing the effects of concrete mixture design on the amount of energy required for proper vibration. A research group from the Pontifical Catholic University of Chile found that the shape of the aggregate in a concrete mix plays a significant role in segregation. Segregation can be reduced by either reducing the maximum size of the aggregate or by increasing the angularity of coarse aggregate. As the density difference between coarse aggregate and mortar increases, the volume-to-surface area ratio becomes more significant in explaining the segregation rate. The lower

segregation rate was due to an increased drag force from the concrete mortar on the small aggregates, which can impact concrete durability. However, the mixtures were still susceptible to segregation by excessive vibration (Navarrete & Lopez, 2017). This study shows that concrete pavement segregation can be mitigated through choice of coarse aggregate size and shape, but vibration parameters still play a key factor in determining potential segregation of the mix, and thus the pavement durability.

Another study sponsored by the National Concrete Pavement Technology Center used a digital image processing (DIP) method associated with a MATLAB algorithm to evaluate cross sectional images of aggregates in self-consolidating concrete mixes. The mixtures were made with limestone and river gravel coarse aggregate. Each type of coarse aggregate used had three different nominal maximum sizes (NMSA), 0.75 in (19 mm), 0.50 in (12.5 mm), and 0.375 in (9.5 mm). The research group developed a new index named the mortar thickness index, which is a ratio between the area of mortar and coarse aggregate in a slice of the concrete mixture. Each of the six aggregates were compared based on average mortar thickness index (MTI), the average spacing between aggregate particle surfaces (D_{ss}), average aggregate diameter (D_{av}), and the ratio of the paste volume and the volume of voids in the combined aggregate system (V_{paste}/V_{voids}). The results of this study can be seen in **Figure 7** and **Figure 8**. These graphs show a trend that, with similar gradations, the MTI of gravel mixtures is higher than that of limestone mixtures when compared to the volume of the voids and the average spacing between particles. This means that a self-consolidating concrete sample, the gravel was better distributed amongst the mortar than the limestone of the same size. The researchers state that this is because limestone particles of higher angularity tend to increase the packing density of the concrete mixture (Wang, Wang, Han, & Taylor, 2015). While this can be a disadvantage for self-consolidating concrete, it could be advantageous for concrete used for slipform paving. As a part of the future vibration study, an aggregate image analysis will be conducted to track aggregate particles as energy is imposed through vibration. Although the results of this study are based on self-consolidating concrete, they may be applicable to slipform paving concrete in determining aggregate dispersion with different types and gradations of aggregate. Further research must be conducted to determine the applicability of these results to concrete used for slipform paving.

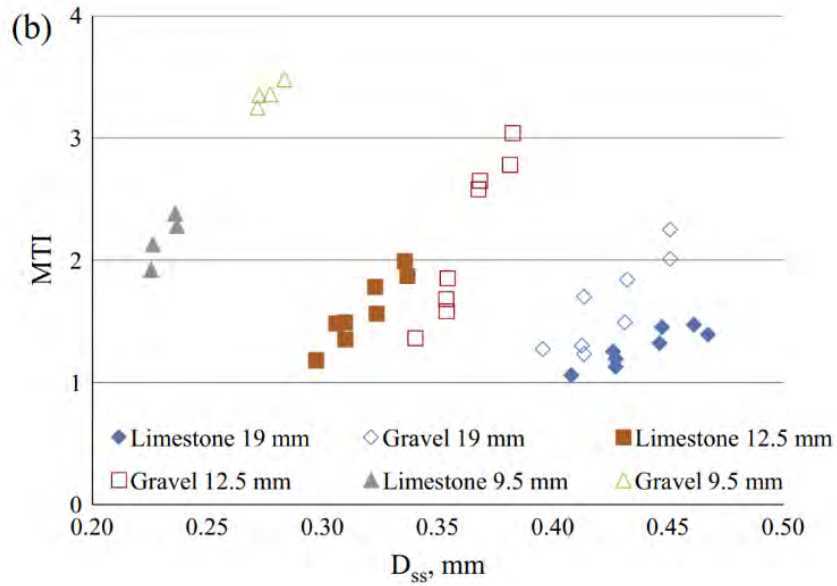


Figure 7: D_{ss} vs MTI (Wang, Wang, Han, & Taylor, 2015)

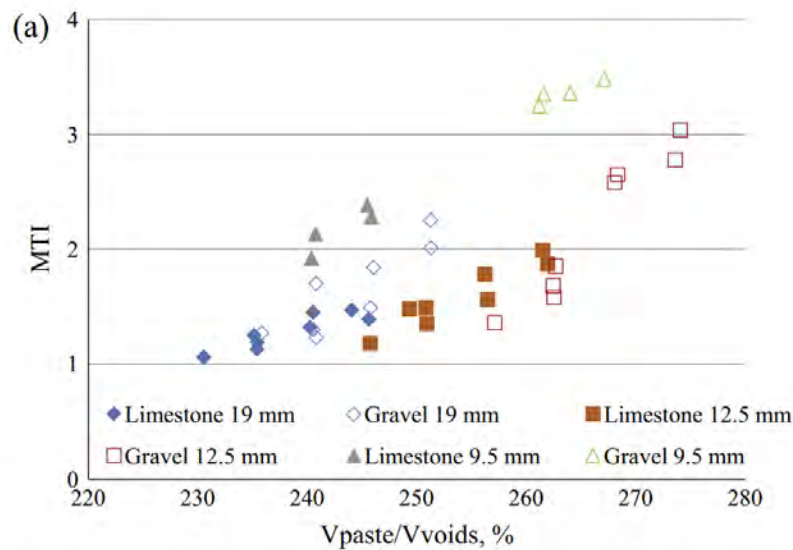


Figure 8: V_{paste}/V_{voids} vs MTI (Wang, Wang, Han, & Taylor, 2015)

Additionally, a researcher from Nigde University used a numerical approach to analyze aggregates in self-consolidating concrete mixtures. A mathematical model which considered fresh concrete as a non-Newtonian fluid and aggregate as Lagrangian particles was developed, and the relationship between aggregate segregation and viscosity of fresh concrete while being poured into formwork was investigated. The model was built based on previous concrete experiments that conducted research on testing and modelling of fresh concrete rheology. The researchers found that the main parameters that effect segregation are the ratios of the materials in the fresh concrete mixture. Viscosity values and water to cementitious (w/c) ratios are not as critical for determining segregation (Bilgil, Ozturk, & Bilgil, 2005). Although the results of this study

are based on self-consolidating concrete, the conclusions may be applicable to low slump slipform paving concrete and used with different vibration parameters to determine which properties may exacerbate concrete pavement segregation. This claim must be further investigated to provide a more definitive answer for how segregation relates to the viscosity of fresh paving concrete.

2.2.2.2 Admixtures

Introducing admixtures to the concrete mixture design can either increase or decrease the flowability of the mixture, which can then impact the durability after vibration and curing. The common practice in slipform paving is to use low-slump (approx. 1.5 in) concrete that is vibrated well to consolidate the mixture. Certain admixtures can increase the flowability of the concrete to the point of making vibration unnecessary for proper consolidation, which is known as self-consolidating concrete. The American Concrete Institute published a study that focused on optimizing the consolidation properties and shape stability of fresh concrete mixtures so that the internal vibration would not be needed in slip-form paving. They found that it is possible to design a concrete mixture that can be consolidated without internal or external vibration and at the same time can maintain its slab shape at the end of a slipform paving process. It is achieved by selectively manipulating flowability, consolidation properties, and green strength of fresh concrete through chemical admixtures or the addition of small amounts of fine materials (Pekmezci, Voigt, Wang, & Shah, 2007). Although self-consolidating concrete is outside the scope of this research area, the qualities of self-consolidating concrete can be studied and compared to normal concrete mixes through aggregate image analysis.

2.3 Flowability of Concrete

The varying flowability of the concrete mixture design refers to the fluidity of the mixture. The higher the flowability, the easier it is to place the concrete around the tie and dowel bars/baskets. The flowability of the mixture is often characterized with the slump test. The test is conducted by filling a metal mold with concrete in three lifts, then slowly lifting the mold and comparing the height of the concrete pile to the height of the mold. See **Figure 9**. The difference in the heights of the concrete and slump mold is known as the slump value. A slump of 0.5 to 1.5 in is typically required for slipform paving. Although the slump test is commonly used in the lab and in the field, it has limitations. Mainly, it is not a reliable test for lean concrete mixes where there is great variation in the mixtures. This is because the true slump may convert to a shear slump, which shows lack of cohesion of the mix. Additionally, the slump value does not describe ease of compaction because the test is conducted without vibration techniques (Civil Today, n.d.). Therefore, although the slump test can be used for concrete pavements in testing workability, it gives little relevant information about the response of the mixture when vibrated.

Slump values also provide little knowledge of the likelihood of segregation of the mixture. Referring to the Construction Material Laboratory group at Tohoku University, the slump value for a concrete mixture was found to have no impact on the coefficient of segregation. The coefficient of segregation compares the total weight of coarse aggregates retained through a sieve analysis divided by the total weight of concrete in the form. A low value for the coefficient of segregation indicates minimal segregation while a higher value indicates significant segregation. This means in cases of highly flowable mixes with similar viscosities, segregation was independent of the magnitude of flowability (Safawi & Iwaki, 2005). Although a slump test can indicate the flowability of the mixture, which is useful, it was found to not be a reliable indicator of whether the mixture is susceptible to aggregate or water segregation. The focus of this work was self-consolidating concrete, but most likely similar conclusions would be achieved for the stiffer slip-form paving concrete. A more comprehensive test must be used to provide such information.



Figure 9: Concrete Slump Test (Civil Today, n.d.)

Flowability of concrete can indicate how workable a mixture is, but there is little research showing a connection between level of flowability and tendency for water or aggregate segregation. Further work should be performed to determine whether such a connection exists, or if it is truly not related. If a connection is found, the results of a slump test may be a good indicator of whether a concrete mixture will be likely to segregate or not. However, there are other tests besides the normal slump test that can be conducted to give information on the concrete workability.

2.4 Applicability of Current Tests

The last area of investigation for this work is how current concrete pavement tests apply to and limit the determination of concrete consolidation characteristics. These tests include the Box test and the V-Kelly test, which are designed for low-slump concrete mixtures that are meant to be consolidated with a concrete vibrator. There are several other tests that determine consolidation characteristics, but the focus of these tests is self-consolidating concrete mixtures and are therefore outside the scope of this work and will not be discussed. The applications and limitations of the Box test and V-Kelly test should be analyzed to determine how to best characterize the flow of concrete under vibration.

2.4.1 Box test

The Box Test was created by Dr. Tyler Ley from Oklahoma State University and was designed to describe the workability of hydraulic-cement concrete in a slip-formed paving application, both in the laboratory and in the field. It is a two-part test that assesses dynamic behavior of plastic concrete through vibration and the static behavior of plastic concrete by its ability to hold its shape after formwork removal. This test method provides a simplistic and economic approach to determine the workability of concrete to be used for slip-form pavements and not for concrete mixtures with a slump of 3 in or greater. To conduct the Box test, the operator must obtain a 12 in x 12 in x 12 in oil-coated wooden form with removable sides and a wooden platform, shown in **Figure 10**. The wooden form must be clamped together to prevent movement and seepage of the concrete as much as possible. Using a hand scoop, fresh unconsolidated concrete is filled into the form to a height of 9.5 in without tamping. A concrete vibrator with a frequency of 208 Hz is inserted vertically downward into the center of the mixture for 3 seconds, and then removed vertically upward for 3 seconds. The vibrator head should be perpendicular to the platform but should not touch it. Once the vibrator is removed and turned off, the forms are removed carefully to prevent the concrete from sticking to the forms. Each side of the concrete cube is then compared visually to the chart shown in **Figure 11** to estimate the amount of voids in the mixture. The final determination of the percentage of the overall voids is based on the average of the four sides (Colorado DOT, 2019).

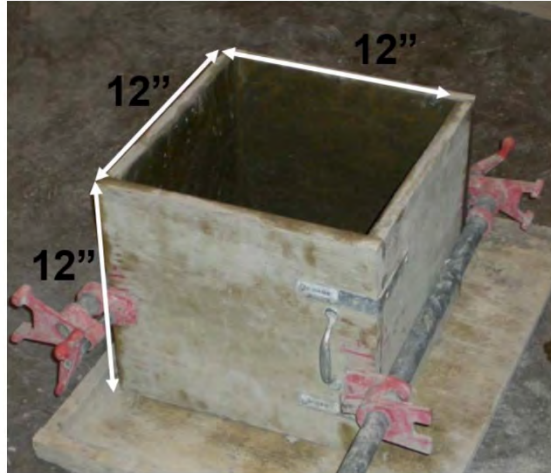


Figure 10: Box Test Form (Colorado DOT, 2019)

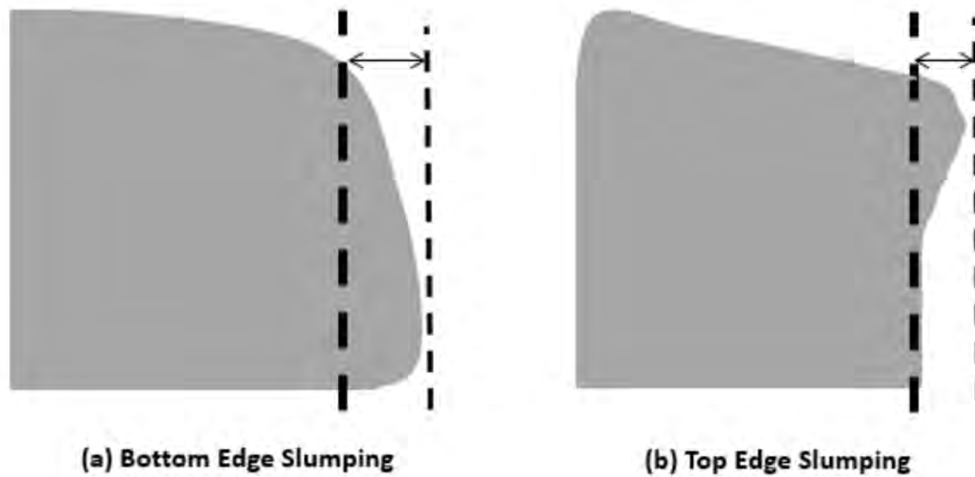


Figure 11: Box Test Edge Slump Measurement (Colorado DOT, 2019)

The concrete cube is then visually inspected for edge slump produced by the mixture. This is done by taking a straight edge and holding it against a corner of the sample and measuring the largest extruding length to the nearest 0.25 inch, as shown in **Figure 11**. This process should be performed for all four sides of the concrete sample with each value reported (Colorado DOT, 2019). The purpose of measuring the average void content and edge slump of each corner of the sample is to determine how well a mixture will be consolidated with a given amount of energy and if it is prone to edge slump. An edge slump of less than 0.25 in and a void ranking of 2 (30% overall surface voids) or less are the most desirable outcomes (National Concrete Pavement Technology Laboratory). While the Box test is useful in quantifying the behavior of a fluid concrete mixture, it is limited in that it is difficult to visually characterize aggregate distribution and how different sized aggregates respond to vibration.

2.4.2 V-Kelly Test

The V-Kelly Test is used to assess the response of a concrete mixture to vibration (i.e., the workability) (Taylor & Wang, 2018). The V-Kelly test was originally created by Professor J.W. Kelly of the Department of Civil Engineering of the University of California (Grieb et al. n.d.) and was later updated by the National Concrete Pavement Technology Center. The test can report both static and dynamic characteristics of the concrete mixture while simulating the effect of vibration from paving. It was intended to primarily be used for mixture design purposes, but it could also be used in the field. With increasingly complex concrete mixtures and placement processes, there is an increased need to measure how a mixture responds to vibration. The V-Kelly Test allows for this accurate prediction of mixture response to vibration because researchers can graphically determine whether a concrete mixture will be easy or difficult to consolidate, as well as the likelihood of edge slump after vibration. The V-Kelly test is also more accurate in determining consistency than the slump test. The V-Kelly test is applicable to a similar range of concrete consistencies used for the slump test, that being concrete of medium to low workability, but it is also appropriate for special concrete mixtures such as lightweight and heavyweight concrete. Mixtures with similar slumps may respond very differently when a vibrator is applied to a mixture. The V-Kelly test directly measures how fluid a mixture becomes when it is vibrated. The test is conducted in both a static and dynamic manner on unconsolidated concrete. For the static test, which can be seen in **Figure 12**, concrete is placed in a rubber tub until flushed with the top of the tub. A graduated shaft is manually placed in the middle of the concrete surface. The initial reading on the graduated scale is recorded to the nearest 1/10 of an inch. After this, the shaft is released and allowed to sink from its own weight until it comes to rest. The depth of the shaft is then recorded again to the nearest 1/10 of an inch (National Concrete Pavement Technology Center, 2018).



Figure 12: Depth of Penetration Under Static Load (National Concrete Pavement Technology Center, 2018)



Figure 13: Depth of Penetration Under Dynamic Load (National Concrete Pavement Technology Laboratory).

Once the static test is complete, the dynamic test can be conducted, which can be seen in **Figure 13**. The vibrator attached to the apparatus is turned on to a low speed, such as 133 Hz, while simultaneously another participant keeps time. The increasing depth of the shaft is recorded every 6 seconds until either 36 seconds are reached or the shaft reaches the bottom of the rubber tub. If the test is being conducted in a lab, the concrete should be remixed in a mixer for 30 seconds and the test should be reconducted. If the test is being conducted in the field, the test should be reconducted with fresh concrete. A minimum of three reading sets should be taken and should be within half an inch of each other. Once this is complete, the average depth of penetration can be found by plotting the penetration length against the square root of the time it was taken at. The best fit line is given by **Equation 1**.

$$D = V\sqrt{t} + C \quad (1)$$

where

$$\begin{aligned} D &= \text{Penetration depth at time } t \\ t &= \text{Elapsed time of vibration (seconds)} \\ C &= \text{non - zero constant} \\ V &= V - \text{Kelly Index} \end{aligned}$$

The V-Kelly index is the slope of the line of best fit. This index tells researchers

how easily a concrete mixture will consolidate when using vibration. An index value of $0.8 - 1.2 \text{ in}/\sqrt{s}$ is considered good for slipform paving concrete. A value below $0.6 \text{ in}/\sqrt{s}$ indicates that the mixture will be difficult to consolidate, while a value above $1.1 \text{ in}/\sqrt{s}$ indicates that the mixture will be prone to edge slump, causing deformed finished pavements (National Concrete Pavement Technology Laboratory). The V-Kelly test is much more useful than the previous tests mentioned regarding concrete pavements because researchers can gain knowledge of how the concrete will respond to the vibration process. Although the V-Kelly test provides more useful information than the slump test, the main drawback is that the precision of the test declines with the increasing size of coarse aggregate (Taylor & Wang, 2018). Therefore, the V-Kelly test is not as accurate for concrete mixture designs with larger aggregates ($>1.5 \text{ in}$). This leaves researchers with insufficient information regarding large-aggregate mix design consistency.

There are several tests used to measure varying qualities of concrete. While many of them may give necessary information for self-consolidating concrete, they do not offer insight into slipform paving concrete. Two tests that are useful in determining qualities of low-slump slipform paving concretes are the Box test and the V-Kelly test. The Box test was designed to describe how fresh concrete responds to vibration through visual void inspection and the development of edge slump. While knowing these properties are useful for slipform concrete pavements, the Box test is not useful in visually inspecting aggregate distribution, which is an important aspect of this vibration study. The V-Kelly test was designed to provide information on concrete pavement, specifically regarding the fluidity of the mix during vibration, the ease of consolidation, and the likelihood of edge slump after vibration. However, the V-Kelly test is limited due to the decrease in precision as aggregate sizes increase. Due these factors, future work should be performed that can test the flowability, likelihood of segregation, and likelihood of edge slump for slipform paving concrete based on an established amount of energy needed for proper placement.

2.5 Data Collection, Image Processing, and Investigation

To analyze the distribution of coarse aggregate and evaluate the quality of concrete consolidation, it is crucial to identify, isolate, and digitally reconstruct the coarse aggregate. Previously, digital reconstructions primarily involved manually differentiating aggregates from cement paste by artificially coloring the aggregate regions, followed by the extraction of these aggregates using the Otsu algorithm (Wang et al., 2015). This process facilitated the computation of the aggregate size, orientation, spacing, and uniformity from the digital images (Han et al., 2016). Moreover, the three-dimensional arrangement of aggregates was estimated to a certain extent using Cavalieri's principle (Baddeley and Jensen, 2004). Nevertheless, this approach was labor-intensive and resulted in irreversible damage to the concrete samples. Consequently, researchers have explored using naturally colored aggregates and color-based pixel recognition and extraction techniques to mitigate extensive lab work. However, due to the non-uniform color distribution of aggregates and variations in experimental conditions, numerous adjustments are often necessary to accurately delineate aggregate boundaries (Yan et al., 2024b; Chai et al., 2023).

The recent advancements in computer vision have encouraged researchers to explore the application of convolutional neural networks (CNNs) or deep convolutional neural networks (DCNNs) for concrete feature extraction (Wang et al., 2022; Zhou et al., 2019b). However, a significant challenge in using CNNs for coarse aggregate recognition and segmentation is the requirement for a large dataset of pre-labeled images to effectively train these networks, a demand that is impractical for small-scale lab studies. Therefore, for small laboratory investigations, there is a need to develop a convenient and reliable set of image recognition and segmentation tools that can simplify image-based analysis and evaluation.

In addition, reflecting the distribution of 3D aggregates in space through 2D images has been shown to be a convenient and effective method for assessing aggregate discrete properties (Wang et al., 2015). However, past studies have mainly focused on the investigation of high-flow concrete and have not investigated vibration for different sizes of aggregates. Therefore, a suitable image evaluation method is needed to reflect the different correspondences of aggregate size to vibration.

2.6 Gaps in Knowledge

2.6.1 Test methods

Even considering all the work performed by researchers, there are still aspects of concrete pavement consolidation that have not been properly investigated and leave current researchers with unanswered questions. Mainly, the impact of pavement vibrator parameters such as angle, depth, and spacing on concrete consolidation are not fully known. Past work has focused on characterizing the workability of the mixture (slump test) and how the mixture flows when vibrated (V-Kelly and Box test). A better understanding is still needed regarding the amount of energy (vibration rate and paver speed) needed to properly consolidate a concrete with a given workability (possibly defined using the V-Kelly test) for a given set of paving conditions (environmental conditions, size of the head in front of the paver, etc.)

2.6.2 Numerical modeling and assessment criteria

Numerical modeling has been recognized as a convenient and feasible way to inform concrete experiments. Wherein, mesoscale modeling of concrete offers a low-carbon, dependable framework for gaining deeper insights into concrete behavior (Fascetti et al., 2018). Mesoscale modeling, which involves simulating a three-phase material composed of aggregate, mortar, and interfacial transition zone (ITZ), serves as a direct and effective method to study the mechanics of concrete fracture, damage mechanisms, local nonlinear deformations, and the effects of aggregate spatial homogeneity on macroscopic properties (Comby-Peyrot et al., 2009). This scale primarily addresses the coarse aggregate component of concrete (Qian et al., 2016). Achieving an ideal spatial distribution of aggregates typically requires using fully realistic aggregates in concrete experiments. However, simulating real concrete experiments and their aggregate distributions has been challenging due to the randomness in aggregate shapes and sizes and the limitations imposed by the large number of particles involved (Guo et al., 2023). Therefore, Garboczi proposed spherical harmonic functions (Garboczi, 2002), and random field theory (Grigoriu et al., 2006; Mollon and Zhao, 2014a; Guo et al., 2023), to address these challenges. Spherical harmonic function expansion is an accurate method for representing three-dimensional geometries using Fourier expansions. It utilizes a complete set of orthogonal functions on the sphere, which are expanded or contracted to model the target 3D surface morphology. Garboczi utilized x-ray tomography to capture voxel geometries of aggregates, which were then mathematically modeled using spherical harmonic functions. This method provided a rigorous analysis of aggregate geometry, moving beyond simplified models like spheres (Xu and Chen, 2016), ellipsoids (Liu et al., 2014), or polyhedral elements (Thilakarathna et al., 2021). The approach allows for a detailed analysis of aggregate geometry, influencing factors such

as concrete rheology (Erdogan, 2005), packing density, and the impact of aggregate shape on concrete fracture and damage (Guo et al., 2023; Erdoğan et al., 2017). Although the mathematical representation of individual aggregates addresses many issues, the inherent randomness in aggregate morphology remains a challenge. Therefore, aggregates of sufficiently high fidelity need to be constructed based on spherical harmonic functions to ensure the accuracy of mesoscale simulations. In addition, since the concrete test results will eventually be evaluated, given that there is not a good criterion to rely on in this case, it is also important to establish a comprehensive and rational evaluation system.

3. Experimental Methodology

3.1 Experimental Setup of PaCS

The PaCS was designed to simulate the slipform paving of a 9.5-in concrete slab with a dowel bar in a dowel basket and can assess the consolidation not only after the simulation is complete, but during the simulation as well. To accurately replicate the paving process both the vibration energy and the speed of the paver are accounted for during the simulation.

To simulate paving a 10-in long and 11.25-in wide section of a transverse joint of a jointed plain concrete pavement, a form was constructed of a 0.5-in thick, transparent polycarbonate material. This material was selected because the transparency allows the researchers to visually monitor the consolidation on all sides of the specimen during the simulation from the exterior of the form. It also provides sufficient rigidity while vibration of the concrete slab section is performed. The form consists of two components. The lower component forms a 10 x 11.25 x 9.5-in section of a 9.5-in slab with a doweled transverse joint that will be “paved” during the simulation. It contains a 3D-printed dowel basket and an acrylic 1.25-in diameter dowel bar which extrudes 6 in into the middle of the form from the front of the apparatus and is centered 4.75 in up from the bottom. The dowel bar extends 3.5 in outside of the front of the form. The upper component is a detachable section that is used to extend the height of the lower component 6 in above the top of the slab. This is used to simulate a 6-in head of concrete over the vibrators on the paver during the paving process. Handles are attached to both the upper and lower components of the form so the upper form can be lifted off the top of the lower form more easily upon completion of the simulation. A photo of the novel PaCS apparatus is shown in **Figure 14**, with dimensions in **Figure 15**.

The PaCS was designed to quantify the energy imposed by a vibrator on a paver during the paving process. To do this, a vibrator is extended through a circular channel located on the outside of the back of the form. The vibrator shaft has a collar attached 6.5 in from the tip. This ensures the vibrator is inserted in the exact same location and the exact angle during each simulation. The channel is 0.9 in long and has a diameter of 1.75 in. The channel is on a 15-degree angle from the plane of the surface of the slab. This is representative of the angle of the vibrators mounted to slipform pavers (Jaworski, 2022). A rubber flash is placed over the circular hole in the form where the channel is attached to prevent concrete from flowing out of the form during the vibration process and as the vibrator is removed. The speed of the paver is simulated by controlling the rate at which the vibrator is inserted into and extracted from the specimen as well as the duration at which it is maintained in the specimen. To help the operator manually insert and extract the vibrator at the desired speed, different colored lines were scribed onto the vibrator shaft so the depth of penetration could be monitored. The different colors correspond to different paving speeds, which are farther or closer together depending on the speed used for each simulation. These lines along with a stopwatch are used to help maintain the

target rate of insertion and extraction of the vibrator shaft.

Most commercially available vibrators operate at much higher frequencies (167 to 233 Hz) than paving vibrators. Therefore, a vibrator was manufactured specifically for this purpose by Minnich Manufacturing, Inc. It is a CSV Flex Shaft motor equipped with a 1.125-in head. This is a variable-frequency vibrator which will vibrate at a user-specified frequency between 0 and 233 Hz. The system also logs vibration signal data from the motor when in use. The CSV Flex Shaft allows the researchers to conduct multiple tests of varying vibration frequencies all with one system.

It is important to monitor the spatial variation of energy throughout the slab section during the simulation to quantify the energy used to produce the level of consolidation achieved in each simulation. Accelerometers were used for this purpose. Accelerometers were attached to the end of three separate steel rods that extended into the lower component of the form. The first rod extends 4 in in from the front of the form to the top of the bottom bar of the dowel basket. It is centered 2.8 in off the left edge of the form and 0.5 in up from the bottom of the form. The second accelerometer rod also extends 4 in in from the front of the form to the top of the top bar of the dowel basket and is centered 2.75 in off the right edge of the form and 4.3 in up from the bottom. The third accelerometer rod extends 5.6 in into the form perpendicular to the dowel bar, on the right side. The rod is centered 4.25 in from the front edge of the form and 3.3 in from the bottom of the form. These have been defined as locations 1, 2, and 3, respectively. An accelerometer is also attached to the shaft of the vibrator. This is used to define the actual input frequency for each experiment so any reduction in wave signal amplitude, or damping, caused by the fluidity of the concrete and/or friction around the obstructions within the slab can be quantified. Quantifying the damping effect can provide a better understanding of the true mobilization of the fluid concrete compared to what was expected given the specific set of paving parameters.

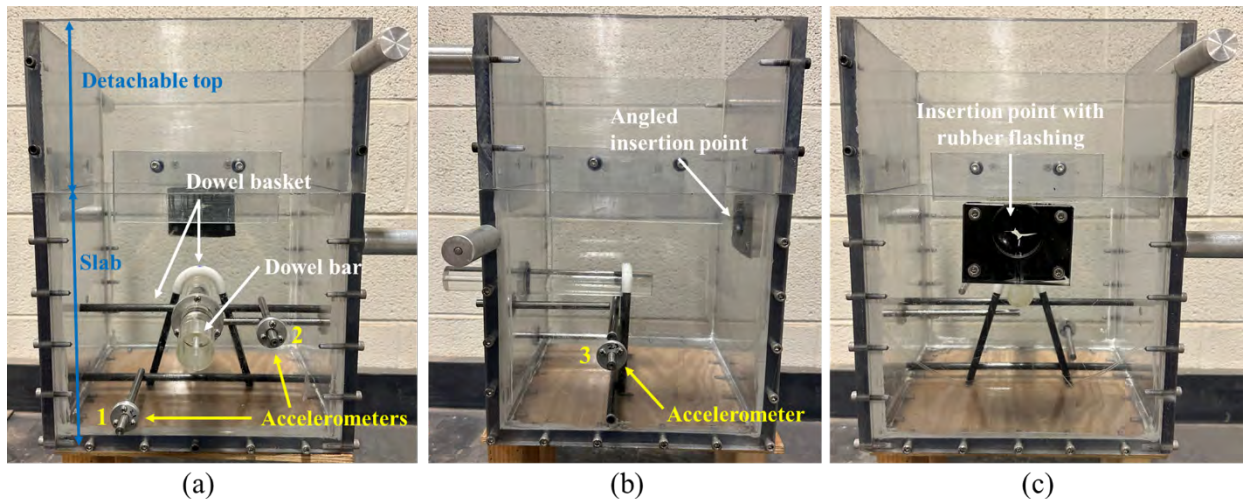


Figure 14. Photos of the PaCS apparatus, (a) Front view, (b) Side view, (c) Back view.

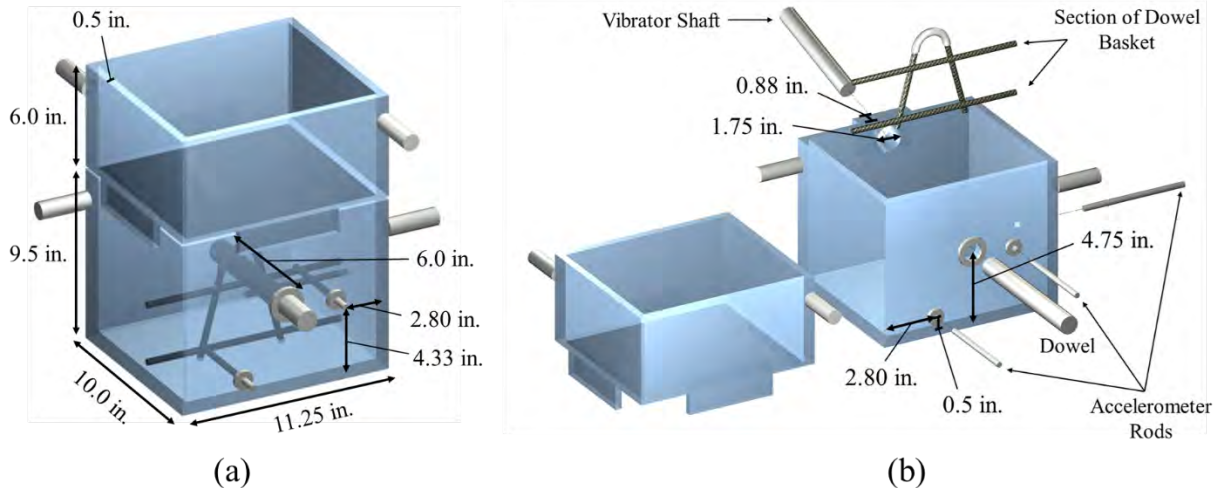


Figure 15. Schematic of the PaCS apparatus, (a) assembled apparatus, (b) apparatus components.

The goal is to be able to assess the consolidation both during and after the simulation is complete. To monitor the consolidation during the simulation, four Akaso EK7000 cameras are mounted to a frame constructed around the form (**Figure 16**). A camera is mounted on each of the sides of the frame so that the flow of the concrete around the sides of the dowel bar can be captured during the simulation. Two cameras aligned vertically are mounted to the top of the frame in the center of the form to record the top surface of the concrete during consolidation. This configuration was designed to facilitate the use of stereo vision for extracting the 3D information from the video image of the top of the specimen during the simulation.

The ability to generate a virtual reconstruction of the specimen makes it possible to quantitatively assess consolidation after the completion of the simulation. The reconstruction requires measuring the distribution of the aggregates and entrained and entrapped air after vibration throughout the specimen. This reconstruction was performed by slicing the hardened concrete, grinding the surface of each slice flat, and then scanning the surface on a flatbed scanner. The final grinding was performed with a 100-grit stone. Colored aggregates were used so that the location and size of an aggregate could be identified in the hardened concrete in an automated fashion during the particle tracking analysis. A different colored aggregate was used for each of four different particle sizes. The aggregates were selected so that they all had a similar shape, texture and specific gravity but also had colors that could be easily distinguished during the image processing. The various colored aggregates selected for use are shown in **Figure 17**. Again, the purpose of this analysis is to characterize the level of consolidation achieved based on the uniformity of the aggregate distribution throughout the specimen. This is particularly important around the dowel bar and basket, where aggregates have difficulty mobilizing.

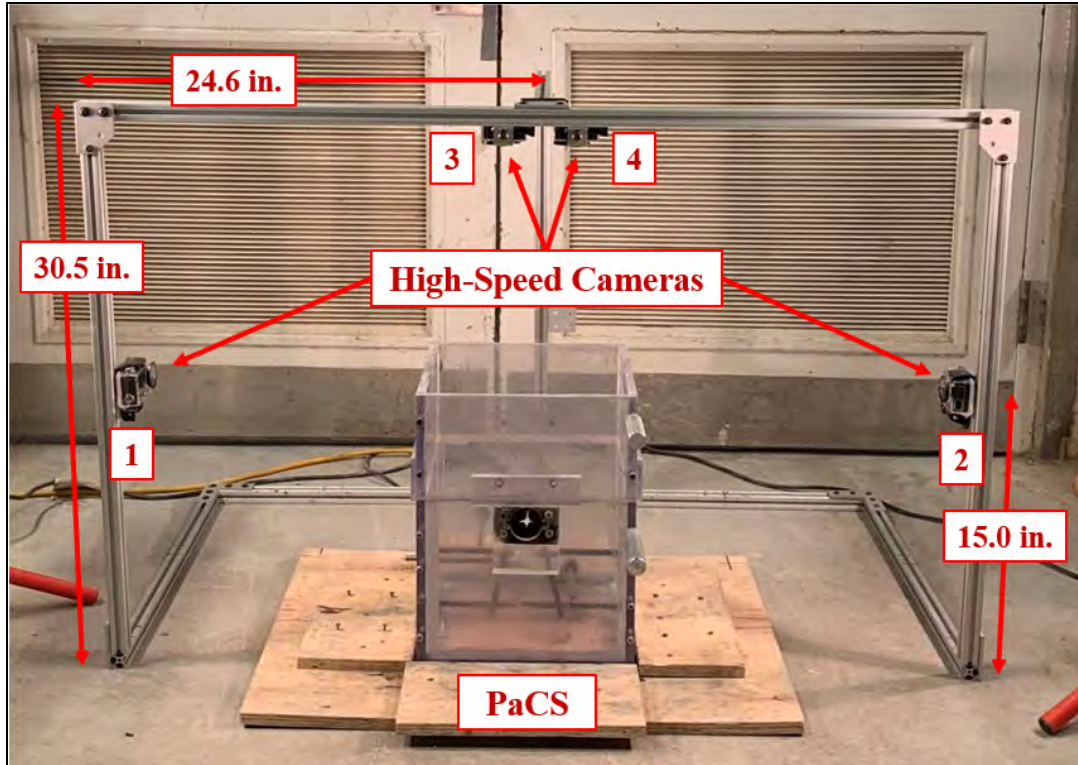


Figure 16. Elevation view of PaCS setup with cameras.



Figure 17. Colored aggregates are used to differentiate between particle sizes.

3.2 Experimental Procedure

Each PaCS simulation consists of subjecting fresh concrete to specified levels of vibration energy to quantify the degree of consolidation achieved. First, concrete is mixed according to ASTM C685M-17 (ASTM International, 2017). Concrete slump and air content are measured according to the ASTM C143M-20 and C173M-16 standards, respectively (ASTM International, 1978) (ASTM International, 2022). The PaCS form is filled by hand placing the concrete up to the surface of the detachable top component. The excess concrete is then struck off level to the top of the form. The specimen is then vibrated at a pre-determined frequency and simulated paver speed, which is accomplished by inserting and retracting the vibrator shaft at a continuous rate. The difference in vibrator frequency and simulated paver speed from each experiment translates to a difference in vibration energy. The vibrator shaft is inserted into the form and approaches the center, simulating the paver approaching the dowel bar and basket. Once the tip of the vibrator has reached the center of the form, the shaft is held for a user-defined duration, which simulates the paver moving over the basket. The shaft is then retracted from the concrete, simulating the paver leaving that area of the pavement.

Data is collected from the four accelerometers throughout the simulation to monitor energy variations throughout the depth of the pavement. The four cameras also record the consolidation throughout the simulation so the reduction in height of the fluid concrete in response to the energy input into the system can be determined. This footage allows the researchers to monitor and quantify the level of consolidation being achieved in real time. A screenshot of the video footage before and after vibration can be seen in **Figure 18**. Once the simulated paving process is complete, the difference in height from the surface of the detachable top component of the form to the surface of the consolidated concrete is measured manually with a ruler. The depth is measured over a 9.25 x 8.00-in area on a 2.67 x 3.17-in grid. This information is used to provide a rough estimate of the level of consolidation reached from the specified combination of paving parameters used in the simulation and to validate the results of the stereo vision analysis performed on the video footage. The PaCS is completed by removing the detachable top from the bottom portion of the form and screeding off any excess concrete. Once the concrete has begun to set, the acrylic dowel bar and the steel accelerometer rods are removed. The specimen is then cured with a wet burlap and demolded after 24 hours.



Figure 18. Top view of test specimen (a) before and (b) after paving simulation.

The PaCS was designed such that a range of paving conditions commonly encountered in the field can be replicated. This includes a range of vibrator frequencies, paver speeds, and concrete workability conditions. Currently, six simulations have been performed representing different combinations of these three parameters. The factors considered for each simulation are shown in **Table 4**. Each of these values were selected because they are typical for what is commonly seen in slipform paving projects. Vibrator frequencies routinely used in paving projects range from 60 to 133 Hz (PennDOT, 2020) (IowaDOT, 2015) (MnDOT, 2003) (Jaworski, Vibrations Role Surface Defects-Concrete Surface Distresses Caused By Vibrator Speed, 2017), with the most common being 108 Hz (Jaworski, 2022). Paver speed was selected to reflect typical values reported by the American Concrete Paving Association. “Slow,” “normal,” and “fast” speeds for slipform paving were reported as 3.0, 5.0, and 8.0 ft/min, respectively (American Concrete Pavement Association, 1996). Also, according to the Portland Cement Association, fresh concrete for pavements should have a slump ranging between 1.0 and 3.0 in (PCA, 2011). It should be noted that the increase in workability of the mixture was achieved by adding additional water reducer while maintaining a constant water-to-cement ratio. The control simulation for this study consists of vibrator frequency of 83 Hz, a paver speed of 5.0 ft/min, and a target slump of 1.5 in. Multiple experiments using these control conditions have been conducted to demonstrate the repeatability of the PaCS. The effects of other mixture design characteristics such as aggregate gradation, paste content, and water-to-cement ratio could also be considered in future work.

Table 4. Summary of parameters for each PaCS performed.

Parameter	Values considered
Vibrator frequency, Hz	67, 83, 108, and 133
Paver speed, ft/min	3.0, 5.0, and 8.0
Concrete slump, in	1.5 and 2.5 (+/- 0.5)

3. Concrete Mixture Design

The mixture design used meets the Penn DOT specification for a slip form paving mixture with a target slump of 1.5 in and target air content of 6%. The gradation of the coarse aggregates also conforms with Penn DOT specifications (PennDOT , 2020). The mixture design and the material properties of the aggregates used are provided in **Table 5**.

Table 5. Concrete Mixture Design.

Categories	Material Properties			Mixture Design
	Particle Diameter Range (in)	SSD Specific Gravity	Absorption Capacity (%)	Volume Fraction
Yellow Rock (F1)	1.0 to 1.25	2.61	0.62	0.01
White Rock (F2)	0.75 to 1.0	2.82	0.33	0.11
Red Rock (F2)	0.5 to 0.75	2.71	0.89	0.11
Gray Limestone (F3)	0.1 to 0.5	2.71	0.17	0.17
Sand	< 0.1	2.62	1.00	0.29
Type I/II Cement	-	3.15	-	0.11
Water	-	-	-	0.13
Air Content	-	-	-	0.06

4. Data Analysis

4.1 Vibration signal analysis

During each PaCS, four accelerometers record the vibration frequency in the fluid concrete to track vibration energy throughout the specimen. This is used to determine the damping effect of the concrete and quantify the vibration energy as a function of paver speed and vibration frequency.

First, the data is filtered to remove any signal less than 3 Hz from each accelerometer. Once the data is filtered, power spectrum plots are generated. Power spectrum plots display on the y-axis the total measured energy of the frequencies along the x-axis for the entirety of the simulation. The tallest peaks in each plot correspond to frequencies that most commonly occur at each location during the simulation. Example power spectrum plots for the accelerometer at Location 3 and the vibrator shaft are shown in **Figure 19** for a PaCS with a vibrator frequency of 133 Hz, paver speed of 5 ft/min, and the control mixture with a 1.5-in slump. Based on the peak power values, the most common frequency measured at both sensors was 133 Hz. This was expected since the vibrator frequency was set to 133 Hz. The power measured at the vibrator shaft was significantly greater than the power measured at Location 3. The difference in power is due to damping from the fluid concrete, which is sufficiently viscous to absorb some of the force of the vibration (Halliday, Resnick, & Walker, 2021).

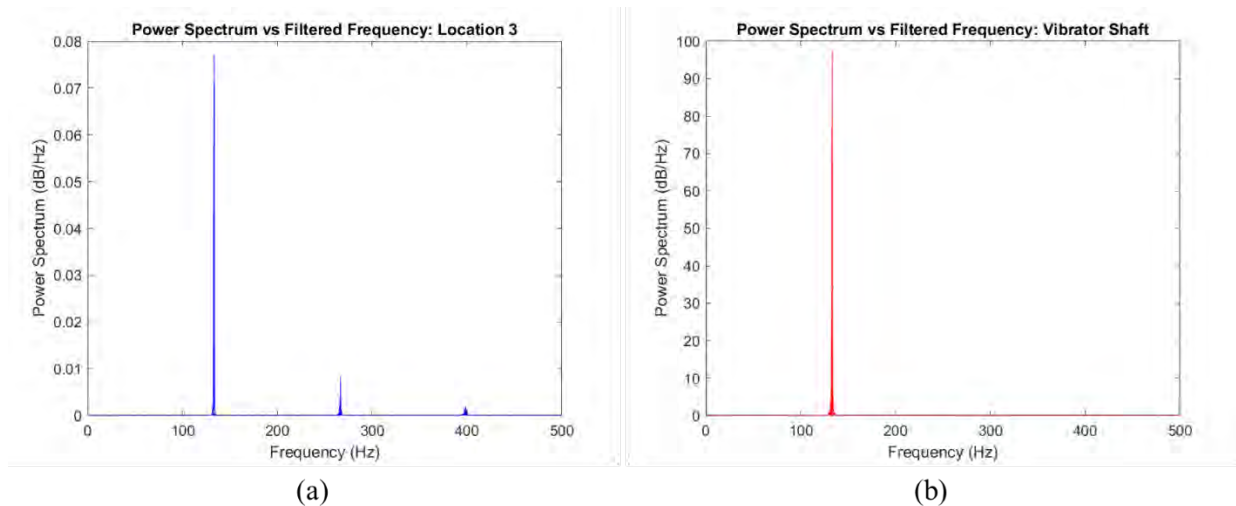


Figure 19. Power Spectrum at (a) Location 3 and (b) Vibrator Shaft.

Color spectrograms are developed for each accelerometer location to evaluate the spatial variability of energy dispersion given different paving parameters. Color spectrograms display the signal intensity of measured frequency using color on the y-axis throughout the simulation and are used to measure vibration energy variation over time (Martin P. , 2021). The color spectrograms generated for the same PaCS shown in **Figure**

19 are depicted in **Figure 20** for Location 3 and the vibrator shaft. In both spectrograms, the measured frequency remains stable around 133 Hz throughout the test, with some resonance frequencies occurring at Location 3, which indicates that the vibration energy remained constant. Additionally, the constant difference in power between Location 3 and the vibrator shaft indicates that damping was constant throughout the simulation.

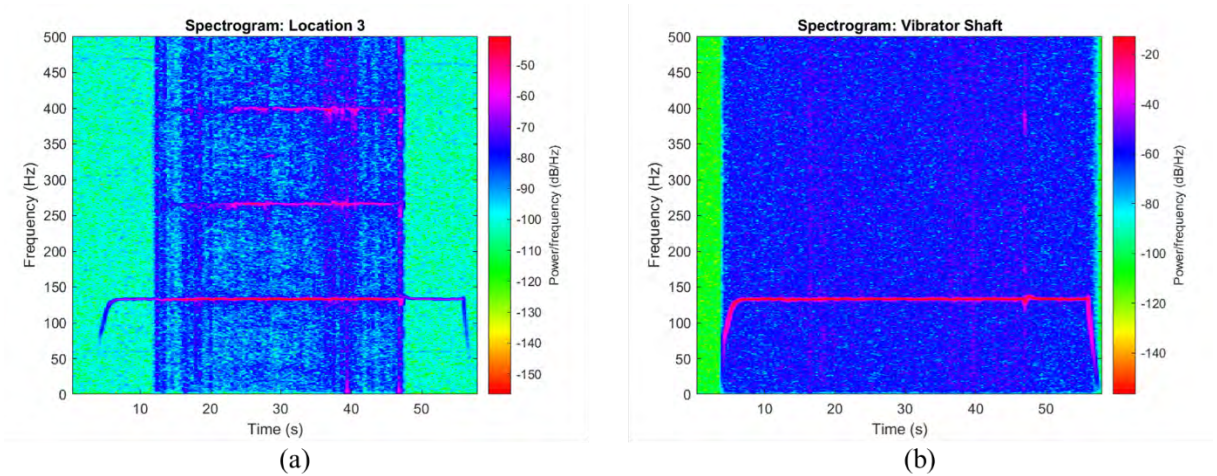


Figure 20. Spectrogram at (a) Location 3 and (b) vibrator shaft.

The repeatability of the PaCS was evaluated by conducting two shakedown simulations. The control concrete mixture was used with gravel replacing the limestone for the 0.5-inch fraction of the coarse aggregates. The paving parameters used for both simulations were a vibrator frequency of 83 Hz, a paver speed of 5 ft/min, and a slump of 2.5 in. The power spectrum from each test, from Location 3 and the vibrator shaft, are shown in **Figure 21**. Results from both simulations show that the tallest peak was observed at 83 Hz and damping occurred between the vibrator shaft and Location 3. This data demonstrates that the experimental procedure for the PaCS is repeatable.

The concrete tests conducted in this study are shown in **Table 6**. The current study mainly focuses on the effect of vibration time on the quality of concrete consolidation, so subsequent studies will be conducted based on three groups: 133 Hz-3ft/min, 133Hz-5ft/min, and 133Hz-8ft/min.

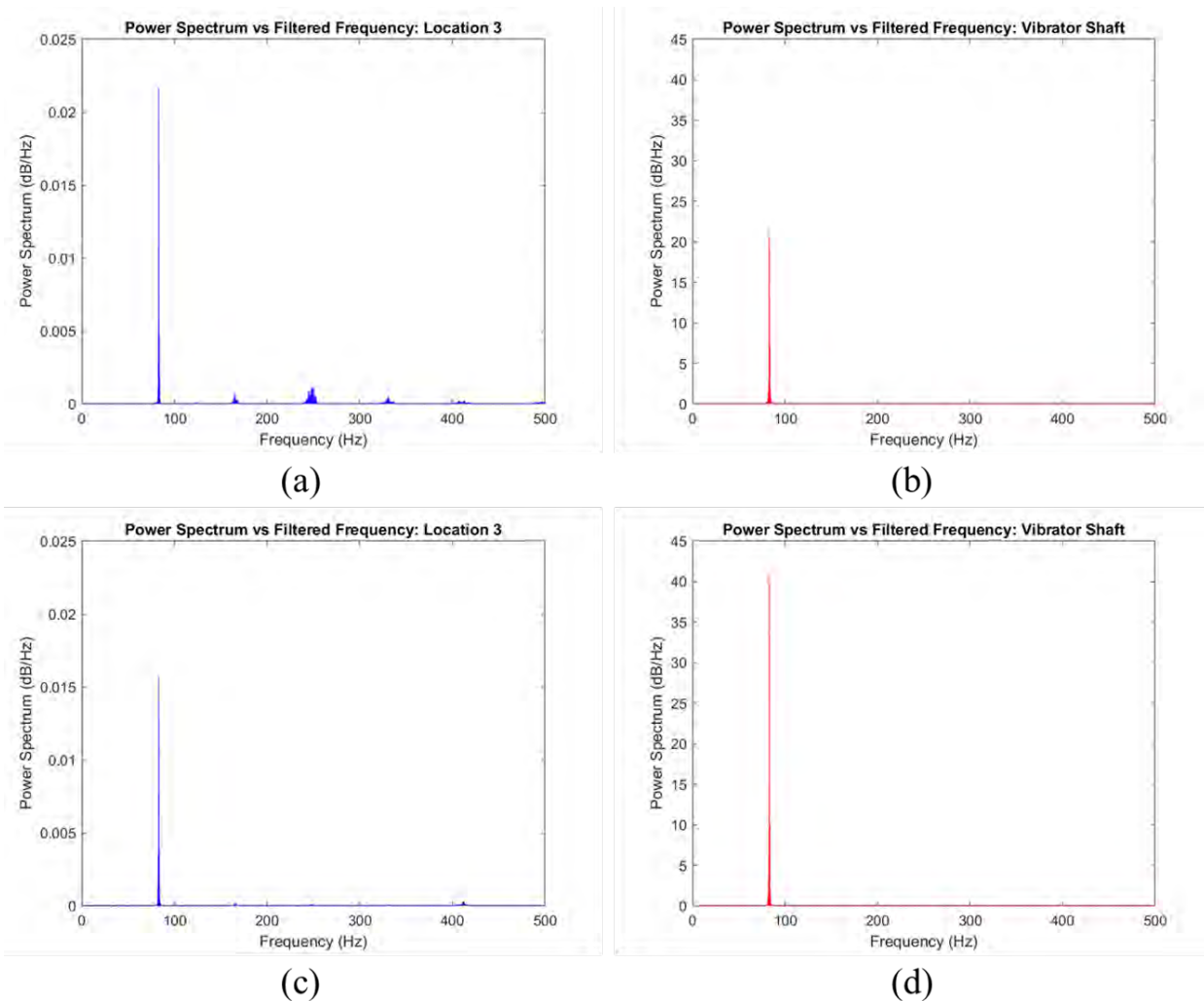


Figure 21. Power spectrum plot comparisons for shakedown replicate 1 at (a) Location 3 and (b) the vibrator shaft and for replicate 2 at (c) location 3 and (d) the vibrator shaft.

Table 6. Vibration frequency, paver speed of experiments.

Paver speed (ft/min)	Vibrator Frequency (Hz)		
	67	83	133
3	Slump: 1.25 in Air: 5.3 %	---	Slump: 1.00 in Air: 5.0 %
5	---	Slump: 1.25 in Air: 5.5%	Slump: 1.50 in Air: 5.5 %
8	---	Slump: 2.00 in Air: 6.0%	Slump: 1.25 in Air: 5.3 %

4.2 Image acquisition, CNN-based image recognition and image analysis

To assess the consolidation quality of concrete, it is essential to obtain information on the internal distribution of aggregate particles. This section describes the methods used to capture images, as well as the techniques for processing and analyzing these images.

4.2.1 Image acquisition

The hardened concrete samples are sectioned horizontally to produce images of the concrete cross-sections. **Figure 22** illustrates the technique used to capture these images. The peripheries of the hardened concrete samples are trimmed as shown in **Figure 22(a)** to eliminate any effects from the mold walls on aggregate distribution. The surfaces are then smoothed using a 100-grit polishing pad and scanned to acquire raw 2D images.

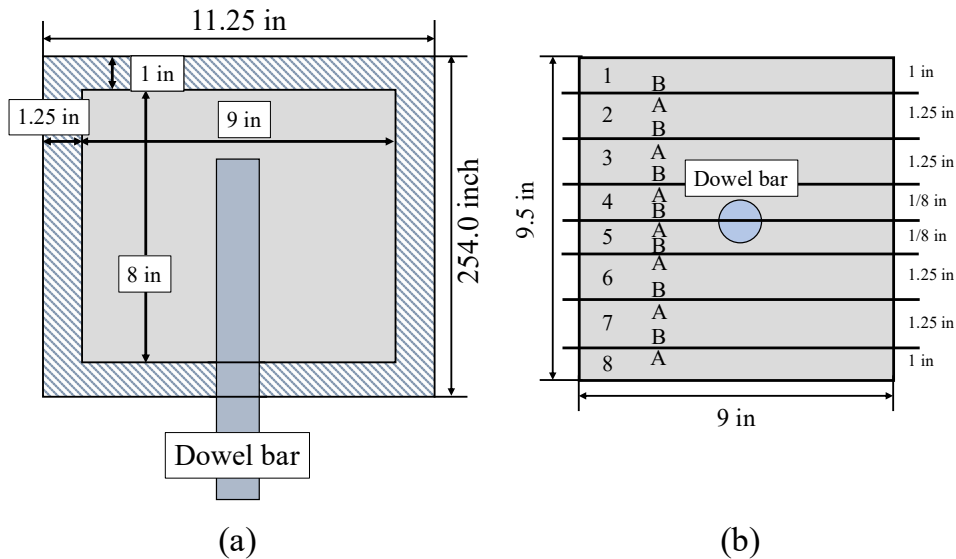


Figure 22: Slicing to acquire concrete images, (a) removal of external faces of the specimens, (b) schematic of slicing protocol.

4.2.2 CNN-based image recognition

Recent advancements in research have enabled the segmentation of features in untrained images using a pre-trained image segmentation model known as the Segment Anything Model (SAM) (Kirillov et al., 2023). Unlike traditional CNNs that focus on

recognizing specific features, SAM primarily segments objects by identifying their boundaries. This object segmentation, which utilizes stability coefficients, allows for the creation of comprehensive aggregate masks (Kirillov et al., 2023). This enables it to conduct precise and controlled image segmentation without relying heavily on pre-labeled image data, and it is even capable of segmenting and extracting air voids as small as approximately 0.04 in in diameter (Zha et al., 2023; Yan et al., 2024a).

For instance, **Figure 23** illustrates how image segmentation, recognition, and extraction are performed. The SAM model generates sufficient segmentation, producing 6348 masks as shown in **Figure 23(b)**, ensuring that each aggregate with volume exceeding $2 \cdot 10^{-4} in^3$ is adequately covered. The color beneath each mask and the color stability factor are analyzed to identify the specific color of each aggregate. These colored aggregates are then extracted and combined to form a digitally reconstructed image as displayed in **Figure 23(d)**. The processing of each image takes merely 10 minutes on a workstation equipped with an Intel i7 12700 KF, 32GB of RAM, and a GeForce RTX 3070Ti GPU. These digitally reconstructed images are utilized for further analysis of aggregate distribution as outlined in the subsequent section.

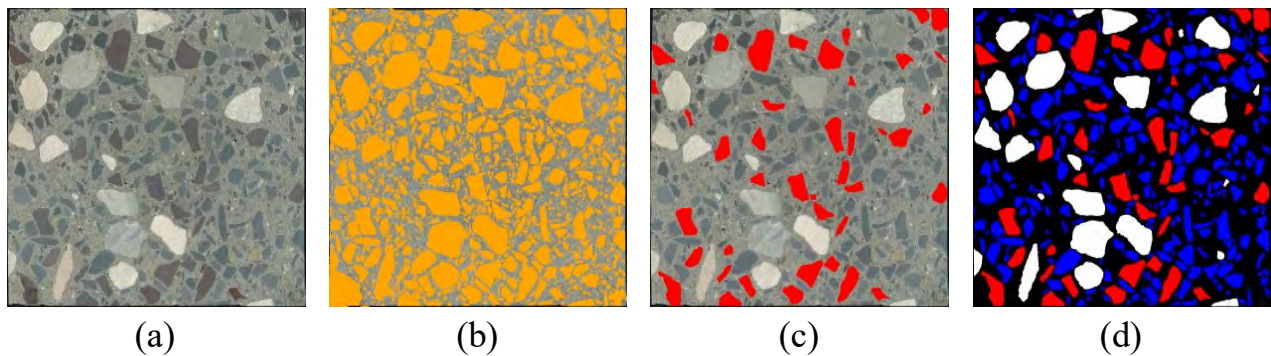


Figure 23: Example to acquire the reconstructed digital image, (a) slice 1-B plane, (b) 6348 masks for all segmented objects, (c) specific mask extraction, (d) digital image reconstruction.

4.2.3 Image analysis

4.2.3.1 Assessment of concrete consolidation

The evaluation of concrete consolidation in this study is dependent on various aggregate sizes, which typically constitute 30-60% of the concrete by volume and significantly impact its mechanical properties (Brisard et al., 2020; Yilmaz and Molinari, 2017). The analysis of aggregates encompasses examining their natural characteristics, homogeneity, dispersion, and three-dimensional spatial distribution, all while distinguishing between different aggregate classes (Yan et al., 2024b; Han et al., 2016). The methods used and initial findings are detailed using the 8000 Hz, 3 ft/min slice 1b image; for comprehensive details on all experiments and their correlation with DEM simulations, see **Section 4.5**. It is important to note that this article focuses solely on the study of coarse aggregates (specifically, F1, F2, and F3 aggregates); fine aggregates are not considered in this analysis.

4.2.3.2 Aggregate properties analysis

The analysis of aggregate properties involves examining the extrinsic morphological features from digitally reconstructed images to determine if the natural characteristics of aggregates influence vibration effects and to verify the accuracy of aggregates modeled using spherical harmonic functions.

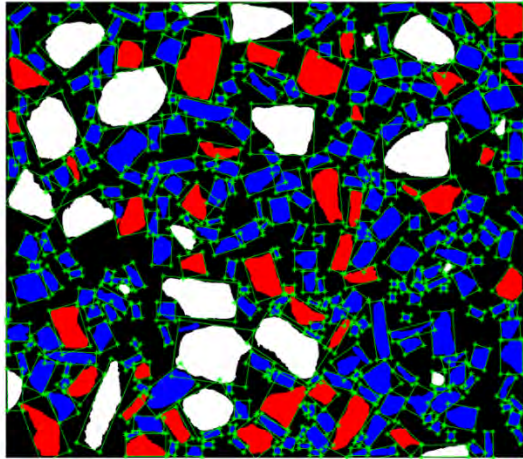
Figure 24 illustrates the scope of aggregate property analysis, including the size, aspect ratio, and orientation of aggregates. Initially, the minimum bounding box for each aggregate is derived from the digital image, providing the length (L) and width (W) measurements for each. L is designated as the size of the aggregate, with statistical outcomes displayed in **Figure 24(b)**. The data indicate a distinct size variation across different grades: more than 90% of F3 aggregates are less than 0.50 in in size; F2 aggregates mostly range from 0.50 - 0.71 in, indicating more uniformity; F1 aggregates are the largest, with only 25% under 0.83 in, showing greater size variability. The observed discrepancy between the dimensional statistics curve and the actual sieve curve suggests that even though the sieve curve uses both width and height rather than the longest side, horizontal sections generally yield smaller aggregate sizes. The minimum dimensions for each aggregate class are marked with vertical dashed lines, showing that the cuts reduce the dimensions of F1 and F2 aggregates by about 30% and 50% of their longest side, respectively.

The aspect ratio, calculated as L/W , indicates roundness—the closer the ratio is to 1, the more cubical the aggregate. As depicted in **Figure 24(c)**, the aspect ratios across different aggregate grades are not markedly distinct. The aspect ratio for F3 aggregates predominantly falls within the 1-2 range, comprising 75% of the total. Despite significant differences in size and quantity, F2 and F3 aggregates show similar statistical distributions, suggesting morphological resemblances. F1 aggregates typically show a

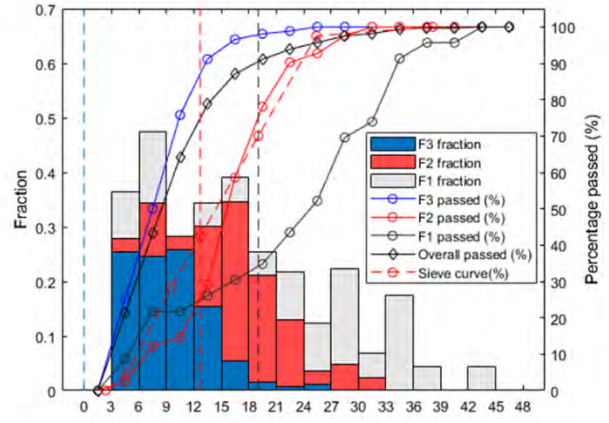
narrower range in aspect ratios, with 80% falling within the 1-2 range. Generally, the aspect ratio decreases with an increase in aggregate size, with F1 and F2 aggregates displaying more significant statistical variations due to quantity differences.

Aggregate orientation is defined by the angle between the major axis of the ellipse, which has equivalent second-order moments as the aggregate, and the horizontal plane, varying from -90 to 90 degrees. Orientation statistics in **Figure 24(d)** reveal no significant directional trends among the various aggregate grades, but minor fluctuations are observed in F1 and F2 aggregates due to their limited quantities. Although some aggregates tend to align within specific directional ranges, this is attributed to edge aggregates more likely adopting horizontal or vertical orientations.

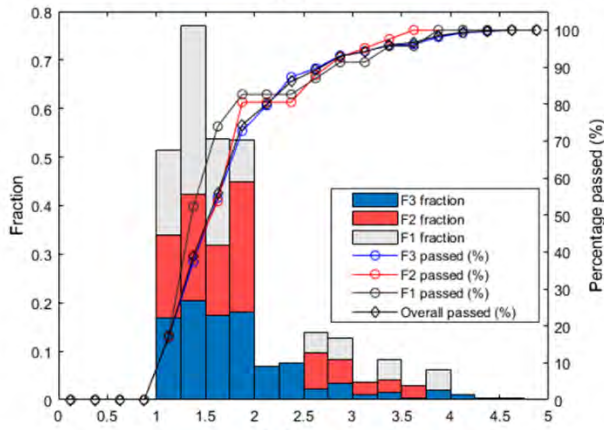
Further investigation into the correlation between aggregate properties is presented. A polar plot illustrating the relationship between aggregate area, aspect ratio, and orientation is shown in **Figure 24(e)**. F3 aggregates display the highest dispersion, while the aspect ratios of F2 and F1 aggregates predominantly range from 1-2. Correlation coefficients detailing the relationships between these properties are listed in **Table 7**. There is little to no correlation between the area of an aggregate and its orientation, whereas the aspect ratio tends to decrease as the aggregate area increases.



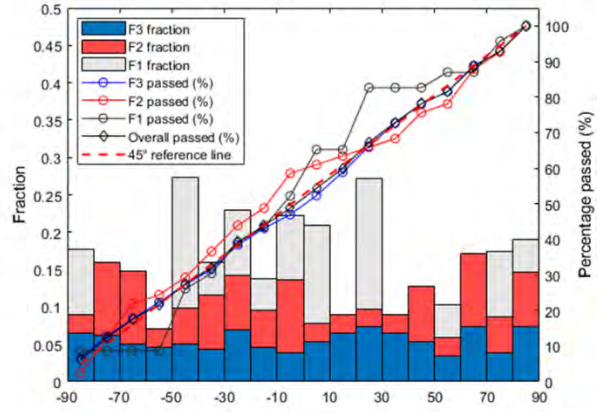
(a)



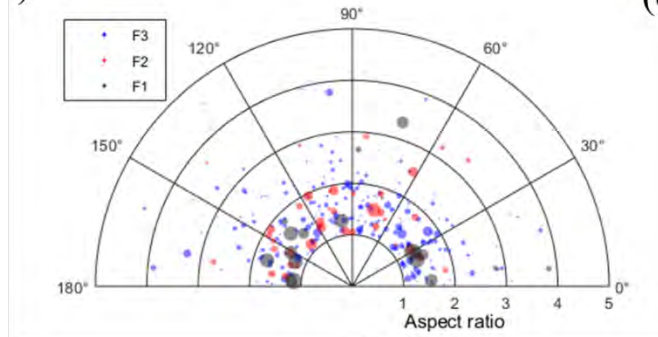
(b)



(c)



(d)



(e)

Figure 24: Aggregate property analysis, (a) Minimal bounding box, (b) Aggregate size (mm), (c) Aspect ratio, (d) Aggregate orientation ($^{\circ}$), (e) Area, aspect ratio, and orientation polar plot of aggregates.

Table 7. Correlation coefficients of aggregate properties.

Categories	Orientation	Aspect ratio	Area
Orientation	1	-0.1049	-0.0307
Aspect ratio	-0.1049	1	0.1446
Area	-0.0307	0.1446	1

4.2.3.3 Aggregate homogeneity analysis

The assessment of aggregate uniformity is based on comparing the area ratio of each aggregate class within an image to its designed ratio; greater closeness to this ratio indicates a more uniform distribution. As illustrated in **Figure 25**, the area ratios for each aggregate grade are determined by segmenting the image into nine equal sections (3x3 grid). **Figure 25(b)** shows that the area ratios for each class oscillate around their corresponding volume ratios, indicated by the reference dashed line. Due to its smaller size and higher prevalence, the F3 aggregate demonstrates the most consistency. In contrast, the larger F1 and F2 aggregates exhibit notable variability, particularly in specific sections such as areas 6 and 8 (see **Figure 25(b)**).

Furthermore, the inclusion of a dowel bar and basket typically reduces aggregate content in the middle and bottom of the concrete specimen. Consequently, the areas affected by these obstructions have their ratios adjusted by multiplying by a factor equivalent to their volume ratio of 0.41 for appropriate normalization to account for the space consumed by the dowel and basket.

To approximate the homogeneity of the aggregate distribution in three dimensions, an analysis overlaying the area ratios from 14 image layers is conducted. This method helps reconstruct a three-dimensional perspective of aggregate uniformity across the specimen.

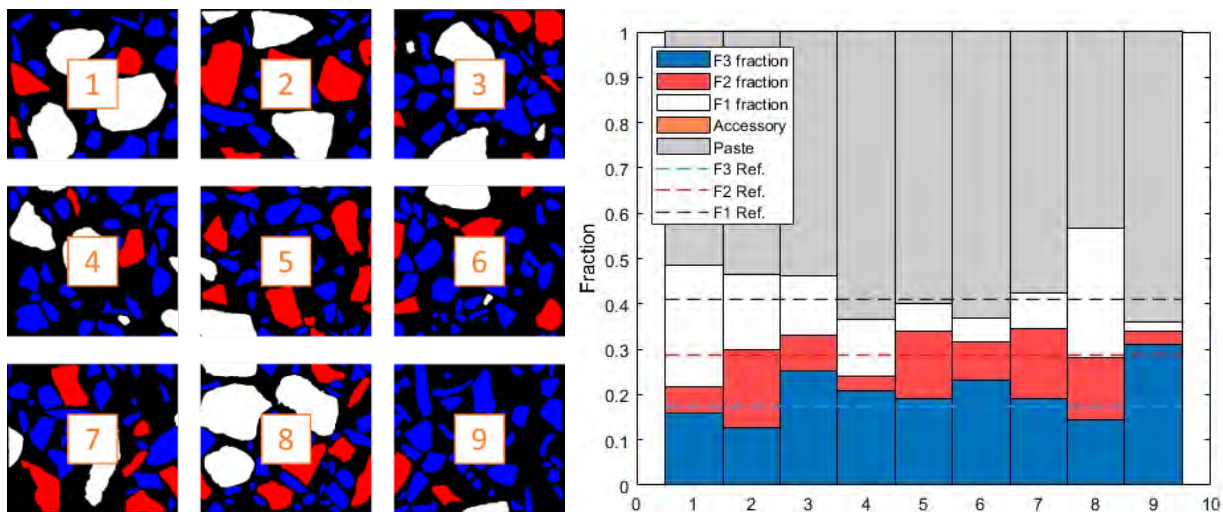


Figure 25: Aggregate homogeneity analysis, (a) regional division, (b) the fraction of aggregate area.

4.2.4 Aggregate dispersion analysis

The discrete analysis of aggregates in this study evaluates the spatial relationships between aggregates by measuring the distances between them to identify instances of aggregate convergence or segregation. As depicted in **Figure 26**, the centroid of each aggregate is determined, followed by the computation of Delaunay triangles based on these centroids. Delaunay triangulation, a geometric technique, constructs triangles from sets of points ensuring that no points lie within the circumcircles of any other triangles. This method maintains the uniqueness of the triangles by adhering to the maximum-minimum angle criterion, which prevents the formation of triangles with sharp angles. Delaunay triangulation is commonly utilized in numerical analyses to explore the mechanical properties and energy transfer behaviors in concrete structures and is also applied here for discrete analysis.

Using the Delaunay triangles, the Mortar to Aggregate Ratio (MTAR) within each triangular area is calculated by counting the pixels representing the mortar and the aggregate. MTAR is defined as the ratio of mortar area to aggregate area, as seen in the shaded regions versus the remaining areas in **Figure 26(b)**.

Figure 26(c) presents the statistical analysis of MTAR values for the image. The vertical dashed lines indicate the volume ratio of each aggregate type as per the design specifications. The Root Mean Square Error (RMSE) for each aggregate type quantifies the degree of dispersion relative to the design values, with higher RMSE values indicating greater dispersion. According to **Table 8**, the RMSE value for the F3 aggregate is the lowest, suggesting a more homogeneous distribution of the mortar around these smaller aggregates. Conversely, the F1 aggregates show a more significant variance in mortar distribution, indicating less uniformity.

Furthermore, **Figure 26(d)** illustrates the Delaunay Triangles Side Lengths (DTSL), representing the distances between the centers of gravity of the aggregates. This metric visibly correlates with aggregate gradation. For the F3 aggregate, the data display a normal distribution, indicating a more consistent spread of distances with 85% of the DTSL measuring less than 1.00 in. In contrast, 88.78% of the DTSL for the F2 aggregate fell within the 0.50-2.50 in range. The mean distance between aggregates and the standard deviation of these distances are detailed in **Table 8**. Due to its lower quantity, the F1 aggregate exhibits the longest mean spacing and the highest standard deviation in spacing. Notably, despite differences in size and mean spacing, the F1 and F2 aggregates show similar distribution patterns in their statistical curves.

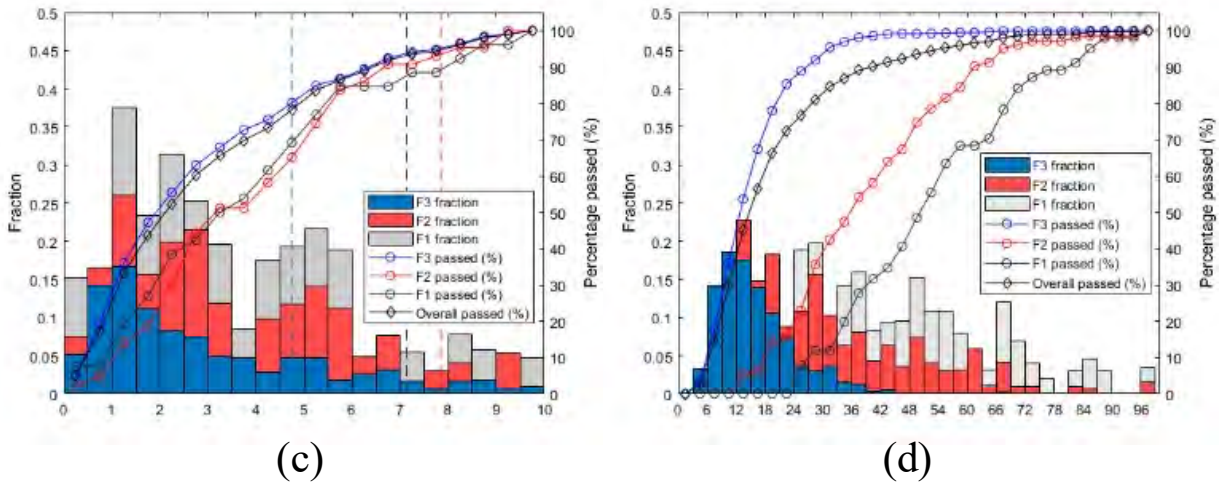
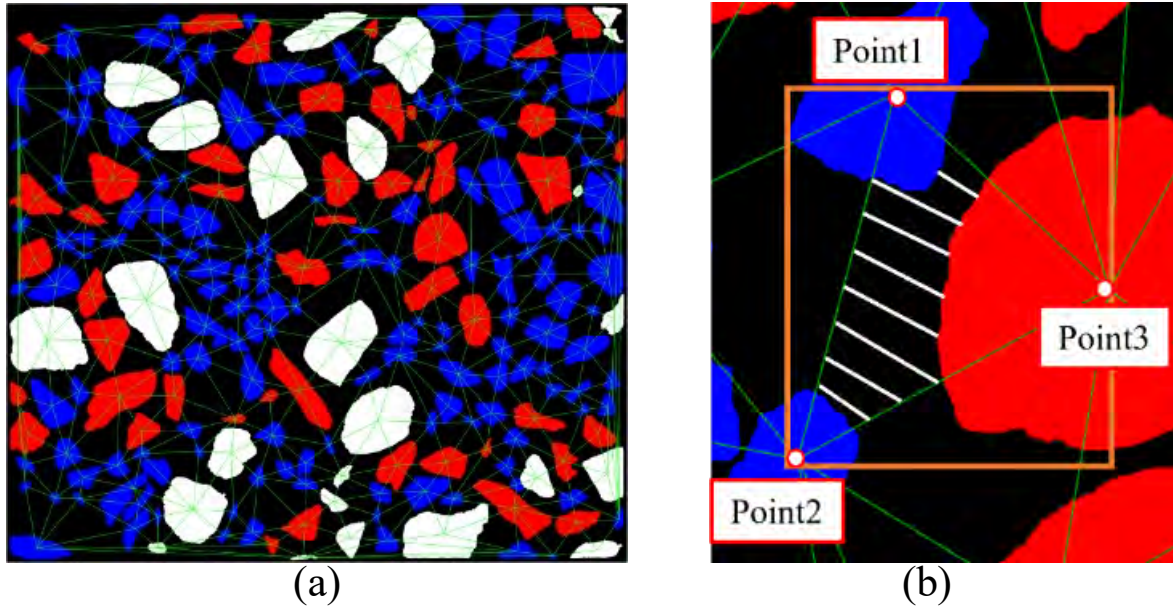


Figure 26: Aggregate dispersion analysis, (a) Delaunay Triangulation, (b) Calculation of mortar to aggregate ratio, (c) MTAR, (d)DTSL (mm) (25.4 mm = 1 in).

Table 8. Dispersion analysis

Categories		F1	F2	F3
MTAR	RMSE	25.743	13.227	6.679
	Mean	12.121	11.418	5.149
	Standard deviation	25.255	12.737	6.667
DTSL	Mean (in)	2.277	1.669	0.657
	Standard deviation	0.984	0.862	0.420

4.2.3.4 Aggregate 3D spatial distribution analysis

The 3D spatial distribution involves a rudimentary reconstruction of the true 3D center of gravity distribution of aggregates by layering the center of gravity coordinates from 14 images. This method assesses potential eccentricities resulting from vibrations. Initially, the center of gravity for each aggregate on the 2D images is determined, followed by fitting an ellipse using the least squares method. This technique calculates the center and the radii of the long and short axes of the ellipse to evaluate the positional spread of the aggregates. As depicted in **Figure 27**, there are noticeable differences in aggregate distribution levels; the center of gravity of the F3 aggregate typically aligns with the origin, and the fitted ellipse shows the smallest radii for both axes, suggesting a more uniform 3D distribution without noticeable eccentricity. In contrast, the centers of gravity for F1 and F2 aggregates are also near the origin but exhibit wider dispersion with larger radii on the short axes. Additionally, the presence of a dowel bar influences the slice-4B position, showing clear eccentricity. This issue, commonly encountered during slip paving (Voigt et al., 2010), necessitates further evaluation. This approach outlines the method for assessing the uniformity of the 3D spatial distribution of aggregates, providing a foundation for future research in this area.

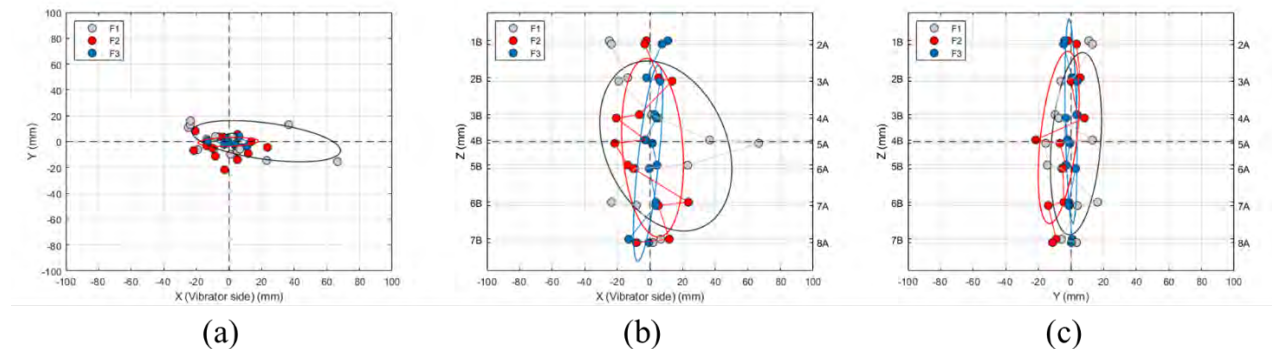


Figure 27: Example of the spatial distribution (Exp.1). (a) Top view, (b) Front view, (c) Side view (25.4 mm = 1 in).

4.3 Mathematical representation of aggregate morphology based on spherical harmonic expansion

This section outlines the methodology for collecting aggregate morphology data and the mathematical representation of aggregates. Utilizing multi-scale control, a substantial number of "virtual aggregates" are generated. These virtual aggregates mimic the morphometric properties of actual aggregates and are intended for use in subsequent mesoscale modeling of concrete.

4.3.1 Aggregate morphology acquisition

Previously, capturing the geometry of individual aggregates required the use of costly X-ray imaging facilities, where specialists would scan aggregates to produce dense 2D images. These images were then stacked to create 3D voxel structures, which were refined using various surface smoothing algorithms (Garboczi, 2002; Yang et al., 2013). This method was not only expensive but also limited in its application due to its complexity and the specialized equipment required.

In this study, a more accessible and efficient method is adopted using a laser scanner to capture the surface structure of aggregates. Specifically, Faro's Quantum Max Laser Scan Arms were employed, featuring an 8-axis structure that provides significant flexibility and ease for 3D scanning. The device meets the ISO 10360-8 Annex D specifications, ensuring non-contact measurements with an accuracy up to 0.001 in (FARO laser scan arm, 2024). This scanning process is supported by Geomagic studio software, which facilitates the quality checking of the geometric model, correction of outliers, and ultimately the export of the model in a stereolithography (.stl) format for straightforward manipulation. As shown in **Figure 28**, laser scanning achieves satisfactory fidelity, offers cost-effectiveness, and enhances maneuverability.



Figure 28: Aggregate morphology acquisition, (a) real aggregates (left limestone-01: 0.55 x 0.16 x 0.67 in; right white marble-04: 1.1 x 0.67 x 1.4 in), (b) scanned aggregates (left limestone-01: 6,801 vertices and 13,589 faces; right white marble-04: 30,502 vertices and 61,00 faces).

4.3.2 Virtual aggregate generation based on random radius field

For a mathematical representation utilizing spherical harmonic functions, the shape of the input must first be parameterized. This involves mapping the coordinates of discrete surface vertices from a Cartesian coordinate system to a uniformly continuous grid of spherical coordinates, $r(\theta, \varphi)$. The transformation is illustrated in **Figure 29**, where r represents the distance from the geometric center to a surface vertex, φ is the polar angle within $(0, \pi)$, and d is the azimuthal angle within $(0, 2\pi)$. The geometric center serves as the origin for the local polar coordinate system. Thus, any vertex $u(x, y, z)$ on the input shape can be expressed by **Equation 2**.

$$\begin{aligned} x_{i,j} &= r_{i,j} \sin(\theta_i) \cos(\phi_j) \\ y_{i,j} &= r_{i,j} \sin(\theta_i) \sin(\phi_j) \\ z_{i,j} &= r_{i,j} \cos(\theta_i) \end{aligned} \quad (2)$$

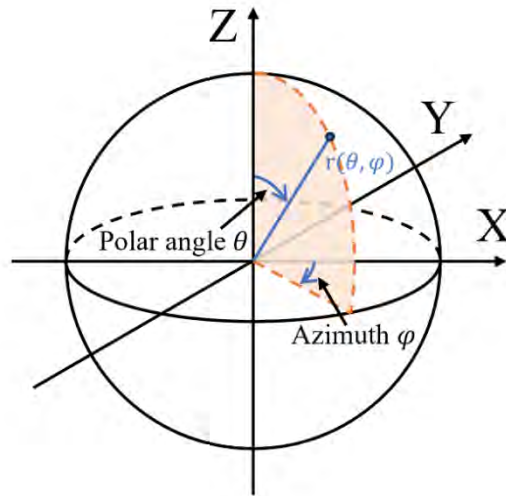


Figure 29: Spherical coordinate system.

The fundamental equation in spherical harmonic function analysis is presented as **Equation 3**, where θ ranges from 0 to π and φ from 0 to 2π . Here, A_l^m are the Fourier coefficients and $Y_l^m(\theta, \varphi)$ denotes the spherical harmonic function. The variable l denotes the degree of the function, and m its order; l dictates the maximum number of expansion terms in the spherical harmonic series, with a higher l leading to a more precise mathematical representation of the shape. According to the Sturm-Liouville problem, to find non-trivial solutions for the eigenvalues l , one must satisfy $l = 1$ to ∞ and $m < l$; assuming the maximum value of l as n . This indicates that any point $r(\theta, \varphi)$ in the spherical coordinate system can be viewed as a sum of the products of that point's

coordinates and its coefficients on the basis function of each spherical harmonic term.

$$r(\theta, \varphi) = \sum_{l=0}^{\infty} \sum_{m=-l}^l A_l^m Y_l^m(\theta, \varphi) \quad (3)$$

The spherical harmonic function is formalized as **Equation 4**, in which $P_l^m(x)$ denotes the associated Legendre function, a series of orthogonal polynomials; here, i represents the imaginary unit. This function, $P_l^m(x)$, is outlined as **Equation 5**, characterized by its degree l and order m . As depicted in **Figure 30**, the spherical harmonic functions are sequentially expanded according to their hierarchical organization, with each form representing the shape of the basis function for a specific degree and order combination; yellow color illustrates the real part, and blue color represents the imaginary part. At a degree of zero, the function describes a sphere, but as the degree increases, the morphology of the basic functions becomes more angular, enhancing their capability to capture the local intricacies of the aggregate.

$$Y_l^m(\theta, \varphi) = \sqrt{\frac{(2l+1)(l-m)!}{4\pi(l+m)!}} P_l^m(\cos\theta) e^{im\varphi} \quad (4)$$

$$P_l^m(x) = (1-x^2)^{\frac{|m|}{2}} \frac{d^{|m|}}{dx^{|m|}} \left[\frac{1}{2^{l!}} \frac{d^l}{dx^l} (x^2-1)^l \right] \quad (5)$$

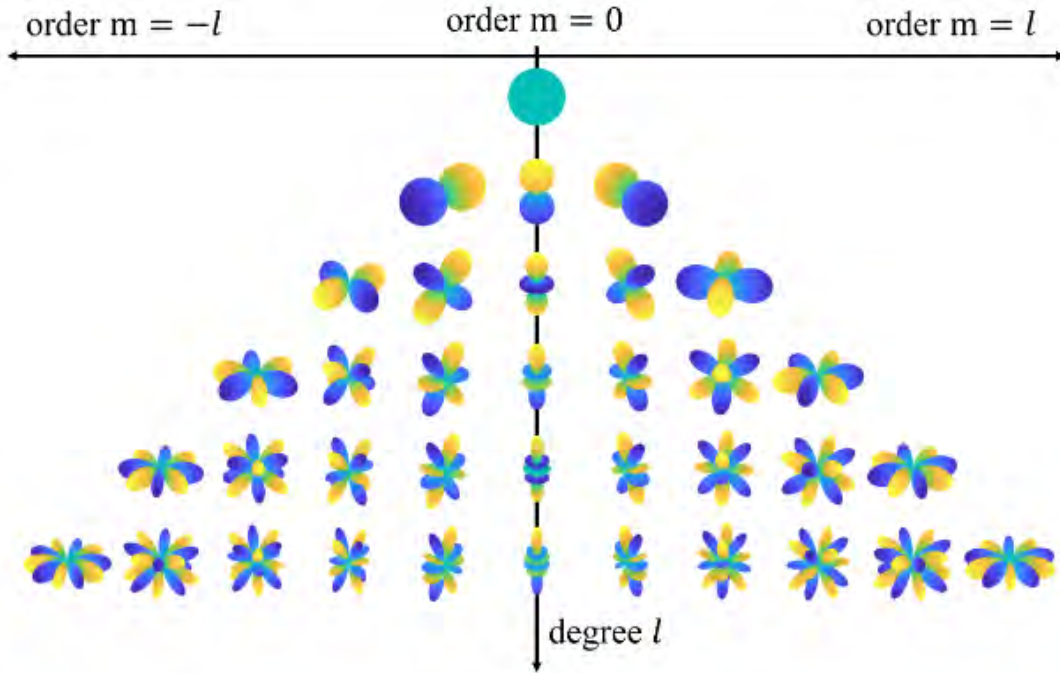


Figure 30: Hierarchy of the spherical harmonic functions.

Subsequently, to mathematically represent the aggregate, the Fourier coefficients of each basis function are calculated, denoted as A_l^m . These coefficients are typically determined through matrix operations and least squares fitting, this process will be

illustrated using an array of spherical coordinates $r_i(\theta_i, \varphi_i)$ for a sample aggregate, where $1 < i < n$ represents the total number of input points to fit Fourier coefficients A_l^m . From **Equation 3**, $y_{i,j} = Y_l^m(\theta_i, \varphi_j)$, where, $j = l^2 + l + m + 1$ marks the sequential numbering of the basic functions; $k = (l + 1)^2$ is the total sphere-harmonized basis functions, with each degree l having $2l + 1$ basis functions. Given that the number of sampling points for the aggregate exceeds $2l + 1$, this matrix can be reliably solved using least squares fitting methods. Using these coefficients, the Limestone-05 aggregate can be mathematically reconstructed as shown in **Figure 31**.

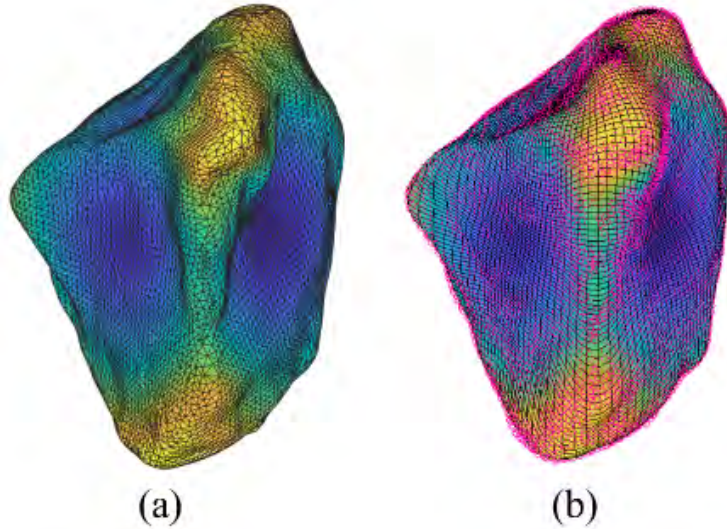


Figure 31: Mathematical reconstruction of Limestone-05 with degree $l = 20$, (a)input particle with 7078 vertices, (b) reconstructed particle (pink circle: input vertices).

To demonstrate the impact of varying degrees of spherical harmonic functions on the mathematical representation of aggregates, **Figure 32** displays how different degrees affect the representation of Limestone-05 particles. It is evident that at lower degrees ($l < 4$), there are substantial changes in the shape of the reconstructed particles. As the degree increases ($l > 8$), modifications become more focused on refining small-scale details within the particles. At a degree of $l = 22$, the spherical harmonic function nearly captures all the morphological characteristics of the input aggregate. Previous research by Zhou et al. (2018) suggests that the spherical harmonic function equation yields a unique solution at $l = 15$. In this study, to ensure the accuracy of the reconstructed aggregate, the degree l is set to 20.

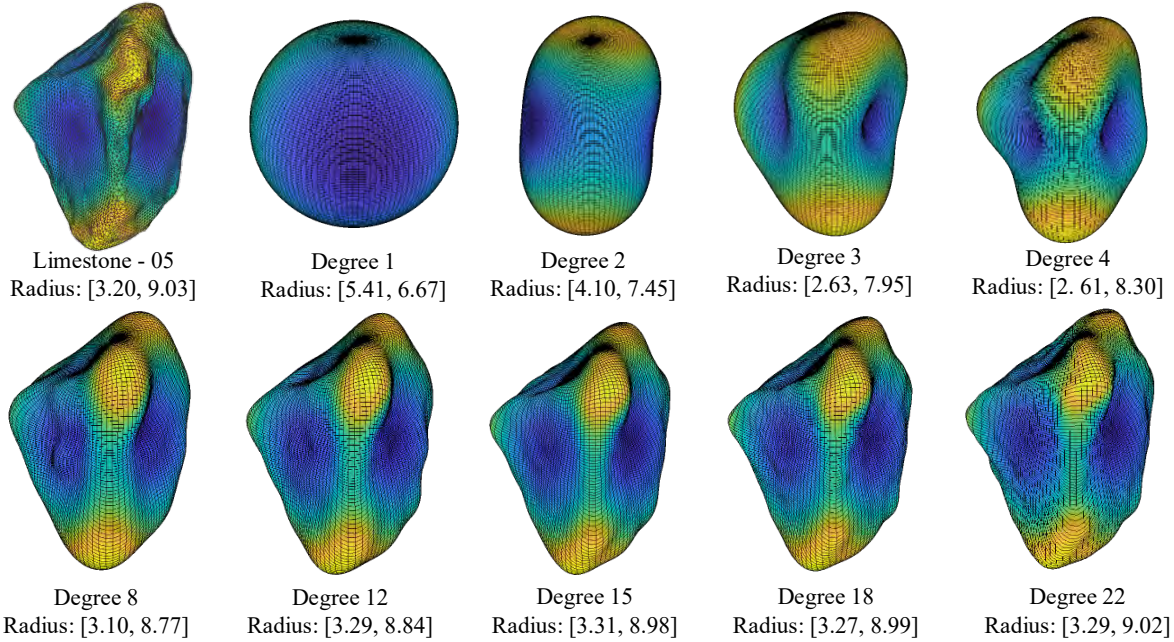


Figure 32: Mathematical representation with different maximum SH degrees of Limestone-05.

As spherical harmonic functions have proven effective for decomposing aggregate morphology and controlling the granularity of the reconstructed aggregate across various scales. This capability largely hinges on adjusting the parameters associated with each spherical harmonic basis function. Therefore, when it is impractical to individually scan each aggregate used in simulating aggregate particles, scholars naturally consider manipulating the coefficients of the spherical harmonic functions to synthesize new aggregates that resemble the scanned ones. For instance, while studies like (Wei et al., 2018, Zhou and Wang, 2017, Liu et al., 2011, Grigoriu et al., 2006) have mainly produced new particles by employing presumed random spherical harmonic function coefficients, these do not ensure similarity to the original aggregates. The work by Wei et al. (2018) and Guo et al. (2023) has utilized the capacity to decompose morphological components of aggregates with spherical harmonic functions and random field theory to create virtually new aggregates with controlled similarity. Nevertheless, current research primarily focuses on generating sand particles and encounter limitations due to the least-squares method, which does not effectively generate elongated and flat aggregates.

The creation of a new aggregate involves generating a new radius field, namely, constructing a new aggregate radius field based on a reference radius field and random field theory. Assuming $r(x)$ is the radius at point: $x = \{(\theta, \varphi)\}^T$ on a random aggregate, then an $N \times N$ size continuous radius random field can be formed as $I(x, \omega) = \{r(x_1, \omega), (x_2, \omega), \dots, (x_{n \times n}, \omega)\}^T$, where ω denotes a sample from an arbitrary aggregate. Given that the aggregate form is naturally shaped through processes like friction, splitting, and crushing, it is assumed that the radius field $I(x, \omega)$ follows a multivariate Gaussian distribution.

For any two points on the aggregate surface, $x_1 = (\theta_1, \varphi_1)^T$ and $x_2 = (\theta_2, \varphi_2)^T$, their radii are $r(x_1)$ and $r(x_2)$, and their autocorrelation function can be expressed as **Equation 6**.

The standard deviation is denoted by σ , and the covariance operator $cov(\xi_1, \xi_2)$ for two random variables ξ_1 and ξ_2 can be expressed as $cov(\xi_1, \xi_2) = ((\xi_1 - E(\xi_1))(\xi_2 - E(\xi_2)))$, where $E(\cdot)$ represents the expected value operator. The radius field $I(x, \omega)$ is assumed to be strictly stationary up to the second order, ensuring that its mean μ and standard deviation σ remain constant through space (Feng et al., 2014). Additionally, as the autocorrelation function $C(\tau)$ relates only to the relative positions of two points, $x_2 = x_1 + \tau$.

$$C(x_1, x_2) = \frac{cov(r(x_1, \omega), r(x_2, \omega))}{\sigma_1 \sigma_2} \quad \forall x_1, x_2 \in D \quad (6)$$

The development of a new radius field necessitates the use of statistical parameters, μ , σ , and C from the original radius field as references. Assuming the discrete radius field $I(x, \omega)$ to be ergodic, the ensemble averages of these parameters are deduced from their spatial averages across a large number of realizations (Feng et al, 2014, Feng et al, 2016). Utilizing these reference statistics and spectral representation, a new random radius field is then constructed according to **Equation 7**.

$$I(x, \omega) = \mu + \sqrt{N_1 \cdot N_2} \cdot FFT^{-1}(\sqrt{Sx(\omega)} \exp(i\alpha)) \quad (7)$$

In this equation, μ represents the mean of the reference radius field $R_r(x)$; $Sx(\omega)$ is the autocorrelation function of $R_r(x)$, derived from the Wiener-Khinchin relation (Feng et al, 2014). The autocorrelation function C of $R_r(x)$ is modeled as a Gaussian power spectral density function, calculated via Fast Fourier Transform (FFT) based on the Wiener-Khinchin relationship. The variable α is a random phase angle uniformly distributed between 0 and 2π ; i is the imaginary unit, and $N_1 = N_2 = N$ indicates the number of grids in each direction.

$$I(x, \omega) = FFT^{-1}\{FFT_{\{R_r(x)\}} \cdot \exp(i\alpha)\} \quad (8)$$

The core of **Equation 7** lies in its ability to randomly alter the phase of the autocorrelation matrix of the original radius field $R_r(x)$ while maintaining a consistent global magnitude, achieved by introducing the random phase angle α . By incorporating the statistical parameters of $R_r(x)$ **Equation 7** is refined into **Equation 8**.

Following **Equation 8**, a new radius field created using Limestone-05 as the reference aggregate is depicted in **Figure 33**. The autocorrelation function C elucidates the correlation between radial and lateral positions of points within the radius field D , directly influencing the overall morphological representation of the aggregate. This

correlation is crucial for extracting morphological features of aggregates. **Figures 33(c-e)** compare the new radius field with the original, illustrating the similarity between the newly generated and original aggregates. **Figures 33(f-g)** display the probability density function and cumulative distribution function of the radius field, showing high congruence with the Gaussian distribution.

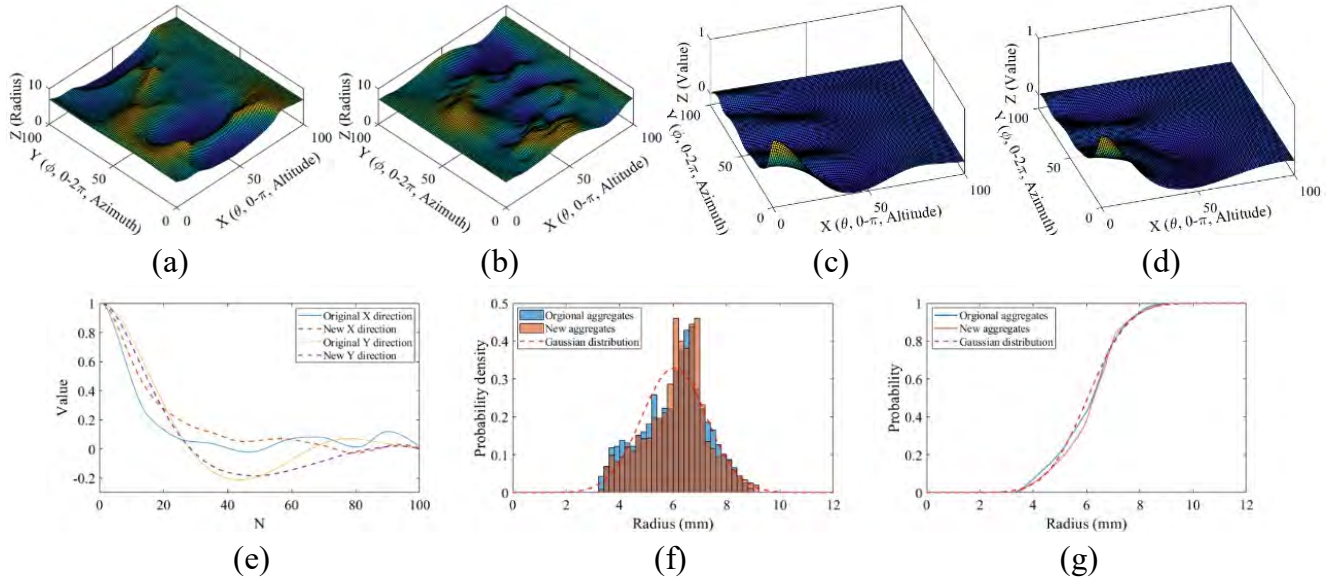


Figure 33: Generation of new radius fields. (a) reference radius field, (b) new radius field, (c) reference autocorrelation map, (d) new autocorrelation map, (e) comparison of autocorrelation functions, (f) probability density function, (g) cumulative distribution function (25.4 mm = 1 in).

4.3.3 Multi-scale aggregate morphology control

Using the previously described method, new aggregates were created with statistical parameters μ, σ , and C that are statistically equivalent to the reference aggregate Limestone-05. However, the morphology of these new aggregates distinctly differed from that of Limestone-05. This variation is attributable to the randomization of the phase angle as per **Equation 8**, which randomly alters the radius of the new radius field $I(x, \omega)$. To achieve a morphology more akin to the reference aggregate, Guo et al. (2023) suggested employing the morphological component decomposition capabilities of the spherical harmonic function. This approach involves keeping the coefficients of the lower-order spherical harmonic basis functions $\{f_{0\sim 5}\}$ unchanged while only adjusting the higher-order coefficients to maintain the principal characteristics of the aggregate, as illustrated in **Figure 34**.

This method ensures the morphology of the subject aggregate bears resemblance

to the reference. However, the introduction of the random phase angle α is still stochastic, which leads to additional complexities in the newly created aggregate that are absent in the reference aggregate. Consequently, the new aggregate produced by this method cannot definitively be said to possess similar morphological characteristics to the reference particle. Additionally, the new aggregates exhibit a pronounced oscillation effect at the center, complicating the simulation of flat surfaces typically created by splitting, as demonstrated in **Figure 34**.

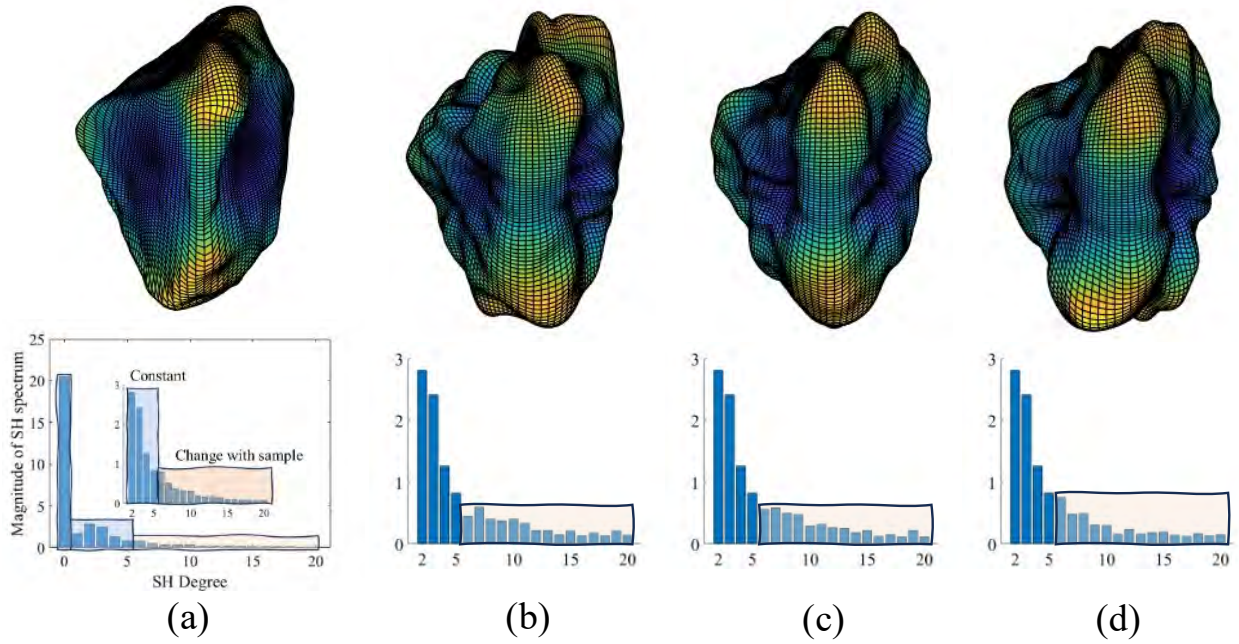


Figure 34: Use of component decomposition to control the morphology of aggregates. (a) Reference aggregate Limestone-05 and associated coefficients, (b-d) three new aggregates with the same spectra $\{f_{0\sim 5}\}$ as the reference aggregate.

To address these challenges, it is proposed to employ a novel methodology that modulates the extent of variation in the introduced phase angle α and combines down-sampling and up-sampling techniques to better control the location of random field introduction. Initially, to manage the variation range of the phase angle α , a scaling factor k is introduced, allowing **Equation 8** to be modified into **Equation 9**. This adjustment aims to generate a more realistic aggregate by precisely controlling the random variations introduced during the process. The demonstrations of controlling the scaling factor k to get different control are shown in **Figure 35**.

$$I(x, \omega) = FFT^{-1}\{FFT_{\{R_r(x)\}} \cdot exp(i\alpha/k)\} \quad (9)$$

$$I(x, \omega) = resize(FFT^{-1}\{FFT_{\{resize(R_r(x), s)\}} \cdot exp(i\alpha/k)\}, 1), \forall S \in [0,1] \quad (10)$$

This approach offers enhanced control over the magnitude of global morphological changes, resulting in more realistically shaped aggregate particles. While the previous method allows for fine-tuning of small-scale details, it does not provide control over these finer scales. Furthermore, to create more regular aggregate surfaces, this method incorporates a down-sampling technique to reduce the radius field $I(x, \omega)$ size, followed by the introduction of a random field and subsequent restoration to its original size. This adjustment adheres to **Equation 10**, where s is the scaling factor of the radius field used to determine the control range. A smaller S value corresponds to a larger control scale, in this case $S = 0.3$. The process is detailed in **Figure 35**. An additional advantage of this method is its ability to address issues such as the oscillation effect and the retention of coarse-scale morphological features of the aggregate as shown in figure, which is the challenges commonly faced with traditional methods for generating flat or elongated aggregates.

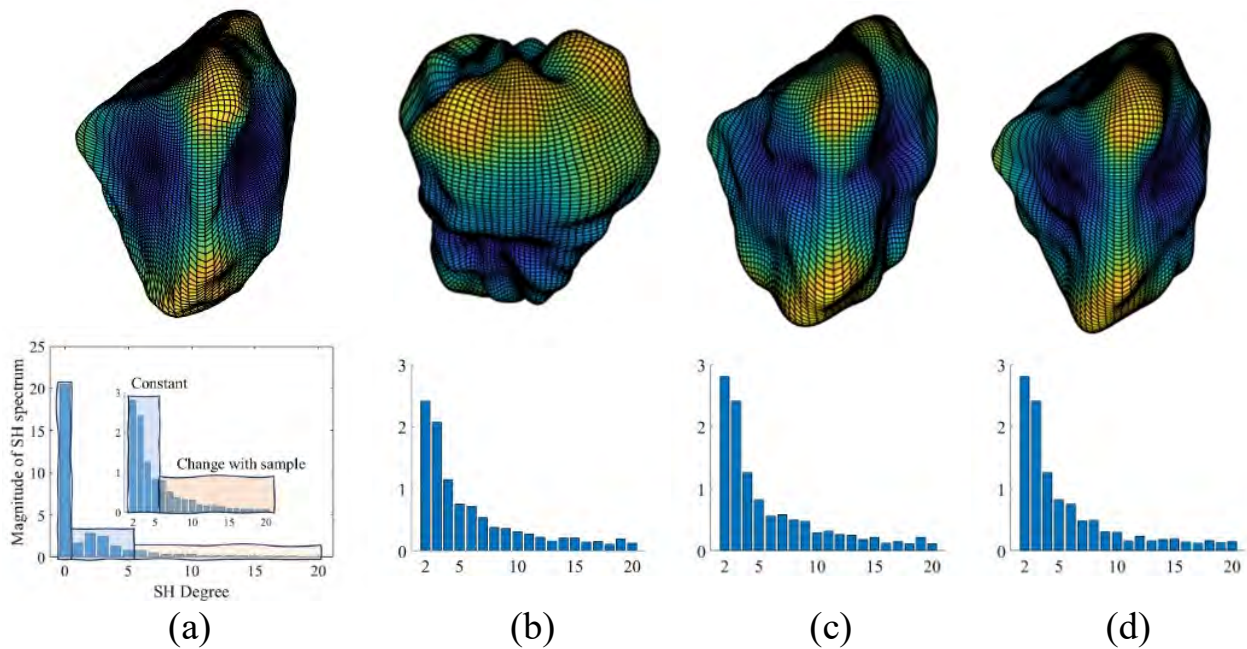


Figure 35: Generation of aggregate morphology using the phase angle control method. (a) Reference aggregate Limestone-05, (b-d) three generated aggregates.

4.3.4 Validation of aggregate with morphological index

To validate that the previously proposed method generates new aggregates with comparable morphological characteristics, this section will employ various morphological metrics to assess them across different scales. Garboczi initially introduced a method to calculate the volume and surface area of virtual aggregates using integrals when he began representing aggregates with spherical harmonic functions (Garboczi, 2002). While this method is not impacted by the resolution quality of images obtained from X-ray tomography, it is influenced by the shape of the aggregate. Moreover, the computation speed varies with the model's size, taking several minutes per aggregate for larger aggregates such as the F1 type. In this study, the dense discrete mesh from laser scanning and a chosen dense mesh selection ($N = 100$) ensure the accuracy of the mesh-based approach for calculating aggregate morphology metrics.

Common properties of aggregates such as Surface area (S) and Volume (V) can be determined using **Equation 11**, leveraging the vectorial nature of the triangular mesh. The volume of an aggregate can be computed using the scattering theorem, as outlined in **Equation 12**.

$$\begin{aligned} \forall faces_{(i)} \in D, \exists v_{(1,i)}, v_{(2,i)}, v_{(3,i)} \in faces_{(i)} \\ normal_{(i)} = cross(v_{(2,i)} - v_{(1,i)}, v_{(3,i)} - v_{(1,i)}) \\ s_{(i)} = surfacearea_{(i)} = 0.5 \times norm(normal_{(i)}) \\ S = total_{(surface\ area)} = sum(s_{(i)}) \end{aligned} \quad (11)$$

$$\begin{aligned} z(normal) = normal(i, z) \\ v_{(i)} = volume_{(i)} = s_{(i)} \cdot mean(v_{(1,i,z)}, v_{(2,i,z)}, v_{(3,i,z)}) \cdot z(normal) \\ V = total_{(volume)} = sum(v_{(i)}) \end{aligned} \quad (12)$$

The Sphericity Index (SI), defined in **Equation 13** (Clayton et al., 2009), compares the surface area of a volume-equivalent sphere (S_{eq}) to the surface area of the aggregate (S). A higher SI indicates that the aggregate shape is more spherical.

$$SI = \frac{S_{eq}}{S} = \frac{4\pi(\frac{3V}{4\pi})^{\frac{2}{3}}}{S} \quad (13)$$

The Convexity Index (CI), detailed in **Equation 14** (Zhao et al., 2020), is the ratio of the aggregate's volume (V) to the volume enclosed by the smallest convex surface around the aggregate (V_{conv}). A higher CI suggests a shape closer to convex.

$$CI = \frac{V}{V_{conv}} \quad (14)$$

The Roughness Index (RI) measures the flatness of the triangular mesh relative to the geometric center of the aggregate, as shown in **Equation 15** (Naderi and Zhang,

2019). Here, r_i is the unit vector from the i th face to the geometric center of the aggregate; u_i is the unit normal vector of the i th face; ΔS_i is the area of the i th face; and n is the total number of triangles. Larger RI values indicate a rounder, less angular surface.

$$RI = \frac{\int_S |r \cdot u| \cdot dS}{S} = \frac{\sum_{i=1}^n |r_i \cdot u_i| \Delta S_i}{S} \quad (15)$$

The Ruggedness Index (R_gI), as described in **Equation 16** (Loz et al., 2021), quantifies the ruggedness over a localized region where η measures the deviation of a vertex (x, y, z) on any face from its average surface level. Higher R_gI values denote a rougher surface.

$$R_gI = \sqrt{\frac{1}{S} \iint_S \eta^2(x, y, z) dx dy dz} \quad (16)$$

Applying the morphological metrics discussed in **Section 4.3.3** to produce 100 aggregates, with the results depicted in **Figures 36**. The findings clearly indicate that feature control can effectively maintain morphological consistency between the generated aggregates and the original samples. Furthermore, aggregates created using the phase angle control method managed to preserve the main features more effectively, which amalgamates different aggregate morphologies in a somewhat rudimentary manner.

Additionally, the robustness of the phase angle control method in producing flat and elongated aggregates was also assessed, as shown in **Figure 37**. This was done by introducing elongation indices $EI = \text{width} / \text{length}$ and flattening indices $FI = \text{height} / \text{width}$, calculated from the dimensions of the aggregates' bounding boxes. This approach confirms that a substantial number of aggregates with consistent morphology can be synthesized while only requiring scans of a limited number of original aggregates.

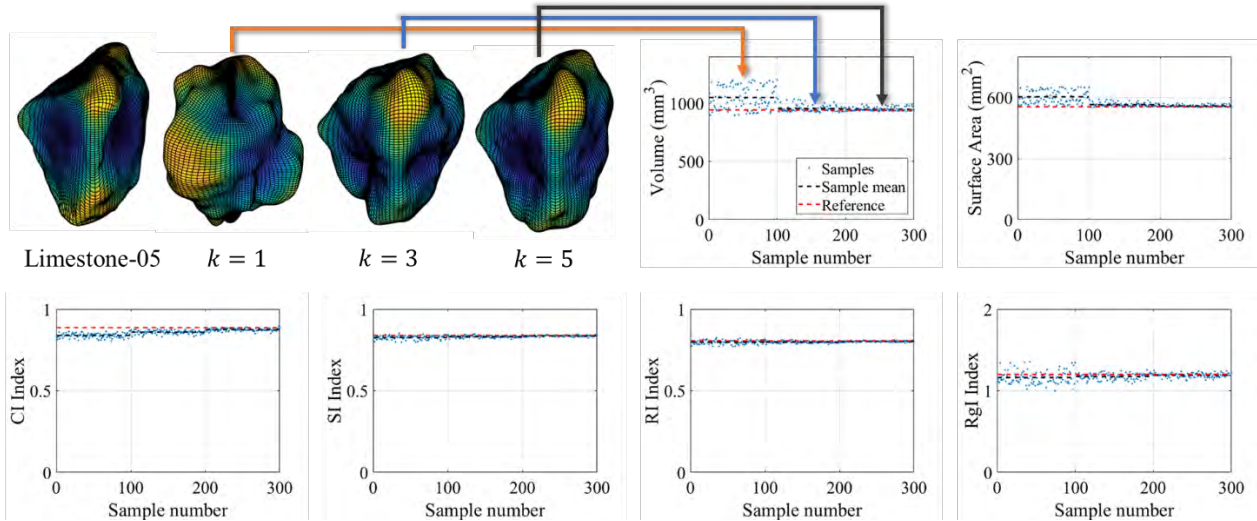


Figure 36: Validation of morphological indices for phase angle control method. Three types of parameters are chosen, each type generated 100 aggregates.

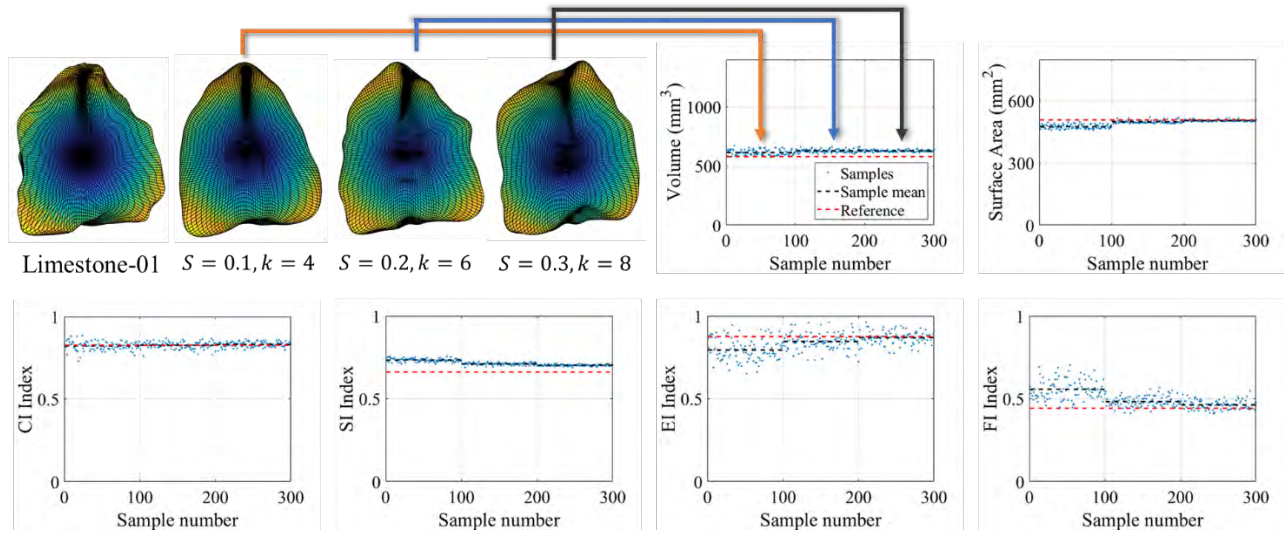


Figure 37: Validation of morphological indices for flatten aggregate. Three types of parameters are chosen, each type generates 100 aggregates.

4.4 Discrete element method (DEM) simulation

After successfully creating the desired digital representation of coarse aggregate particles, the challenge of efficiently positioning multiple aggregates within a specific container for mechanical simulations continues to be a significant issue in the field (Mollon and Zhao, 2014a; Qian et al., 2016). While simplified models using spheres or sphere-like bodies are common, the random morphology of aggregate particles often leads to unavoidable contact points at the corners, necessitating complex calculations to prevent overlaps.

To address this difficulty, gravity deposition is frequently employed. In this technique, a predetermined quantity of aggregates is set in a lattice with random orientation and placement, and then allowed to settle into a container by the force of gravity, or through compaction or expansion—though the latter process generally incurs higher costs and longer durations (Mollon and Zhao, 2014a). However, since this study aims to create standard, uniformly distributed cross-sections as references, merely filling a container with enough aggregates does not suffice.

To achieve an optimal aggregate distribution, this research utilized the Discrete Element Method (DEM) platform's PFC 3D software, employing a spatial compression approach coupled with porosity measurements. The physical collision properties defined in PFC3D ensure that no overlaps occur between the aggregates, and using porosity as a reference coefficient not only facilitates the creation of a convincing and ideal target model but also maintains its validity in 3D space.

Given that mortar was not modeled in this study, to mimic the effect of mortar spacing on aggregate particles, the mortar thickness was set at 0.04 in. Following optimal distribution, the equivalent sphere radius of all aggregates was decreased by 0.02 in to ensure a minimum spacing of 0.04 in between any two aggregates. The methodology can essentially be broken down into two phases: random aggregate generation and spatial compression.

4.4.1 Discrete aggregate generation and placement

Positioning discrete aggregates within a specified container is often challenging. Typically, aggregates are initially placed in a larger space and then compressed to achieve desired spatial dimensions and porosity levels. In PFC3D, aggregates are modeled using the logic of lumped superposition, where multiple spheres of varying sizes and positions are combined to represent a single "pebble" that mimics the morphology of the aggregate. This method also aids in calculating the contact behavior between aggregates.

The detail of the pebble model is primarily controlled by two parameters: the angle of intersection between the spheres d and the ratio of the smallest to the largest sphere r , where d ranges from 0 to 180 degrees and r from 0 to 1. **Figure 38** illustrates the pebble morphology generated by the "Pebble Packing" algorithm and its comparison to the reference aggregate Limestone-05. Increasing d enhances the model's capacity to simulate meso-scale details, while decreasing r improves the representation of fine-scale details. However, higher levels of fineness require a greater number of spheres to accurately model the aggregate's shape.

To maintain a balance between model detail and computational efficiency, this study sets ($d = 140$) degrees and ($r = 0.1$). For a concrete sample measuring 6 x 6 x 6 in, typically 2,000-3,000 aggregates of various sizes are needed based on the mix ratios employed.

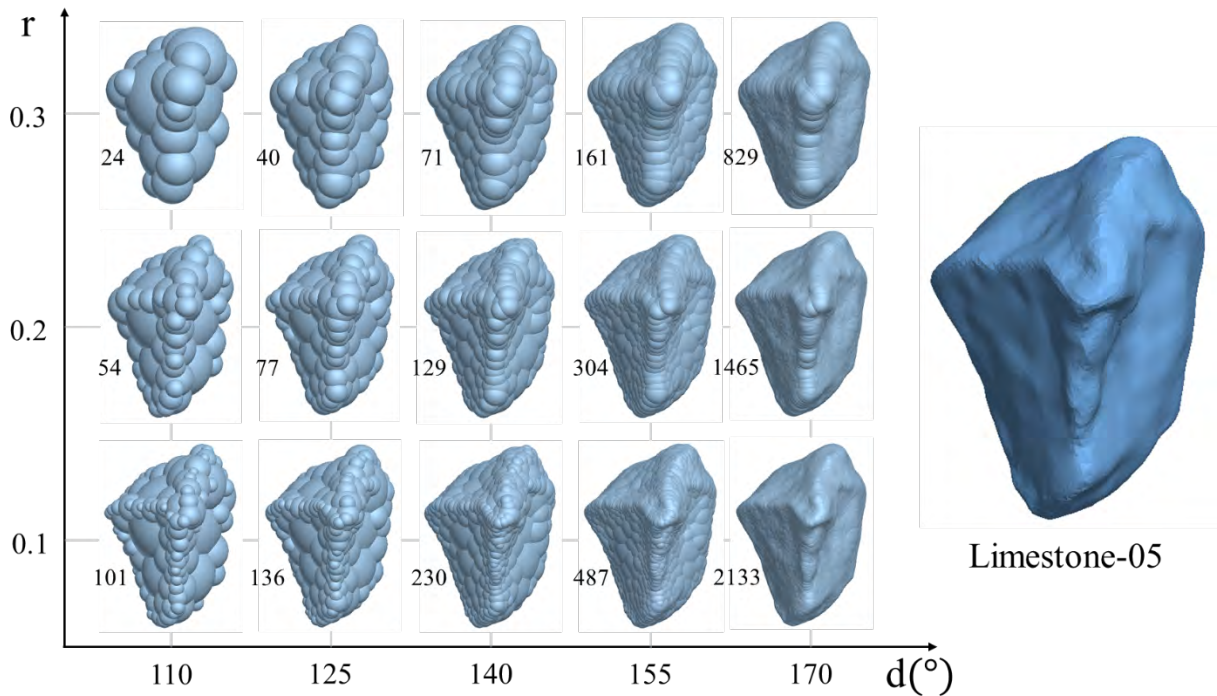


Figure 38: Morphological development of pebble models under different parameters.

After obtaining detailed aggregate morphology, reproducing the real aggregate content necessitates generating aggregates in amounts that correspond to the aggregate grading curve, as illustrated in **Figure 39**. The aggregate grading curve is derived using the sieve method, which classifies aggregates based on whether their length and width pass through a specific sieve mesh size. In this study, the equivalent sphere diameter defined in PFC is used to scale the size of the aggregates to fit within the specified intervals.

Aggregate quantities are determined based on volume, and the desired volume content for each size interval is achieved by summing the volumes of all generated aggregates. Due to the inherent randomness in aggregate morphology and size, which leads to variations in volume, the amount of aggregate produced varies with each batch. Moreover, given that this study presumes a minimum spacing of 0.04 in between aggregates due to mortar, the radius of each aggregate is increased by 0.02 in, significantly increasing the overall volume of aggregates.

Consequently, it is necessary to adjust the target porosity and aggregate content for each sieve interval. The adjusted aggregate volume V can be recalculated using **Equation 17**, where V_{ratio} is the percentage of volume adjustment based on the radius variation, and r is the average radius for the aggregate size interval.

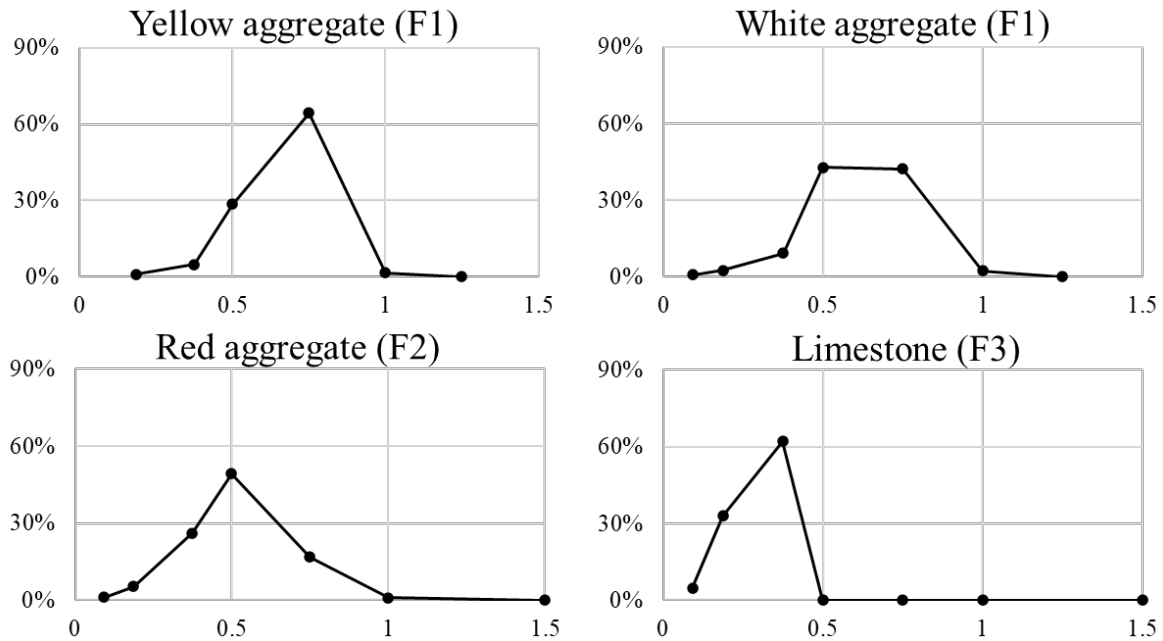


Figure 39: The gradation of aggregate by class.

$$V_{ratio} = \frac{V'}{V} = \frac{\frac{4\pi(r+\frac{1}{2})^3}{3}}{\frac{4\pi r^3}{3}} = 1 + \frac{\frac{3}{2}r^2 + \frac{3}{4}r + \frac{1}{8}}{r^3}$$

$$r = \frac{Upper\ size\ limit + Lower\ size\ limit}{2} \quad (17)$$

4.4.2 Optimal spatial distribution of aggregate

To simulate the optimal spatial distribution of aggregates, it is essential first to model the desired aggregate particles and then determine their optimal spatial distribution using the Monte Carlo method (Rubinstein and Kroese, 2016). According to this approach, the most uniform distribution is achievable by randomly placing a certain quantity of aggregate in a predefined space and averaging the results after multiple iterations. The pseudocode for this simulation is presented in **Algorithm 1**. Initially, individual aggregates are generated based on their specified size and randomly positioned within a cubic space of 7.9 x 7.9 x 7.9 in, with randomized rotations around the three coordinate axes. Each aggregate is placed 2,000 times, and the total volume for that aggregate is recorded upon successful placement until the aggregate volume for that interval is reached. Next, the porosity CP_1 of the sphere centered at the origin with a radius of 2.95 in is calculated, checking whether the difference between CP_1 and the target porosity is within a predefined tolerance. If not, a velocity directed towards the spatial origin is applied to each aggregate, scaled by a velocity coefficient k . After running for the predetermined time T seconds, the new porosity CP_2 is calculated. The process evaluates whether CP_2 is closer to the target porosity TP_1 than CP_1 ; if not, the velocity of the aggregates is halved, and the process is repeated until CP_2 is less than CP_1 . This iterative method ensures that the final cubic model M_1 achieves the desired porosity and, therefore, the desired 3D spatial distribution.

As depicted in **Figure 40**, the initial aggregate distribution is purely random, and the velocity of the aggregate particles is linearly related to their Euclidean distance from the origin. A total number of 10 optimal models, and 14 cross-sections for each model will be collected at equal intervals (0.4 in), providing a total of 140 cross-sections as references for the optimal distribution.

Algorithm 1 Optimal spatial distribution simulation

```
for All aggregate class and size interval do
  Get target volume for current size interval  $V_{total}$ ;
  Set current total volume  $V'_{total} = 0$ ;
  while  $V'_{total} < V_{total}$  do
    Generate one aggregate with aggregate database;
    Random place and rotate aggregate on 3-axis;
    Calculate current total volume  $V'_{total}$ ;
  end while
end for
```

```
Set target porosity as  $TP$ ;
Calculate current porosity  $CP1$ ;
while  $|CP1 - TP| > 0.01$  do
  Get velocity direction of each aggregate as  $[-x_i, -y_i, -z_i]$ ;
  Save current model as  $M1$ ;
  Set velocity scale factor  $k = \frac{s_1}{1 - |CP1 - TP|}$ ;
  Set velocity of each aggregate as  $k[-x_i, -y_i, -z_i]$ ;
  Run model for  $T$  seconds;
  Set velocity of all aggregate as  $[0, 0, 0]$ ;
  Calculate current porosity  $CP2$ ;
```

```
  Set  $s_2 = s_1$ ;
  while  $|CP2 - TP| > |CP1 - TP|$  do
    Reload  $M1$  and set  $s_2 = s_2/2$ ;
    Set velocity scale factor  $k = \frac{s_2}{1 - |CP1 - TP|}$ ;
    Set velocity of each aggregate as  $k[-x_i, -y_i, -z_i]$ ;
    Run model for  $T$  seconds;
    Set velocity of all aggregate as  $[0, 0, 0]$ ;
    Calculate current porosity  $CP2$ ;
```

```
  end while
  Set  $CP1 = CP2$ ;
  Save current model as  $M1$ ;
```

```
end while
```

```
Return  $M1, CP2$ ;
```

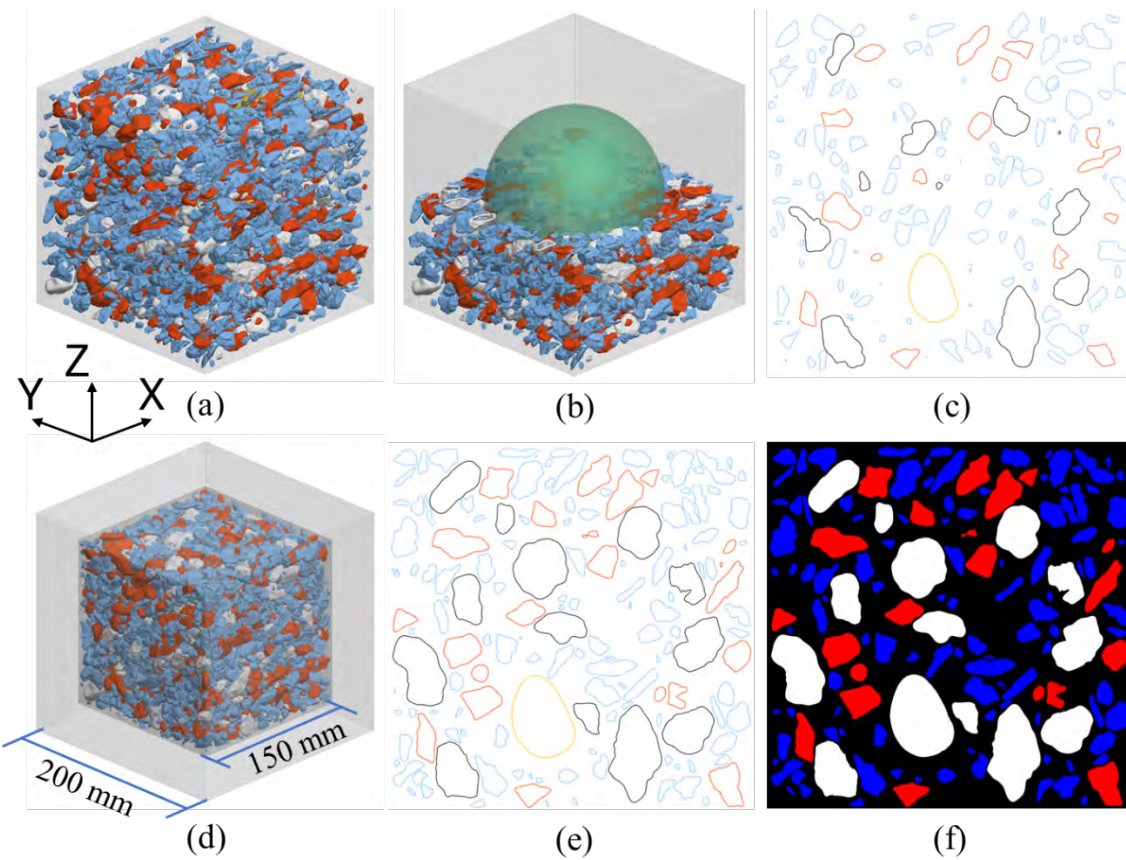


Figure 40: Optimal spatial distribution of aggregate, (a) aggregate generation and random placement, (b) porosity measure (0.746), (c) cross section image, (d) spatial coordinate shrinking (0.469), (e) cross section after shrinking, (f) image processing.

4.5 Consolidation Analysis

In this section, the analytical methodology discussed in the previous will be applied to compare and assess the experimental data gathered with the numerical simulation presented in **Section 4.4**. This analysis aims to elucidate the relationship between the vibratory input and the consolidation quality of the obtained concrete.

4.5.1 Results of DEM simulation

Ten sets of DEM simulations, as outlined in **Section 5**, were conducted, and are displayed in **Figure 41**. Each simulation achieves the target porosity, representing an ideal distribution pattern. However, there are variations in the individual assessment metrics across simulations, as the method does not uniformly maintain homogeneity at every localized spot. To mitigate the influence of outliers in this analysis, the interquartile ranges (10%, 90%) and the median values of the assessment metrics were plotted to refine the findings, as illustrated in **Figure 42**.

It is important to note that during the image segmentation of the actual concrete cross-sections, only coarse aggregates were differentiated. Any aggregate smaller than material passing the No. 8 sieve (< 0.094 in) was classified as fine aggregate and was considered to be a part of the mortar paste and therefore excluded from subsequent analysis. The same criteria were applied to the image processing tasks within the DEM analytical model to maintain consistency in the analyses.

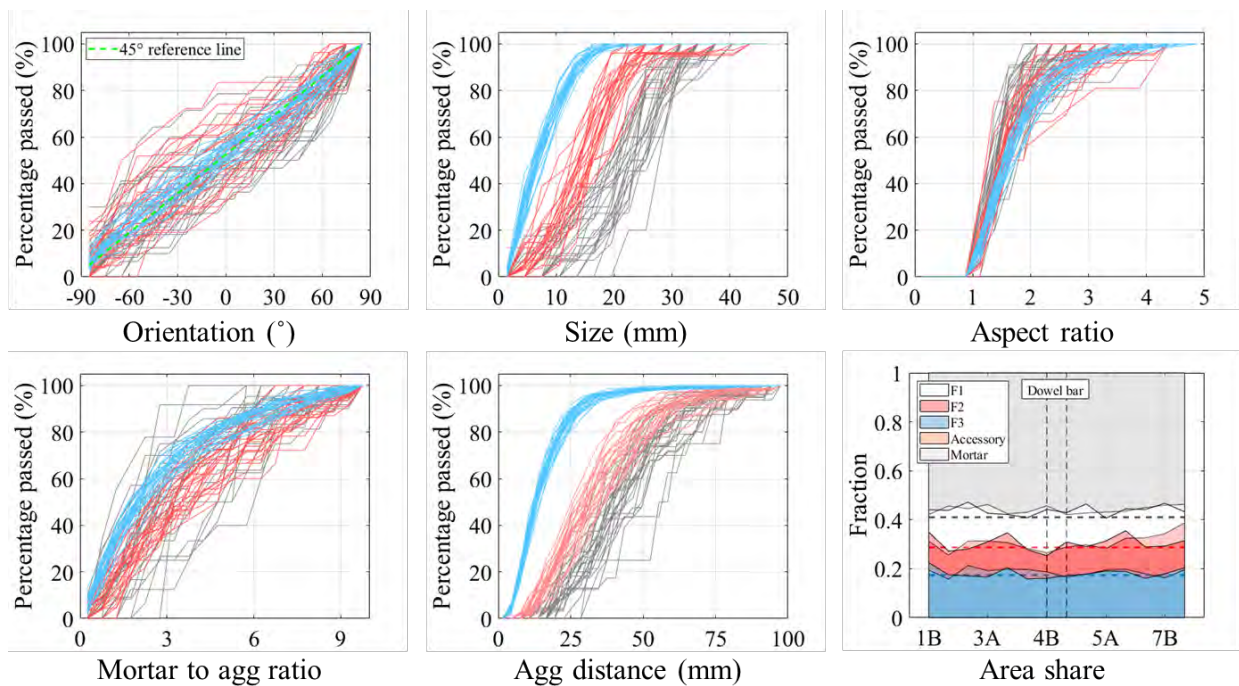


Figure 41: Results of DEM simulation (25.4 mm = 1 in).

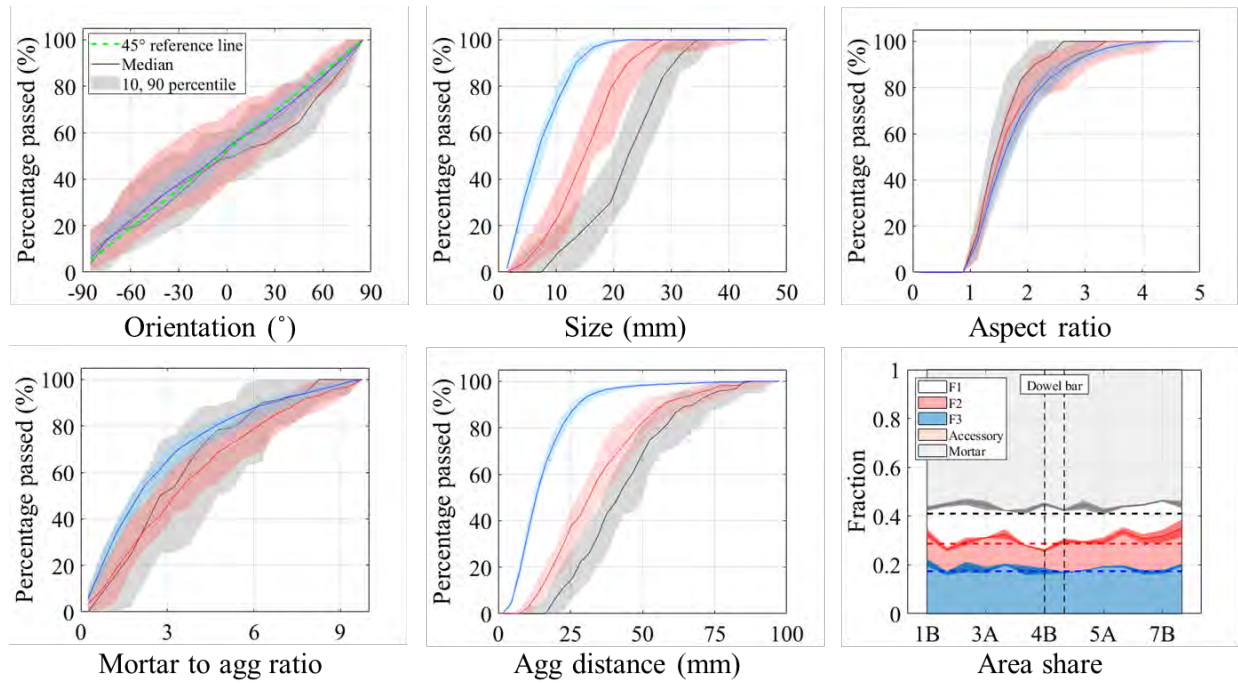


Figure 42: Data refinement of DEM simulation.

4.5.2 Aggregate properties analysis

Aggregate properties were examined to assess if aggregate gradation is influenced by vibration duration and the correlation with depth. The findings from both experiments and simulations regarding aggregate properties are depicted in **Figure 43**. The DEM model successfully replicated aggregate morphology and gradation, showing a strong correlation with actual concrete experiments, and thereby confirming the reproducibility of the proposed method.

Vibration duration did not significantly impact the orientation, size, or aspect ratio of the aggregates; however, notable fluctuations were observed in the F1 and F2 aggregates based on the specific relative volume content (see **Figure 42**). Additionally, no correlation was found between the depth of aggregate and its properties. The aspect ratio and roundness of aggregates increase with gradation, consistent with observations from **Section 4.2**.

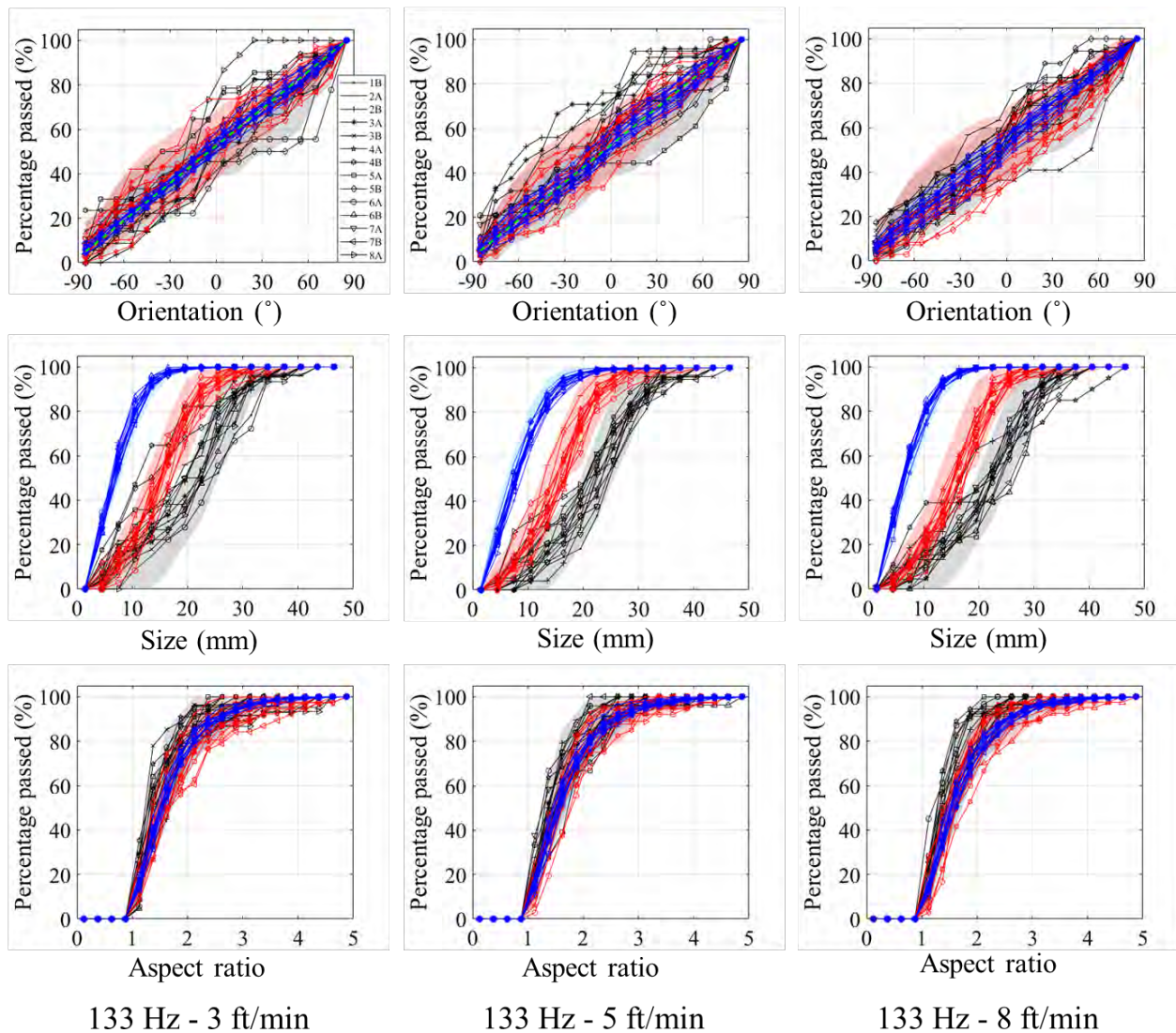


Figure 43: Aggregate properties of the experiments and DEM simulation.

4.5.3 Aggregate homogeneity analysis

Figure 44 presents statistics related to the volumetric portion of aggregates along the depth. Specifically, the orange area (accessory) denotes the area of the dowel bar and basket included in the PaCS simulations, calculated by multiplying the area of these elements by the corresponding volume fraction (0.409). The area share of the F3 aggregate remains stable and aligns with analytical data, while the F1 aggregate shows significant variability and is substantially influenced by accessories (Plane 4B and 5B). There is a notable decrease in large-sized aggregate (F1) content with depth, suggesting that accessories like baskets and dowel bars predominantly affect the distribution of larger aggregates.

Incorporating findings from **Figure 44(d-e)**, prolonged vibration results in increased content of mortar and smaller aggregates (F3) at the bottom of the specimen, with a corresponding decrease in large aggregate content. This outcome is expected as vibration typically expels trapped air, allowing the mortar to become more fluid and occupy spaces formerly filled with air. Additionally, vibration caused a disturbance in the standard deviation (SD) of large-sized aggregates, while its effect on the F3 aggregate was minimal for the paver speeds considered. According to the DEM analysis, the aggregate distribution at 133 Hz - 5 ft/min proved to be optimal. In contrast, the coarse aggregate at 133 Hz - 3 ft/min was insufficient, and the F1 aggregate at 133 Hz - 8 ft/min did not display the expected standard deviation, i.e., the lower portion of the specimen contained a greater-than-optimal F1 aggregate content.

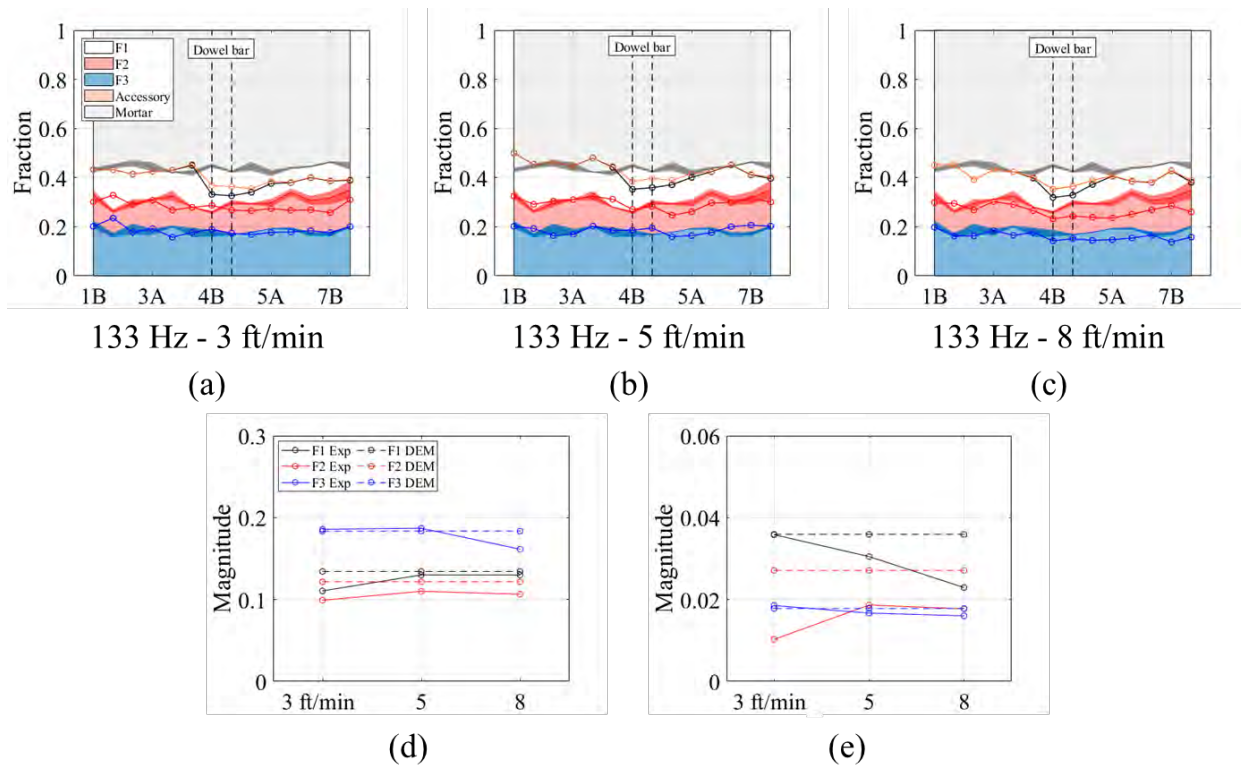


Figure 44: Homogeneity analysis of the three experiments, (a-c) are the area share, (d) mean of the area share, (e) standard deviation of the area share.

4.5.4 Aggregate dispersion analysis

Dispersion analysis is utilized to evaluate the stability of aggregate distribution across different layers based on MTAR and DTSL, serving as key indicators of aggregate homogeneity over the depth of the pavement. **Figure 45 (a-c)** reports the statistical

outcomes for MTAR, where the experimental data align closely with the analytical predictions, with both F1 and F3 aggregates exhibiting good volatility. Analysis from **Figures 45 (d-e)** indicates that vibration impacts the spatial distribution of aggregates in a size-dependent manner. Increased vibration duration results in greater dispersion of large-sized aggregates (F1), enhancing the mortar content around them while stabilizing the mortar content around smaller aggregates (F3). Vertically, the upper layers of F1 aggregates are less influenced by vibration duration compared to the lower layers, whereas the F3 aggregates demonstrate minimal variance across the depth.

The results further reveal that in the 133 Hz - 3 ft/min experiment, the mortar content and standard deviation around the F1 aggregates significantly diverged from the reference values, suggesting excessive vibration. Although the 133 Hz - 8 ft/min experiment aligned most closely with the analytical results, it showed higher mortar content around the F3 aggregates, indicative of insufficient vibration. It is important to note that fluctuations in the experimental results are slightly more pronounced than those predicted analytically due to the influence of the dowel bar and baskets in the PaCS simulations.

Figure 46 presents the DTSL statistics, where the experimental sample size exceeded that of the analytical model, resulting in slightly larger average spacings for F1 and F2 aggregates. Consistent with MTAR findings, increased vibration duration markedly raises the average spacing and dispersion of larger aggregates while the dispersion of smaller aggregates tends to stabilize for the paver speeds considered.

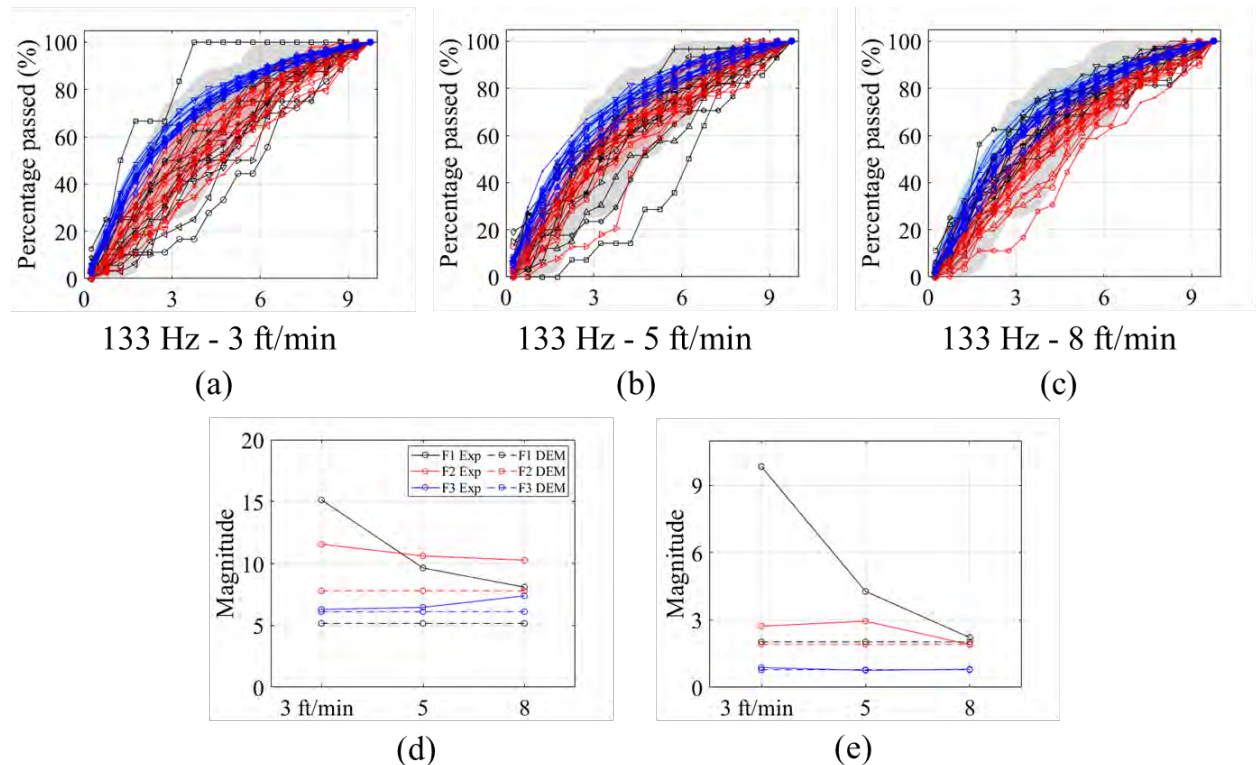


Figure 45: The MTAR of the three experiments, (a-c) are the MTAR of the three experiments

and analytical models, (d) mean of the MTAR, (e) standard deviation of the MTAR.

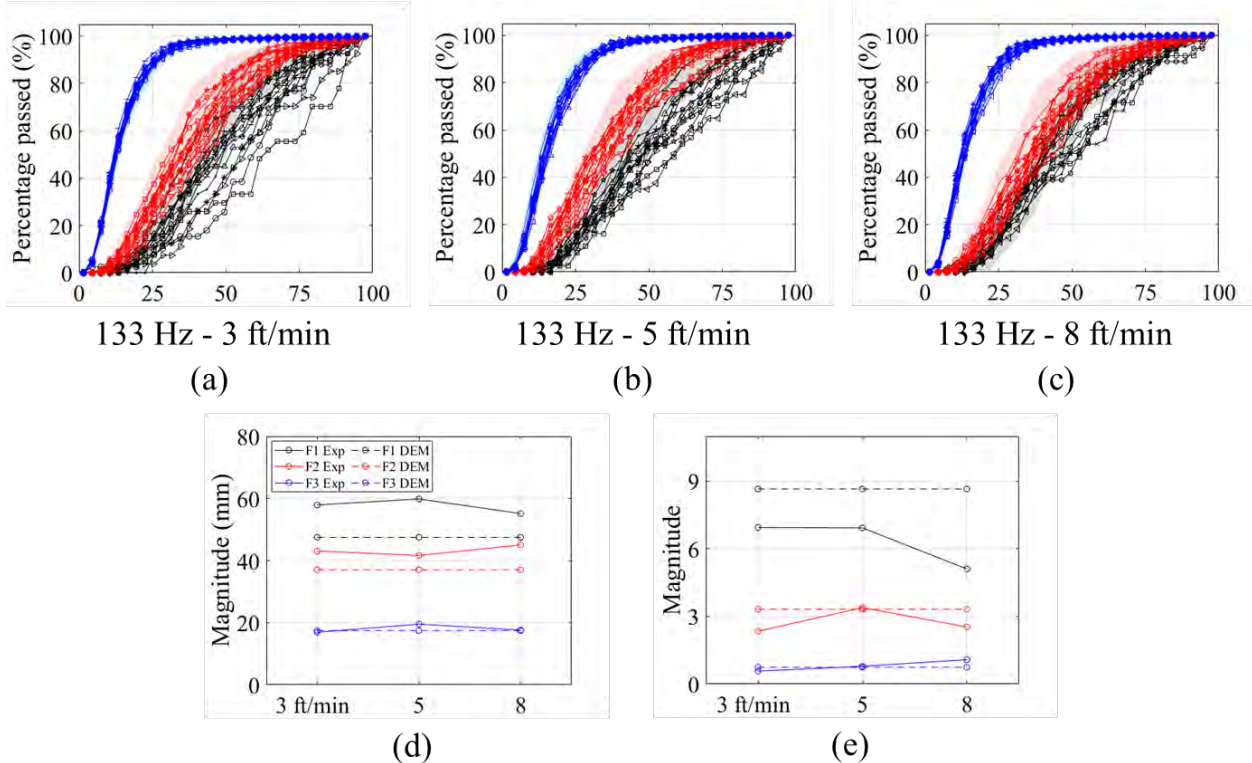


Figure 46: The DTSL of the three experiments, (a-c) are the DTSL of the three experiments and analytical models, (d) mean of the DTSL, (e) standard deviation of the DTSL.

4.5.5 Aggregate 3D spatial distribution analysis

Figure 47 illustrates the aggregate center of gravity distribution across three perspectives, fitted with ellipses using the least squares method based on analytical data. Each set of experiments shows varied dispersion levels, with F1 aggregates consistently displaying the most eccentricity. The 133 Hz - 3 ft/min experiment shows notable eccentricity in both the upper and middle sections of the F1 aggregate, while the F3 aggregate exhibits almost no eccentricity. A slight eccentricity is observed for all three aggregate types at 133 Hz - 5 ft/min, whereas significant fluctuations in the X direction occur for the F1 aggregate in the 133 Hz - 8 ft/min experiment. Given the presence of dowel bars, this suggests that the central F1 aggregates were displaced across all three experiments.

The experimental accessories primarily impacted the distribution of large-sized aggregates without significantly affecting the numerous smaller-sized aggregates. No direct influence of vibration duration on the center of gravity distribution was observed, likely because vibration randomly disperses large-sized aggregates but maintains overall stability in the center of gravity, as no directional bias was introduced. Notably, the primary

eccentricity of the aggregates occurred in the X direction, possibly influenced by the vibration direction of the vibrator shaft, suggesting a potential area for further investigation (Chen et al., 2020; Yan et al., 2022).

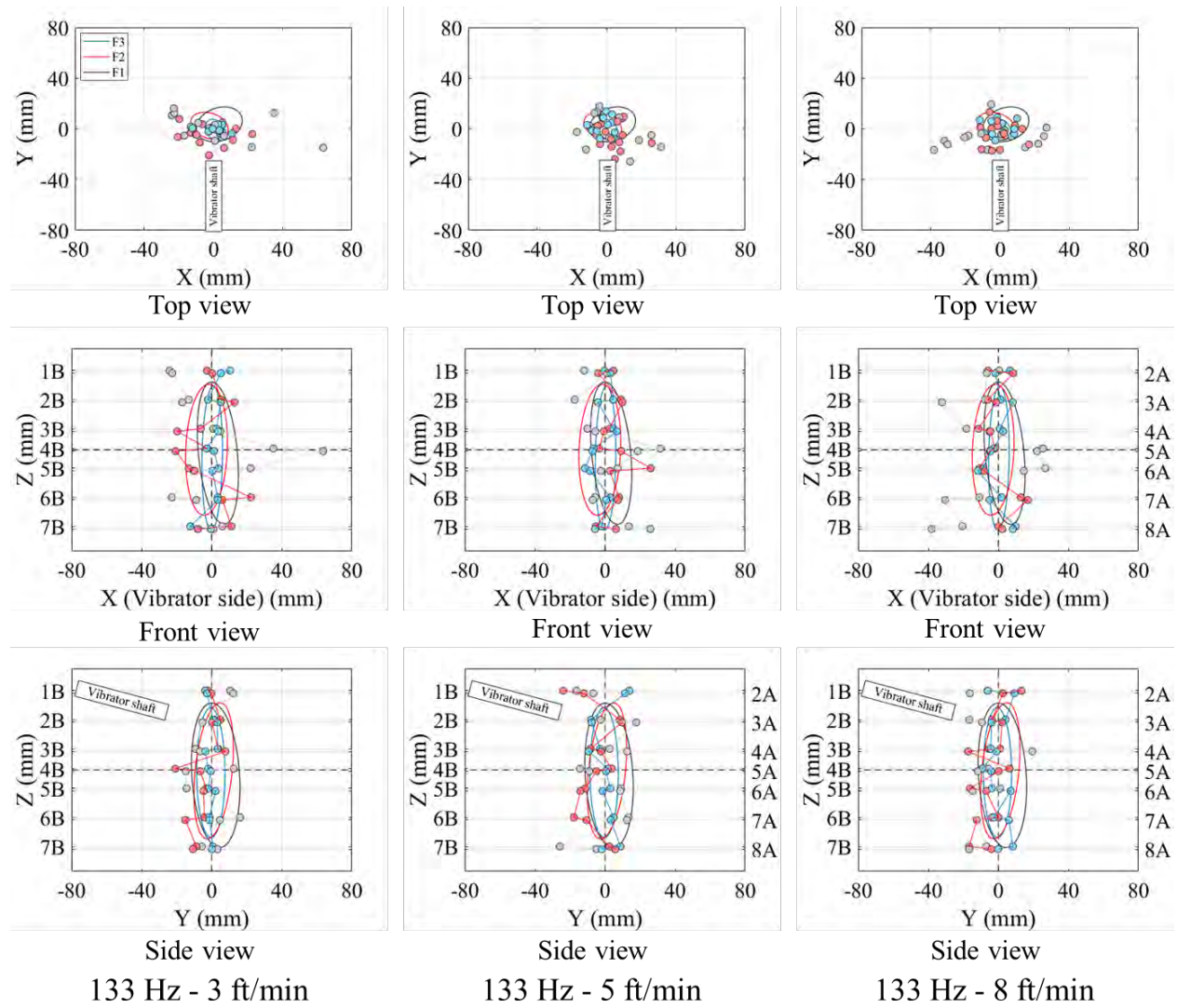


Figure 47: Center of gravity analysis of the three experiments.

5. Discussion

5.1 PaCS Implementation

The PaCS has been shown to effectively replicate the paving conditions and can be used to evaluate the effect of mixture design and vibration energy on consolidation. The next step in this study is to perform the PaCS to replicate the range of parameters depicted in **Table 9**. Preliminary simulations have been performed using the control mixture design with a target slump of 1.5 in and varying paver speed and vibrator frequency. The purpose of these preliminary simulations is to determine if the analysis methods previously described can capture the effect of varying vibration energy. The following three simulations were performed (see **Figure 48**): Specimen A with 8 ft/min paving speed and 83 Hz vibrator frequency, Specimen B with 5 ft/min paving speed and 83 Hz vibrator frequency, Specimen C with 5 ft/min paving speed and 133 Hz vibrator frequency.

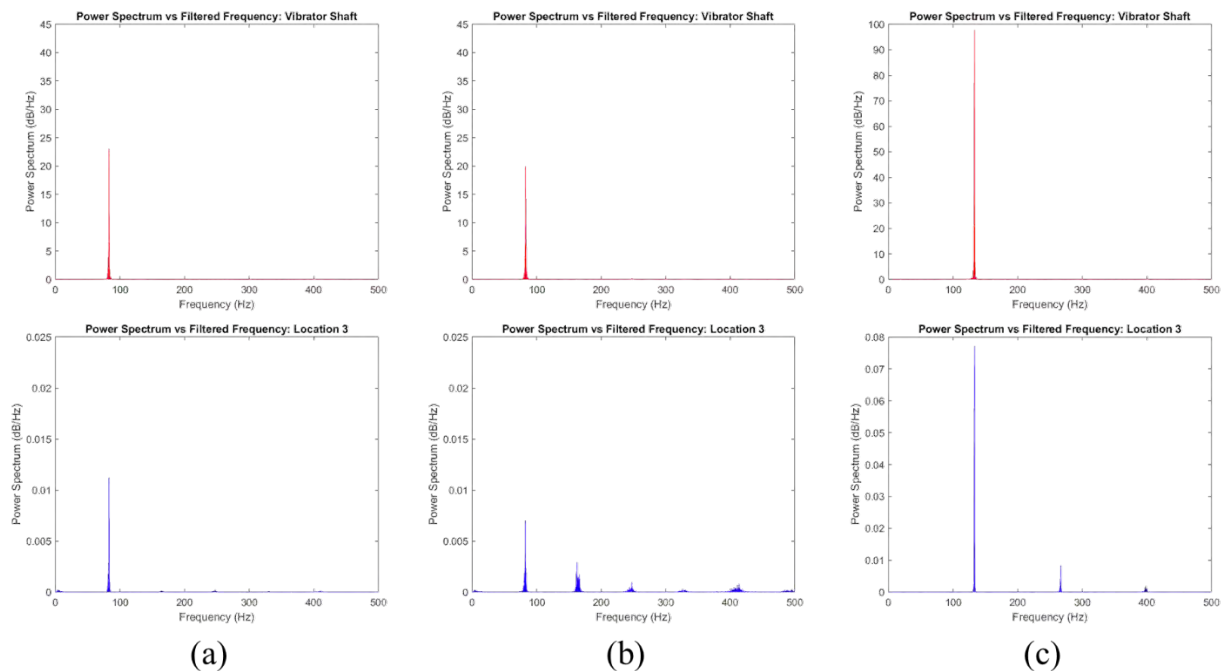


Figure 48. The magnitude of the power spectrum, (a) 83 Hz - 8 ft/min, (a) 83 Hz - 5 ft/min, (a) 133 Hz - 5 ft/min.

First, the data collected by the accelerometers was used to quantify the total vibration energy applied for each simulation. As shown in **Figure 48**, the magnitude of the power spectrum peak was approximately 100 dB/Hz for Specimen C compared to 25 and 20 dB/Hz for Specimens A and B, respectively. The significantly higher vibration energy in Specimen C is attributed to the higher vibrator frequency used. However, paver

speed has minimal effect on total vibration energy, as there was minimal difference between peak power spectrum results for Specimens A and B.

Figure 48 reports the power spectrum plot comparisons at: (1) the vibrator shaft and (2) location 3 for specimens with control concrete mixture and (a) paving speed 8 ft/min and vibrator frequency 83 Hz, (b) paving speed 5 ft/min and vibrator frequency 83 Hz, and (c) paving speed 5 ft/min and vibrator frequency 133 Hz.

Future work will expand on the PaCS procedure established in this study to enable further characterization of concrete consolidation. First, air void system analyses described in (ASTM C457M-23, 2023) will be incorporated into the workflow. An image analysis of the entrained air in each specimen will be used to determine the uniformity and distribution of the air void system as a function of the vibration energy for each simulation. An example of a specimen prepared for this procedure is shown in **Figure 49**. The entrained air highlighted in white will be analyzed in a manner similar to the aggregate reconstruction to determine the uniformity of the entrained air distribution within the specimen.

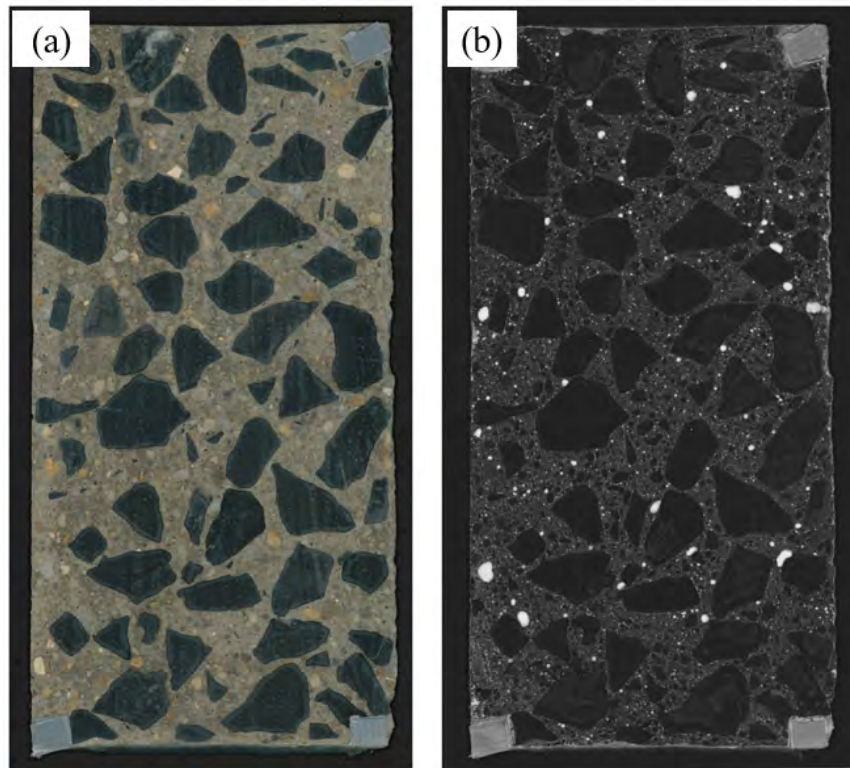


Figure 49. Example of a concrete specimen, (a) prior and (b) after air void detection.

The 2D air void system reconstructions will be coupled with the 2D aggregate reconstructions to develop a 3D model of the aggregate and air content arrangements from each specimen. The model will provide a complete visual and statistical representation of the consolidation that will be used to evaluate the effect of vibrator frequency, paver speed, and concrete workability. The results of this will be presented in

the future. The development of the PaCS along with these analysis techniques provides a unique opportunity to evaluate the amount of vibration energy, in terms of vibrator frequency and paver speed, needed for a project based on the workability of the concrete mixture. Results from the established test methods, such as the V-Kelly Test can be used to characterize the workability of the concrete mixture that will be used on the project. The paver speed is often dictated by the rate of concrete production, but the paving contractor can adjust vibrator frequency during paving to ensure proper concrete consolidation based on the workability of the concrete and the speed of the paver.

5.2 Effect of vibration on spatial distribution of aggregates

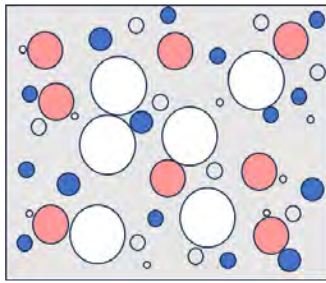
From the analysis, it is observed that the duration of vibration and the location of aggregates do not significantly correlate with the properties of the aggregates, yet the real aggregate properties and their spatial distribution are accurately replicated using spherical harmonic functions and a multiscale control algorithm.

Regarding the uniform distribution of aggregates, the duration of vibration displays a distinct relationship with both aggregate size and depth within the specimen. Specifically, increased vibration time reduces the presence of large-sized aggregates (F1) at the bottom of the specimen while augmenting the quantity of small-sized aggregates (F3) at the same location. The impact on medium-sized aggregates (F2) is minimal, yet there is a notable increase in the variability of large-sized aggregates.

Similarly, extended vibration duration increases the mortar content around large-sized aggregates, widens the spacing between aggregates, and notably enhances the variability of the F1 aggregates, adversely impacting the mechanical properties of the concrete. This observation aligns with findings from other researchers (Chai et al., 2023; Chen et al., 2020) and is indicative of the so-called Brazil nut effect (Granular convection) (Olsson et al., 2019; Breu et al., 2003). This phenomenon is influenced by three main mechanisms: inertia, convection, and buoyancy (Huerta and Ruiz-Suárez, 2004). The predominance of these mechanisms is determined by the density of the particles. When a particle's density exceeds that of the surrounding medium, it settles due to vibration; conversely, if its density is equal to or less than that of the surrounding medium, it rises due to convection, with larger particles typically experiencing more pronounced effects (Makoto et al., 1984). This explains the differing observations of aggregate movement by various research groups (Chai et al., 2023; Chen et al., 2020), suggesting that changes in vibration conditions should carefully consider their impact on the distribution of large-sized aggregates.

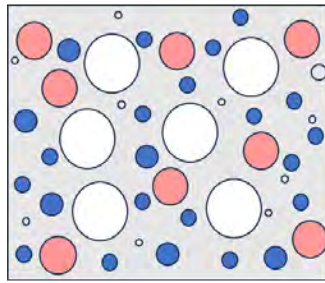
In contrast, the distribution of the center of gravity of aggregates shows no significant correlation with vibration duration. However, the center of gravity for F1 aggregates is significantly influenced by the experimental setup. The analysis reveals that although vibration leads to significant dispersion of the F1 aggregate and a decrease in aggregate content at the bottom, these occurrences tend to be random. Therefore, special attention should be paid to the final aggregate distribution around the baskets and dowels. While coarser aggregate showed tendencies to move in the same direction as the vibrator shaft, further investigation is required to confirm this. Summarizing these findings, a synthetic description of the main findings is reported in **Figure 50**.

Mortar
 Large aggregate
 Middle aggregate
 Small aggregate
 Entrapped air voids
 Entrained air voids



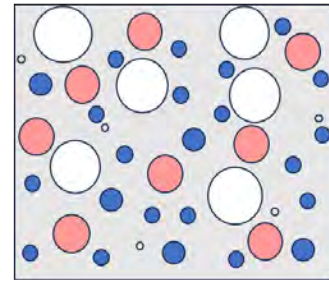
Under consolidation

1. Large entrapped air
2. Granular arches
3. More average mortar around small aggregate



Good consolidation

1. Entrapped air released
2. Granular arches broken
3. Amount of small aggregate increase
4. Average mortar around small aggregate decreases, with an increase in large aggregate
5. Variation of middle aggregate slightly increase



Over consolidation

1. Entrained air released
2. Large aggregate lift-up
3. Average mortar around large aggregate and variation increases significantly
4. Amount of middle aggregate is decreased, with a slight improvement in stability
5. Insignificant change in small aggregate distribution, and even a better stability

Figure 50: Three types of concrete consolidation.

6. Conclusions

In this study, a systematic and comprehensive research framework was proposed to incorporate innovative experimental designs, computer vision-based data acquisition, concrete consolidation quality assessments, multiscale modeling with spherical harmonic expansions and random fields, and numerical simulation of optimal spatial distributions. This framework aims at exploring the relationship between the duration of vibration and the spatial distribution of coarse aggregates in concrete during slipform paving. Examples demonstrate that this framework offers a flexible and efficient approach to simulating the mechanical behavior of slipform paving, streamlines image segmentation and extraction using a pre-trained CNN model, rapidly generates a given number of high-fidelity aggregate particles through digital representations and multiscale reconstruction, and provides a basis for assessing concrete consolidation quality through a DEM-based optimization algorithm. The main conclusions of this study are:

(1) The PaCS simulation effectively replicates the real paving process. Considerations such as vibration angle, vibrator movement mode, dowel bars and baskets, vibration duration, and frequency have allowed for a more versatile and thorough evaluation of concrete consolidation quality.

(2) Image segmentation and extraction techniques utilizing pre-trained CNN models simplify the image processing steps, reducing the complexity of image-based concrete consolidation analysis. Additionally, slicing along the depth direction enhances the program's ability to interpret the 3D spatial distribution of aggregates from 2D images.

(3) The ability to accurately characterize aggregate morphology using spherical harmonic expansions, coupled with the rapid generation of numerous "virtual aggregates" that are statistically similar to the real aggregate particles, by means of multi-scale control and random fields. Laser scanning simplifies acquiring morphological characteristics of aggregates and avoids the biases introduced by Gaussian and Brownian random fields in capturing raw aggregate geometry. Oscillation effects encountered when generating flat and elongated aggregates are mitigated by down-sampling and up-sampling methods.

(4) Utilizing realistic digital representations of aggregate particles, Monte Carlo simulations and optimal spatial distribution algorithms can help achieve an idealized optimal spatial distribution of aggregates. This method serves as a practical guide for field construction to enhance the quality of concrete consolidation and to assess the aggregate distribution quality in actual concrete samples.

(5) In line with previous research, the vibration process for concrete can be summarized as follows: initially, concrete quickly liquefies, eliminating large air pockets and allowing mortar and small-sized aggregates to fill the resulting gaps. As vibration continues, small air bubbles are gradually released, large-sized aggregate spacing increases, granular arches break down, and the content of mortar and small-sized aggregates at the bottom of the specimen slightly increases, leading to the most homogeneous aggregate distribution and optimal mechanical properties of the concrete. With further vibration, entrained air begins to release, causing large-size aggregates to

move and segregate, though the stability of small-size aggregates improves. The content of large-size aggregates at the bottom decreases (affected by convection uplift), average spacing increases, stability along the depth reduces, and mechanical properties start to decline. Increasing vibration frequency exacerbates segregation and reduces the time required for it to occur, affecting large-size aggregates more significantly than small-size aggregates without causing shifts in the aggregate center of gravity.

Furthermore, it is important to acknowledge that the findings of this study are based on the outlined laboratory investigation framework, and several potential factors require follow-up studies to enhance the research:

(1) The design of the experimental setup did not explore the effect of vibrator shaft spacing, nor the potential variations induced by different geometrical features of the pavement cross-section (e.g., edge effects at the pavements) and further verification is needed to determine if vibration waves might overlap in transmission or be reflected in the experimental setup.

(2) The slump of the three test groups varied significantly, potentially affecting the fluidity of the mortar after concrete liquefaction. Further investigations on concrete slump and air content are necessary.

(3) The absence of field tests means that environmental variations in test settings could potentially affect the consolidation quality of concrete.

References

- ACI Committee 305. (1991, July-August). Hot Weather Concreting ACI 305R-91. ACI Materials Journal, 417-436.
- Ahmadi, B. (2000, October). Initial and final setting time of concrete in hot weather. Materials and Structures, 33, 511-514.
- American Concrete Pavement Association. (1996). Construction of Portland Cement Concrete Pavements. Washington D.C.: Federal Highway Administration.
- ASTM International. (1978). ASTM C143-78 Standard Test Method for Slump Of Portland Cement Concrete. West Conshohocken, PA: American Society for Testing and Materials.
- ASTM International. (2017). ASTM C685M-17 Standard Specification for Concrete Made by Volumetric Batching and Continuous Mixing. West Conshohocken, PA: American Society for Testing and Materials.
- ASTM International. (2022). ASTM C231M-22 Standard Test Method for Air Content of Freshly Mixed Concrete by the Pressure Method. West Conshohocken, PA: American Society for Testing and Materials.
- ASTM International, A. (2020). Standard test method for slump of hydraulic-cement concrete. Standard, ASTM International, West Conshohocken, PA. 1, 2
- ASTM International, A. (2022). Standard test method for air content of freshly mixed concrete by the pressure method. Standard, ASTM International, West Conshohocken, PA. 2
- Baddeley, A. and Jensen, E. B. V. (2004). Stereology for statisticians. CRC Press.3.1
- Brisard, S., Serdar, M., and Monteiro, P. J. (2020). Multiscale x-ray tomography of cementitious materials: A review. Cement and Concrete Research, 128:105824. 3.2
- Bilgil, A., Ozturk, B., & Bilgil, H. (2005). A numerical approach to determine viscosity-dependent segregation in fresh concrete. Applied Mathematics and Computation, 162(1), 225-241.
- Bower, L., & Gerhardt, B. (1971). The Effect of Good Vibration on The Durability of Concrete Pavement. Colorado Department of Highways.
- Cable, J., McDaniel, L., & Steffes, R. (1999). Evaluation of Paver Frequency Monitoring and Concrete Consolidation. Iowa State University.
- Civil Today. (n.d.). Advantages and Limitations of Slump Test. Retrieved from civiltoday.com: <https://civiltoday.com/civil-engineering-materials/concrete/80-advantages-and-limitations-disadvantages-of-slump-test>
- Colorado DOT. (2019, September 11). The Box Test in Slip Form Paving of Fresh Concrete. Colorado Department of Transportation.
- Chai, M., Hu, C., and Cheng, M. (2023). Study on the effect of vibrating process on the compactness of slipform concrete. Applied Sciences, 13(14):8421. 1, 2, 3.1, 6.6, 7
- Chen, F., Jelagin, D., and Partl, M. N. (2020). Vibration-induced aggregate segregation

- in asphalt mixtures. *Materials and Structures*, 53:1–14. 6.5, 6.6
- Clayton, C., Abbireddy, C., and Schiebel, R. (2009). A method of estimating the form of coarse particulates. *Geotechnique*, 59(6):493–501. 4.5
- Comby-Peyrot, I., Bernard, F., Bouchard, P.-O., Bay, F., and Garcia-Diaz, E. (2009). Development and validation of a 3d computational tool to describe concrete behavior at mesoscale. application to the alkali-silica reaction. *Computational Materials Science*, 46(4):1163–1177. 4
- Cook, M. D., Ley, M. T., and Ghazeezadah, A. (2014). A workability test for slip formed concrete pavements. *Construction and Building Materials*, 68:376–383. 1, 2
- Elliott, R. (1974). Effect of internal vibration of portland cement concrete during paving. Technical report, Bureau of Materials and Research, Kansas Department of Transportation. 1, 6.4
- Erdogan, S. T. (2005). Determination of aggregate shape properties using X-ray tomographic methods and the effect of shape on concrete rheology. The University of Texas at Austin. 4
- Erdoğan, S. T., Forster, A. M., Stutzman, P. E., and Garboczi, E. (2017). Particle-based characterization of ottawa sand: Shape, size, mineralogy, and elastic moduli. *Cement and concrete composites*, 83:36–44. 4
- Federal Highway Administration. (1995). *Construction of Portland Cement Concrete Pavements*. American Concrete Pavement Association.
- Fantous, T. and Yahia, A. (2020). Air-void characteristics in highly flowable cement-based materials. *Construction and Building Materials*, 235:117454. 1
- FARO laser scan arm (2024). FARO Specification. 4.1
- (Fascetti et al., 2018) Fascetti, A., Bolander, J. E., and Nisticò, N. (2018). Lattice discrete particle modeling of concrete under compressive loading: Multiscale experimental approach for parameter determination. *Journal of Engineering Mechanics*, 144(8):04018058. 3.2.3, 4
- Fascetti, A., Ichimaru, S., and Bolander, J. E. (2022). Stochastic lattice discrete particle modeling of fracture in pervious concrete. *Computer-Aided Civil and Infrastructure Engineering*, 37(14):1788–1808. 3.2.3
- Fascetti, A. and Oskay, C. (2019). Dual random lattice modeling of backward erosion piping. *Computers and Geotechnics*, 105:265–276. 3.2.3
- Feng, J., Cen, S., Li, C., and Owen, D. (2016). Statistical reconstruction and karhunen-loève expansion for multiphase random media. *International Journal for Numerical Methods in Engineering*, 105(1):3–32. 4.2, 4.2
- Feng, J., Li, C., Cen, S., and Owen, D. (2014). Statistical reconstruction of two-phase random media. *Computers & Structures*, 137:78–92. 4.2, 4.2, 4.2, 4.2
- Garboczi, E. J. (2002). Three-dimensional mathematical analysis of particle shape using x-ray tomography and spherical harmonics: Application to aggregates used in concrete. *Cement and concrete research*, 32(10):1621–1638. 1, 4, 4.1, 4.2, 4.5
- Garboczi, E. J. and Bullard, J. W. (2004). Shape analysis of a reference cement. *Cement and concrete research*, 34(10):1933–1937. 4

- Glasby, T., Day, J., Genrich, R., and Aldred, J. (2015). Efc geopolymer concrete aircraft pavements at brisbane west wellcamp airport. *Concrete*, 2015:1–9. 1
- Grigoriu, M., Garboczi, E., and Kafali, C. (2006). Spherical harmonic-based random fields for aggregates used in concrete. *Powder Technology*, 166(3):123–138. 4, 4.2
- Guo, F.-q., Zhang, H., Yang, Z.-j., Huang, Y.-j., and Withers, P. J. (2023). A spherical harmonic-random field coupled method for efficient reconstruction of ct-image based 3d aggregates with controllable multiscale morphology. *Computer Methods in Applied Mechanics and Engineering*, 406:115901. 1, 4, 4.2, 4.2, 4.4, 5
- Grieb, W., & Marr, R. (n.d.). Use of the Kelly Ball for Field Measurement of Concrete Consistency. Highway PHysical Research Engineerings, Physical Research Branch. Bureau of Public Roads.
- Halliday, D., Resnick, R., & Walker, J. (2021). *Fundamentals of Physics, Extended*, 12th Edition. Hoboken, NJ: Wiley.
- Halliday, D., Resnick, R., & Walker, J. (2021). *Fundamentals of Physics, Extended*, 12th Edition. Hoboken, NJ: Wiley.
- Han, J., Wang, K., Wang, X., and Monteiro, P. J. (2016). 2d image analysis method for evaluating coarse aggregate characteristic and distribution in concrete. *Construction and Building Materials*, 127:30–42. 3.1, 3.2
- Hou, Z. Y., Yuan, Y. Z., Yuan, Z. G., Liang, Y. D., and Zhou, Z. H. (2014). Study on vibrational liquefaction behavior of air-entrained concrete. *Advanced Materials Research*, 857:20–26. 1
- Huerta, D. and Ruiz-Suárez, J. (2004). Vibration-induced granular segregation: a phenomenon driven by three mechanisms. *Physical Review Letters*, 92(11):114301. 6.6
- IDOT. (2015). *Standard Specifications for Bridge and Highway Construction*. Ames, IA: Iowa Department of Transportation.
- International, A. (n.d.).
- International, A. (2023). *ASTM C457M- 23 Standard Test Method for Microscopical Determination of Parameters of the Air-Void System in Hardened Concrete*. West Conshohocken, PA: American Society for Testing and Materials.
- Iowa DOT. (2008). *Measuring Paver Vibration Frequency*. Iowa Department of Transportation.
- Jaworski, P. (2022, May 19). (M. Darnell, Interviewer)
- Jaworski, P. (2017, November 30). *Vibrations Role Surface Decets-Concrete Surface Distresses Caused By Vibrator Speed*. American Concrete Pavement Association.
- Jaworski, P. (2017). *Vibrations Role Surface Defects-Concrete Surface Distresses Caused By Vibrator Speed*. American Concrete Pavement Association.
- Jaworski, P. (2022, May 30).
- Kirillov, A., Mintun, E., Ravi, N., Mao, H., Rolland, C., Gustafson, L., Xiao, T., Whitehead, S., Berg, A. C., Lo, W.-Y., et al. (2023). Segment anything. *arXiv preprint arXiv:2304.02643*. 3.1
- Ling, Y. and Taylor, P. (2021). Effect of controlled vibration dynamics on concrete

- mixtures. *ACI Materials Journal*, 118(5):161–172. 1, 7
- Liu, L., Shen, D., Chen, H., and Xu, W. (2014). Aggregate shape effect on the diffusivity of mortar: A 3d numerical investigation by random packing models of ellipsoidal particles and of convex polyhedral particles. *Computers & structures*, 144:40–51. 4
- Liu, X., Garboczi, E., Grigoriu, M., Lu, Y., and Erdoğ an, S. T. (2011). Spherical harmonic-based random fields based on real particle 3d data: improved numerical algorithm and quantitative comparison to real particles. *Powder Technology*, 207(1-3):78–86. 4.2
- Loz, P., Monticelli, J., Futai, M., Tutumluer, E., Lange, D., and Angulo, S. (2021). Roughness of natural aggregates by interferometry and its microstructure. *Construction and Building Materials*, 297:123646. 4.5
- Martin, P. (2021). Spectrograms. In *Speech Acoustic Analysis* (pp. 85-116). Hoboken, NJ: John Wiley & Sons, Inc.
- Martin, P. (2021). Spectrograms. In *Speech Acoustic Analysis* (pp. 85-116). Hoboken, NJ: Wiley & Sons, Inc.
- M., C. L. (1961). Slip-form paving, as developed and pioneered in iowa. *Maine Section American Society of Civil Engineers*. 1
- Makoto, K., Hiroshi, T., and Makoto, K. (1984). Influence of aggregate characteristics on movement of the particle in concrete due to vibrating compaction. *Bulletin of Engineering Geology & the Environment*, 30(1). 6.6
- Mollon, G. and Zhao, J. (2012). Fourier–voronoi-based generation of realistic samples for discrete modelling of granular materials. *Granular matter*, 14:621–638. 4
- Mollon, G. and Zhao, J. (2014a). 3d generation of realistic granular samples based on random fields theory and fourier shape descriptors. *Computer Methods in Applied Mechanics and Engineering*, 279:46–65. 4, 5
- Mollon, G. and Zhao, J. (2014b). 3d generation of realistic granular samples based on random fields theory and fourier shape descriptors. *Computer Methods in Applied Mechanics and Engineering*, 279:46–65. 4.3
- MnDOT. (2003). *Concrete Manual*. Minnesota Department of Transportation.
- Naderi, S. and Zhang, M. (2019). An integrated framework for modelling virtual 3d irregular particulate mesostructure. *Powder technology*, 355:808–819. 4.5
- National Concrete Pavement Technology Center. (2018, October 20). *Vibrating Kelly Ball (V-Kelly) Procedure*. Iowa State University Institute for Transportation.
- National Concrete Pavement Technology Laboratory. (n.d.). *PEM Test for Workability: The Box Test*. Iowa State University Institute for Transportation.
- Navarrete, I., & Lopez, M. (2017). Understanding the relationship between the segregation of concrete and coarse aggregate density and size. *Construction and Building Materials*, 149, 741-748.
- Olsson, E., Jelagin, D., and Partl, M. N. (2019). New discrete element framework for modelling asphalt compaction. *Road Materials and Pavement Design*, 20(sup2): S604–S616. 6.6

- Pennsylvania Department of Transportation, P. D. (2019). Field and laboratory testing manual. Standard, Pennsylvania Department of Transportation, Harrisburg, PA.
- Pennsylvania Department of Transportation, P. D. (2020). Construction specifications. Standard, Pennsylvania Department of Transportation, Harrisburg, PA.
- PCA. (2011). Design and Control of Concrete Mixtures 15th Edition. Washington D.C.: Portland Cement Association.
- Pekmezci, B., Voigt, T., Wang, K., & Shah, S. (2007). Low Compaction Energy Concrete for Improved Slipform Casting of Concrete Pavements. *ACI Materials Journal*.
- PennDOT. (2020). Publican 408. Harrisburg, PA: Pennsylvania Department of Transportation.
- Qian, Z., Garboczi, E., Ye, G., and Schlangen, E. (2016). Anm: a geometrical model for the composite structure of mortar and concrete using real-shape particles. *Materials and Structures*, 49:149–158. 4, 5.
- Rubinstein, R. Y. and Kroese, D. P. (2016). Simulation and the Monte Carlo method. John Wiley & Sons. 4, 5.2
- Safawi, M., & Iwaki, I. (2005, September). A study on the applicability of vibration in fresh high fluidity concrete. *Cement and Concrete Research*.
- Sainz-Aja, J., Carrascal, I., Polanco, J., Sosa, I., Thomas, C., Casado, J., & Diego, S. (2020, October). Determination of the Optimum Amount of Superplasticizer Additive for Self-Compacting Concrete. *Applied Sciences*.
- SME. (n.d.). Ride Quality. Retrieved from sme-usa.com: <https://www.sme-usa.com/ride-quality>
- Steffes, R., & Tymkowicz, S. (1997, April 1). Vibrator Trails in Slipformed Pavements. *Concrete Construction*.
- Steffes, R., & Tymkowicz, S. (1999). Vibration Study for Consolidation of Portland Cement Concrete. *Transportation Research Record*.
- Sticht. (n.d.). Standco Vibrating Reed Tachometers. Sticht Information Manual.
- Taylor, P., & Wang, X. (2018). Development and Evaluation of Vibrating Kelly Ball Test (VKelly test) for the Workability of Concrete. Iowa State University. National Concrete Pavement Technology Center.
- Total Concrete. (n.d.). Concrete Slump Tests -- Measuring the Workability of Concrete. Retrieved from Total Concrete Limited: <https://www.totalconcrete.co.uk/news/concrete-slump-tests-measuring-the-workability-of-concrete/>.
- Thilakarathna, P. S. M., Kristombu Baduge, S., Mendis, P., Chandrathilaka, E. R. K., Vimonsatit, V., and Lee, H. (2021). Aggregate geometry generation method using a structured light 3d scanner, spherical harmonics-based geometry reconstruction, and placing algorithms for mesoscale modeling of concrete. *Journal of Materials in Civil Engineering*, 33(8):04021198. 4
- Tymkowicz, S. and Steffes, R. F. (1997). Vibration study for consolidation of portland cement concrete. *Transportation research record*, 1574(1):109–115. 1.
- Voigt, T., Mbele, J.-J., Wang, K., and Shah, S. P. (2010). Using fly ash, clay, and fibers

- for simultaneous improvement of concrete green strength and consolidate ability for slip-form pavement. *Journal of Materials in Civil Engineering*, 22(2):196–206. 1, 3.2.4.
- Wang, W., Su, C., and Zhang, H. (2022). Automatic segmentation of concrete aggregate using convolutional neural network. *Automation in Construction*, 134:104106. 3.1
- Wang, X., Taylor, P., and Wang, X. (2017). A novel test to determine the workability of slipform concrete mixtures. *Magazine of Concrete Research*, 69(6):292–305. 1, 2
- Wang, X., Wang, K., Han, J., & Taylor, P. (2015). Image analysis applications on assessing static stability and flowability of self-consolidating concrete. *Cement and Concrete Composites*, 62, 156-167.
- Wei, D., Wang, J., Nie, J., and Zhou, B. (2018). Generation of realistic sand particles with fractal nature using an improved spherical harmonic analysis. *Computers and Geotechnics*, 104:1–12. 4.1, 4.2, 5
- Workmaster. (2018). *Vibra-Tak Slide Rule Tachometer*. Workmaster Information Manual.
- Xu, Y. and Chen, S. (2016). A method for modeling the damage behavior of concrete with a three-phase mesostructure. *Construction and Building Materials*, 102:26–38. 4
- Yan, X., Darnell, M., Vandenbossche, J., and Fascetti, A. (2024a). Deep learning-based entrapped air segmentation and evaluation (ease) for plain concrete pavement applications. In 13th International Conference on Concrete Pavements, volume 235, page In press, Minneapolis, Minnesota. Elsevier. 1, 3.1, 7
- Yan, X., Fascetti, A., Vandenbossche, J., and Darnell, M. (2024b). Computer vision-based estimation of the effects of vibration in slipform paving. 103th Transportation Research Record (TRR), 235:In press. 1, 3.1, 3.2
- Yang, Z., Ren, W., Mostafavi, M., McDonald, S. A., and Marrow, T. J. (2013). Characterisation of 3d fracture evolution in concrete using in-situ x-ray computed tomography testing and digital volume correlation. In VIII international conference on fracture mechanics of concrete and concrete structures, pages 1–7. Toledo, Spain CIMNE. 4.1
- Yilmaz, O. and Molinari, J.-F. (2017). A mesoscale fracture model for concrete. *Cement and Concrete Research*, 97:84–94. 3.2
- Zha, D., Bhat, Z. P., Lai, K.-H., Yang, F., and Hu, X. (2023). Data-centric ai: Perspectives and challenges. In Proceedings of the 2023 SIAM International Conference on Data Mining (SDM), pages 945–948. SIAM. 3.1
- Zhao, L., Zhang, S., Huang, D., Wang, X., and Zhang, Y. (2020). 3d shape quantification and random packing simulation of rock aggregates using photogrammetry-based reconstruction and discrete element method. *Construction and Building Materials*, 262:119986. 4.5
- Zhou, B. and Wang, J. (2017). Generation of a realistic 3d sand assembly using x-ray micro-computed tomography and spherical harmonic-based principal component analysis. *International Journal for Numerical and Analytical Methods in Geomechanics*, 41(1):93–109. 4.2

Zhou, H., Yu, X., and Jacobs, D. W. (2019a). Glosh: Global-local spherical harmonics for intrinsic image decomposition. In Proceedings of the IEEE/CVF International Conference on Computer Vision, pages 7820–7829. 4

Zhou, S., Sheng, W., Wang, Z., Yao, W., Huang, H., Wei, Y., and Li, R. (2019b). Quick image analysis of concrete pore structure based on deep learning. Construction and Building Materials, 208:144–157. 3.1



University of
Pittsburgh

Swanson School of Engineering

Department of Civil and Environmental Engineering

IRISE Consortium

742 Benedum Hall

3700 O'Hara Street

Pittsburgh, PA 15261

The information printed in this document was accurate to the best of our knowledge at the time of printing and is subject to change at any time at the University's sole discretion.

The University of Pittsburgh is an affirmative action, equal opportunity institution.